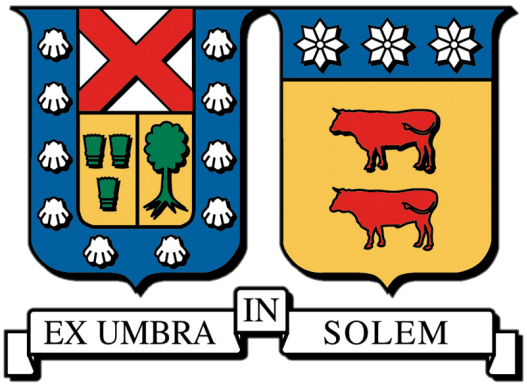
UNIVERSIDAD TÉCNICA FEDERICO SANTA MARÍA

PHYSICS DEPARTMENT



Cold Molecular Gas in Local X-ray selected AGN with Ionized Outflows

Enathian Andrés Ferrada Ruiz

THESIS SUBMITTED IN PARTIAL FULFILLMENT OF THE REQUIREMENTS FOR THE DEGREE OF BACHELOR OF SCIENCE IN ASTROPHYSICS

Supervisor: DR. ALEJANDRA ROJAS LILAYU

Ago-2026

CONSTANCIA DE VALIDACIÓN Y CONFIDENCIALIDAD DE MONOGRAFÍA A REPOSITORIO ACADÉMICO

1.- IDENTIFICACIÓN DEL TRABAJO ACADÉMICO

Tipo de monografía (marcar una opción): ☑ Memoria o trabajo de título ☐ Tesis de Postgrado

Título del trabajo: Cold molecular gas in local X-ray selected AGN with ionized outflows

Nombre del candidato(a): Enathian Ferrada

Carrera / Grado: Licenciatura en Astrofísica

Campus: San Joaquín **Departamento:** Física

2.- VALIDACIÓN DEL PROFESOR GUÍA/DIRECTOR DE TESIS

Yo, Alejandra Rojas Lilayú, en mi calidad de profesor(a) guía/director(a) del trabajo académico mencionado anteriormente **DEJO CONSTANCIA** que:

- He revisado esta versión del documento y corresponde a la versión final aprobada del trabajo.
- El trabajo cumple con los requisitos académicos y de formato establecidos por la institución.

3.- EVALUACIÓN DE CONFIDENCIALIDAD POR PROPIEDAD INDUSTRIAL (marcar una opción)

☑ El trabajo **NO contiene** información que amerite confidencialidad y puede ser publicado de inmediato en repositorio con acceso abierto.

☐ El trabajo **CONTIENE** información con potenciales implicancias de propiedad industrial o intelectual y requiere un periodo de confidencialidad (**embargo**) por **(marcar una opción)**:

☐ 6 meses ☐ 12 meses ☐ 2 años ☐ 3 años ☐ 5 años ☐ 10 años

Fundamentación de la necesidad de confidencialidad (obligatorio si se solicita embargo):

4.- FIRMAS

Profesor(a) guía o director(a) de memoria o tesis:

Fecha: 02 de Octubre 2026 **Firma:** 

Estudiante o Candidato(a):

Fecha: 29 de Septiembre de 2026 **Firma:** 

Este formulario debe ser insertado como página 2 de la memoria o tesis, completado y firmado por estudiante y profesor(a) antes de la entrega en portal PRISMA de Biblioteca USM.

Abstract

AGN play an active role in the formation and evolution of galaxies through a process known as feedback. Understanding this phenomenon is crucial for the study of star formation activity in the host galaxy, and therefore in galaxy evolution. Cold molecular gas observations offer a promising approach to assess the impact of AGN on the fuel available for star formation. The main goal of this work is to analyze sub-arcsec spatial resolution ($\lesssim$ 300 pc) ALMA Band 6 CO$(2-1)$ observations to investigate the influence of AGN on the cold molecular gas content, distribution and kinematics in a sample of local ($z < 0.1$) hard X-ray selected AGN displaying ionized outflow signatures. This sample covers a wide range in physical properties, allowing us to perform an unbiased statistical study of AGN activity and its effects on host galaxies. We find substantial amounts of cold molecular gas in the central regions of 16 out of 18 galaxies in our sample, with molecular gas masses ranging from $(M_{H_2}/M_\odot) = 1.2 \times 10^7$ to 8.2×10^9 and integrated spectral velocities in the range of $FWHM_{CO}$ = 90-480 km s^{-1}. Using kinematic models derived with ^{3D}BBarolo, we study the occurrence of cold molecular gas non-circular motions and if the presence of AGN results in negative or positive feedback.

Acknowledgements

I would like to express my deepest appreciation to Dr. Alejandra Rojas for her invaluable support and feedback throughout this entire project, as well as Dr. Darshan Kakkad, who generously shared his knowledge and expertise. I also extend my sincere gratitude to all the professors who guided me along the way, the university and physics department staff. I would be remiss in not mentioning my high school teacher Erwin Díaz, whose motivation and inspiration made me pursue this career in the first place.

On a personal note, special thanks to my mom and dad, and all my family who supported me from the very start. I am profoundly grateful to my partner Sayén, who was there to help me, encourage me and stay by my side through long hours. I could not have undertaken this journey without my best friends Isidora, Ignacio, Fernanda, Emilio, Juan José, Francisco, Kristina, Anastasia and everyone who stood by me through thick and thin.

I owe a special sense of debt and gratitude to Kyle Busch. Having rooted for him since I was a kid, his career had been a comforting constant throughout my life, and watching his domination and rowdy drives every weekend served as a source of motivation through every step of my academic journey. Life will never be the same since his passing, his influence is woven into every page of this text and therefore I would like to dedicate this work to him. Rowdy forever.

Contents

1 Introduction **1**

1.1 Active Galactic Nuclei . . . 1

1.1.1 Physical Components . . . 1

1.1.2 The AGN unified model . . . 4

1.1.3 AGNs across the electromagnetic spectrum . . . 6

1.1.4 AGN feedback . . . 11

1.1.5 Cold Molecular Gas . . . 13

1.2 Observation with ALMA . . . 18

1.2.1 Multi-array and Multi-configuration Observations . . . 19

1.2.2 Band 6 and Angular Resolution . . . 22

1.3 Motivation of the Study . . . 24

2 Sample **25**

2.1 The BASS survey . . . 25

2.2 The Selection Criteria . . . 25

2.2.1 ALMA Sample . . . 27

3 Analysis **28**

3.1 Morphological Properties . . . 28

3.1.1 CO$(2-1)$ Emission: Gaussian fits and estimation of the Flux-Luminosity . . . 28

3.1.2 Moment Maps . . . 32

3.1.3 Radial Profiles . . . 32

3.1.4 Contour Maps with VLA radio emission . . . 33

3.2 Kinematics . . . 33

3.2.1 ^{3D}BBarolo . . . 33

4 Results **35**

4.1 Molecular Gas Content . . . 35

4.2 Spatial Distribution and Kinematics of CO$(2-1)$ . . . 40

4.3 Radial Distribution of CO(2 – 1) 41
4.4 Spatial correlations of molecular gas emission radio continuum contours. 42
4.5 3D Kinematics Modeling 44

5 Discussion **52**
5.1 Molecular Gas Rings in 3C 403 and HE 0224-2834 53
5.2 Notes on Individual Targets 54

6 Summary and Conclusions **62**

7 Appendix A: Gaussian fits **76**

8 Appendix B: Moment Maps **87**

9 Appendix C: Radial Profiles **94**

10 Appendix D: Radio continuum observations with VLA and correlation with CO(2 – 1) ALMA observations **102**

11 Appendix E: ^{3D}BBarolo Modeling Results **106**

Chapter 1

Introduction

1.1 Active Galactic Nuclei

Active galactic nuclei (AGN) are understood to be energetic astrophysical sources powered by accretion onto supermassive ($\gtrsim 10^6 M_\odot$) black holes (SMBHs) in galaxy cores (e.g. Woo & Urry, 2002; Bentz & Katz, 2015). This implies a number of properties such as very high luminosities, reaching up to $L_{\rm bol} \approx 10^{48}$ erg s^{-1} (e.g. Duras et al., 2020), compact emitting regions of the order of a milliparsec, deduced by their rapid variability (Ulrich et al., 1997), strong evolution of luminosity functions (e.g. Boyle et al., 1987; Ueda et al., 2003) and unique observational features, that cover the full electromagnetic spectrum over more than twenty orders of magnitude in frequency, from γ-rays and visible light to infrared light and radio waves (Padovani et al., 2017; Padovani, 2017).

The wide variety of observational features seen in AGNs has led to an often overwhelming and confusing collection of different labels in the literature, commonly referred to as the AGN zoo. These labels depend on various things, such as the identification or selection schemes and the presence or absence of certain emissions (e.g. radio loud/radio quiet, Quasars, Blazars, Seyferts). To explain this, the AGN unified model was proposed, stating that the zoo of labels depends on a few parameters such as the viewing angle, the accretion rate, the presence or lack of jets, and the properties of the host galaxy or surrounding environment (e.g. Antonucci, 1993; Urry & Padovani, 1995; Padovani et al., 2017).

1.1.1 Physical Components

Characterizing the foundational components of an AGN, extending from the inner accretion disk to the outer gas outflows, is essential for understanding how the central black hole converts matter into galactic-scale energy. Within the framework of the unified model, these structural components dictate the observational classifications of AGNs, as each region governs a distinct emission process that defines a given class.

1.1.1.1 Accretion disk

Accretion disks around SMBHs continue to be the generally accepted paradigm for the central engine of AGN. It is a rotating structure of gas that spirals inward toward a central SMBH. Accretion is the flux of mass towards the inner regions of the SMBH, which transforms the gravitational

potential energy into kinetic energy.

The initial formulation on accretion disks with gas masses at cosmic scales was performed by Weizsäcker (1948), but the most widely adopted model is the standard α-disk model introduced by Shakura & Sunyaev (1973). This classical structure describes a geometrically thin, optically thick accretion disk where the gas is dense and cools with high thermodynamic efficiency, meaning all the heat generated by friction is dissipated as radiation. The model postulates that the necessary internal friction to drive the angular momentum transport required for accretion is generated by turbulent shear and local magnetic fields. To bypass the highly complex physics of this turbulence, they introduce the α-parameter. In this way, the kinematic viscosity ν is modeled as

$$\nu = \alpha c_s H, \tag{1.1}$$

where c_s is the speed of sound in the medium and H is the scale height of the disk.

However, for certain types of AGN such as low luminosity AGNs (LLAGNs) this prescription cannot account for every phase of black hole feeding, necessitating more complex models such as the advection-dominated accretion flows (ADAFs; see Narayan & Yi, 1994 and Narayan & Yi, 1995). In this case, gas does not cool efficiently, where instead of radiating its energy away, the heat is trapped in the gas and carried into the SMBH.

An interesting feature found in the solutions of Narayan & Yi (1995) for the efficient cooling limit (therefore resembling a thin disk) is that they have a low-density hot gas on top of an equatorial thin disk, which is at nearly virial temperature[1]. The hot gas resembles the corona that is thought to sit above the accretion disk on AGNs. They speculate that coronae are a natural and inevitable feature of any thin disk, that such coronae are best described as advection-dominated flows rather than static atmospheres, and that these coronae themselves present outflows with smaller mass-loss rates than in fully advection-dominated flows.

1.1.1.2 Corona

The corona is a highly compact region of ultra-hot ($T \sim 10^9$ K or ~ 100 keV), optically thin, relativistic plasma hovering close to the central SMBH, within a few gravitational radii.

The corona is understood to be the generator of the X-ray continuum emission observed in AGNs through inverse Compton scattering (Haardt & Maraschi, 1991), a process in which low-energy UV and optical photons escape the accretion disk and propagate into the corona, slamming into relativistic high-energy electrons. The collisions transfer kinetic energy from the electrons to the photons, up-scattering the UV light into high-energy hard X-rays.

Although its emission mechanism is well established, the geometry of the corona remains an area of ongoing debate, as its physical dimensions are far too compact to be spatially resolved by conventional imaging. Observational constraints from X-ray reverberation mapping frequently point toward a hyper-compact, point-like source configuration (e.g. Fabian et al., 2015), whereas recent X-ray polarimetry data suggest horizontally extended slab-like structures parallel to the disk plane (e.g. Kim et al., 2024).

[1]The virial temperature is the characteristic temperature a system of particles (e.g. a gas cloud) would reach if its thermal kinetic energy were perfectly balanced against its gravitational potential energy.

1.1.1.3 Dusty Torus

The dusty torus is the key component of the unified model of AGN (Antonucci, 1993; Urry & Padovani, 1995). The classical torus was envisioned as a simple, homogeneous, doughnut-shaped ring of gas and dust surrounding the SMBH and its accretion disk. Its primary job is to act as a shield, defining Type I and II AGNs based on the orientation; if the torus is observed face-on, we are looking down the hole of the doughnut, allowing a direct view to the accretion disk and the Broad Line Region (Type-I), while if the torus is observed edge-on, we look directly into the torus, where the thick dust blocks the core, leaving only the extended Narrow Line Region visible.

Modern studies suggest a different structure, proposing a clumpy torus model (e.g. Nenkova et al., 2002; Nenkova et al., 2008; Elitzur et al., 2004), as they show that the torus is actually an environment of individual, dense dust clumps or clouds rather than a continuous distribution of dust. Therefore, the observer's view is blocked not only by a dust screen but also by the probability of a cloud crossing the line of sight.

Recent observations using mid-infrared (MIR) interferometry have revealed that a considerable fraction of the dust emission comes from the polar regions (along the ionization cones), pushed outward by radiation pressure (Hönig et al., 2013; Asmus, 2019; Haidar et al., 2024).

1.1.1.4 Narrow Line Region

The Narrow Line Region (NLR) is an extended, low-density ($n_e \sim 10^4$) gaseous zone situated out from the central engine, spanning from 10s of parsecs to several kiloparsecs into the interstellar medium (ISM) of the host galaxy (Osterbrock & Ferland, 2006). Located outside the dusty torus, the NLR consists of low-density gas photoionized by the central continuum source, allowing for the emergence of forbidden lines (e.g. [O II], [O III], [N II], [S II]). In addition to the forbidden lines, permitted lines of H I, He I and He II are moderately strong, implying these narrow lines are emitted by highly-ionized gas.

The kinematics of the NLR clouds are dictated by the host galaxy's gravitational potential, yielding narrow line widths ($v \sim 250 - 1200$ km s^{-1}), consistent with the overall stellar velocity dispersion (Terlevich et al., 1990; Nelson & Whittle, 1996). Morphologically, the obscuration of equatorial photons by the dusty torus forces ionizing radiation to escape along the poles, often creating a resolvable bi-conical structure known as ionization cones (Pogge, 1989; Schmitt et al., 2003) or a conically shaped ionizing source (Tadhunter & Tsvetanov, 1989; Storchi-Bergmann et al., 1992; Macchetto et al., 1994), depending on the observational perspective.

1.1.1.5 Broad Line Region

The Broad Line Region (BLR) is a compact, dense, ionized environment located deep into the gravitational well of the SMBH, situated further out than the accretion disk but well inside the dusty torus (Antonucci, 1993). The BLR is composed of a large collection of discrete, high-velocity ($\sim$ 1000 to 10000 km s^{-1}) gas clouds at deep gravitational potentials. This extreme Keplerian motion induces massive Doppler broadening, widening permitted optical and UV emission lines (e.g. Hβ, Mg II, and C IV) to full widths at half maximum (FWHM) of several thousands of km s^{-1}. The BLR is composed of discrete gas clouds with high electron densities ($n_e \gtrsim 10^9$ cm^{-3}), which causes forbidden lines to become greatly weakened by collisional deexcitation, and typical temperature values for the region are around $T \approx 15000$ K (Osterbrock & Ferland, 2006).

For the same reasons as with the corona, the geometry and kinematics of the BLR are mapped via reverberation mapping techniques, which track the operational time lag between variations on the continuum and the response afterwards of the emission lines (e.g. Blandford & McKee, 1982; Peterson, 1993; Grier et al., 2017).

1.1.1.6 Relativistic Jets

Relativistic jets are highly collimated streams of magnetized plasma ejected at near-light speeds (Lorentz factors γ range from 2 to 50) from the cores of certain active galaxies. They can extend from sub-parsec scales out to kiloparsec scales and into intergalactic space. An important discovery was the resolution of the bright radio source, Cygnus A, into two lobes (Jennison & Das Gupta, 1953), where synchrotron radiation was identified as the radio emitting mechanism.

The physical launch mechanism of relativistic jets is driven by magnetohydrodynamic (MHD) processes occurring in the immediate vicinity of the SMBH. The primary theoretical engine for the launch of relativistic jets is the Blandford-Znajek mechanism (Blandford & Znajek, 1977), stating that if a strong magnetic field is anchored to the event horizon of a rapidly spinning black hole, the rotation of space-time itself twists the field lines, extracting rotational energy directly out of the black hole and converting it into a powerful relativistic magnetic jet. Another possibility (or complimentary approach) for jet launching comes from the Blandford-Payne mechanism (Blandford & Payne, 1982), where the energy and angular momentum are removed magnetically from the surface of the accretion disk, and if the magnetic field lines tilt outwards at an angle of less than 60° relative to the disk surface, a centrifugally driven outflow of matter from the disk is possible.

Relativistic jets play a critical role in galaxy evolution through Radio mode (Croton et al., 2006) AGN feedback, where the directed flows of plasma continuously inject big amounts of mechanical energy into the interstellar and intracluster media (McNamara & Nulsen, 2007). Rather than escaping smoothly, these jets displace the surrounding ambient gas, carving out giant X-ray cavities (or bubbles), and driving powerful shocks through the hot halos of host galaxies and galaxy clusters (Churazov et al., 2001; Fabian, 2012). By keeping the surrounding gas hot and highly turbulent, jets prevent gas reservoirs from collapsing into cold, star-forming molecular clouds (e.g. Alatalo et al., 2015; Morganti, 2017; Leftley et al., 2024).

1.1.2 The AGN unified model

A major observational and theoretical challenge is to construct a general picture that connects the various subgroups of AGNs. This paradigm, known as the Unified Model of AGN (Fig. 1.1), suggests that the vast zoo of observed active galaxies does not represent fundamentally different objects, but rather the same physical engine viewed from different angles relative to our line of sight (Antonucci, 1993; Urry & Padovani, 1995).

This scheme starts from a central SMBH fed by an accretion disk (e.g. Shakura & Sunyaev, 1973; Narayan & Yi, 1994, 1995). To this core engine, the model adds other components related to the gas (BLR, NLR) and dust (Dusty Torus) in the system, as well as a highly collimated relativistic radio and γ-ray jets. The appearance and classification of an AGN are mainly dictated by two main parameters: the orientation of the central obscuring dusty torus relative to the observer and the presence or absence of jets in the system.

To understand how the diverse classes of AGN fit into this single geometric framework, it is possible to divide them based on whether the AGN possesses a jet or not.

1.1.2.1 Radio Quiet AGN

In these systems, the emission is dominated by the accretion disk, surrounding gas clouds, and the dusty torus (Antonucci, 1993).

Seyfert Galaxies Often hosted by spiral galaxies (Adams, 1977), Seyfert galaxies possess moderate nuclear bolometric luminosities ranging between $\sim 10^{43} - 10^{45}$ erg s^{-1} (Woo & Urry, 2002). Within the radio-quiet regime, Seyferts are divided into two primary categories based on the properties of their optical spectra (Khachikian & Weedman, 1971).
Seyfert 1 Galaxies: When viewed at a low inclination angle (face-on), the observer's line of sight looks directly down the central opening of the dusty torus, providing an unobstructed view of the BLR, resulting in broad permitted emission lines ($\gtrsim 10^3$ km s^{-1}) in their spectra alongside narrow lines from the NLR (Antonucci, 1993; Osterbrock & Ferland, 2006).
Seyfert 2 Galaxies: In contrast, when the dusty torus is tilted at a high inclination (edge-on) to our line of sight, it physically blocks the accretion disk and the BLR. In these systems only the NLR is observed as it extends above the dusty torus with a conical or bi-conical geometry (Tadhunter & Tsvetanov, 1989; Schmitt et al., 2003), resulting in a stellar-dominated continuum with narrow lines ($\sim 10^2$ km s^{-1}) exclusively (Antonucci, 1993; Osterbrock & Ferland, 2006).

Quasars/QSOs Quasars represent the hyper-luminous counterparts of the Seyfert subdivision, typically exhibiting bolometric luminosities exceeding 10^{47} erg s^{-1} (e.g. Duras et al., 2017). Under the classic framework, their optical/UV appearance remains strictly governed by torus shadowing: Type-I Quasars are viewed face-on, directly seeing the non-stellar continuum from the accretion disk and BLR, while Type-II Quasars are heavily obscured by the torus, which blocks the optical/UV core and leaves only narrow emission lines alongside strong infrared (IR) re-emission from the heated dust grains (Urry & Padovani, 1995).

1.1.2.2 Radio Loud AGN

In a subset of AGN ($\sim 10\%$), the core launches powerful, relativistic plasma jets perpendicular to the accretion disk (Blandford & Königl, 1979). The orientation of these jets relative to Earth creates a separate set of classifications (Urry & Padovani, 1995).

Radio Galaxies When these systems are viewed at a wide angle (side-on), they are classified as radio galaxies, characterized by relativistic jets and immense total radio luminosities up to 10^{46} erg s^{-1} (Kellermann & Verschuur, 1988). Radio galaxies can be classified depending on their kinetic jet power into edge-darkened Fanaroff-Riley Class I (FR-1) and edge-brightened Fanaroff-Riley Class II (FR-II) systems (Fanaroff & Riley, 1974). Following the Seyfert dichotomy, if the dusty torus blocks the direct view of the core (as a Seyfert Type-II would do), it is classified as a Narrow-Line Radio Galaxy (NLRG), whereas a face-on perspective that exposes the BLR is classified as a Broad-Line Radio Galaxy (BLRG) (Antonucci, 1993; Urry & Padovani, 1995).

Blazars When the relativistic jet is oriented nearly perfectly along our direct line of sight, the physical engine undergoes extreme relativistic beaming (Readhead et al., 1978; Blandford & Rees, 1978). This geometric alignment causes the jet emission to be amplified and highly variable from radio to γ-rays, with apparent bolometric luminosities up to $\sim 10^{48}$ erg s^{-1} during flaring states (Ghisellini et al., 2009, 2010). Blazars can be subdivided based on the intrinsic energy of their surroundings: Flat-Spectrum Radio Quasars (FSRQs) represent high power systems that still preserve strong, broad emission lines from the background AGN environment while BL Lacertae Objects (BL Lacs) represent extreme environments where the beamed jet continuum is so bright that it leaves a featureless optical spectrum with no prominent emission or absorption lines (Urry & Padovani, 1995).

Although the classic geometric model attributes AGN diversity entirely due to our viewing angle relative to the obscuring dusty torus, it fails to explain distinct AGN classes that are instead governed by intrinsic physical mechanisms. An example are Low-Luminosity AGNs (LLAGNs), where the engine's accretion rate drops below $\dot{M}_{\rm crit} \approx 0.01\ \dot{M}_{\rm edd}$ (Ho, 2008) (where $M_{\rm crit}$ is the critical accretion rate and $\dot{M}_{\rm edd}$ is the Eddington accretion rate[2]), the accretion disk transitions into a Radiatively Inefficient Accretion Flow (RIAF), for example, an ADAF (Narayan & Yi, 1994, 1995; Ho, 2008). Due to the lack of ionizing power, these objects cannot sustain a BLR or a dusty torus, breaking the core assumptions of geometric unification (Nicastro, 2000; Elitzur & Shlosman, 2006). One example of LLAGNs are Low-Ionization Nuclear Emission-Line Regions (LINERs), whose emission is dominated by forbidden optical lines from low-ionization species.

Another example that challenges the classical unified model is Ultra Luminous Infrared Galaxies (ULRIGs), as they show that AGN appearance changes over time rather than via static viewing angle. It is proposed that these sources represent the initial dust enshrouded stages of quasars, and only once these nuclei shed the obscuring dust is the AGN allowed to visually dominate the decaying starburst, becoming optically selected quasars (Sanders et al., 1988).

1.1.3 AGNs across the electromagnetic spectrum

This section is based mostly on Netzer (2013) and Padovani (2017), as they give a very comprehensive look at AGN observations at different wavelengths throughout the electromagnetic spectrum. AGNs have different spectral signatures that are easily distinguished in several wavelength bands. The overall continuum emission across these bands is captured by the Spectral Energy Distribution (SED), which illustrates how an AGN distributes its bolometric luminosity across the electromagnetic spectrum (Fig. 1.2).

1.1.3.1 Optical/UV

Optical/UV emission in AGN comes from the accretion disk and the BLR (Shields, 1978; Davidson & Netzer, 1979). Because of the presence of dust, one can detect this emission only if our line of sight is unobscured, and therefore only in unobscured sources. The optical/UV band provides a biased view of the AGN phenomenon (Lawrence, 1991), although it was also due to their strong optical/UV emission that AGN were mostly discovered in the past (e.g. Green et al., 1986; York et al., 2000).

[2]The Eddington accretion rate is the mass falling onto a compact object (e.g. a SMBH) at which its emitted radiation theoretically balances the inward pull of gravity, known as the Eddington limit.

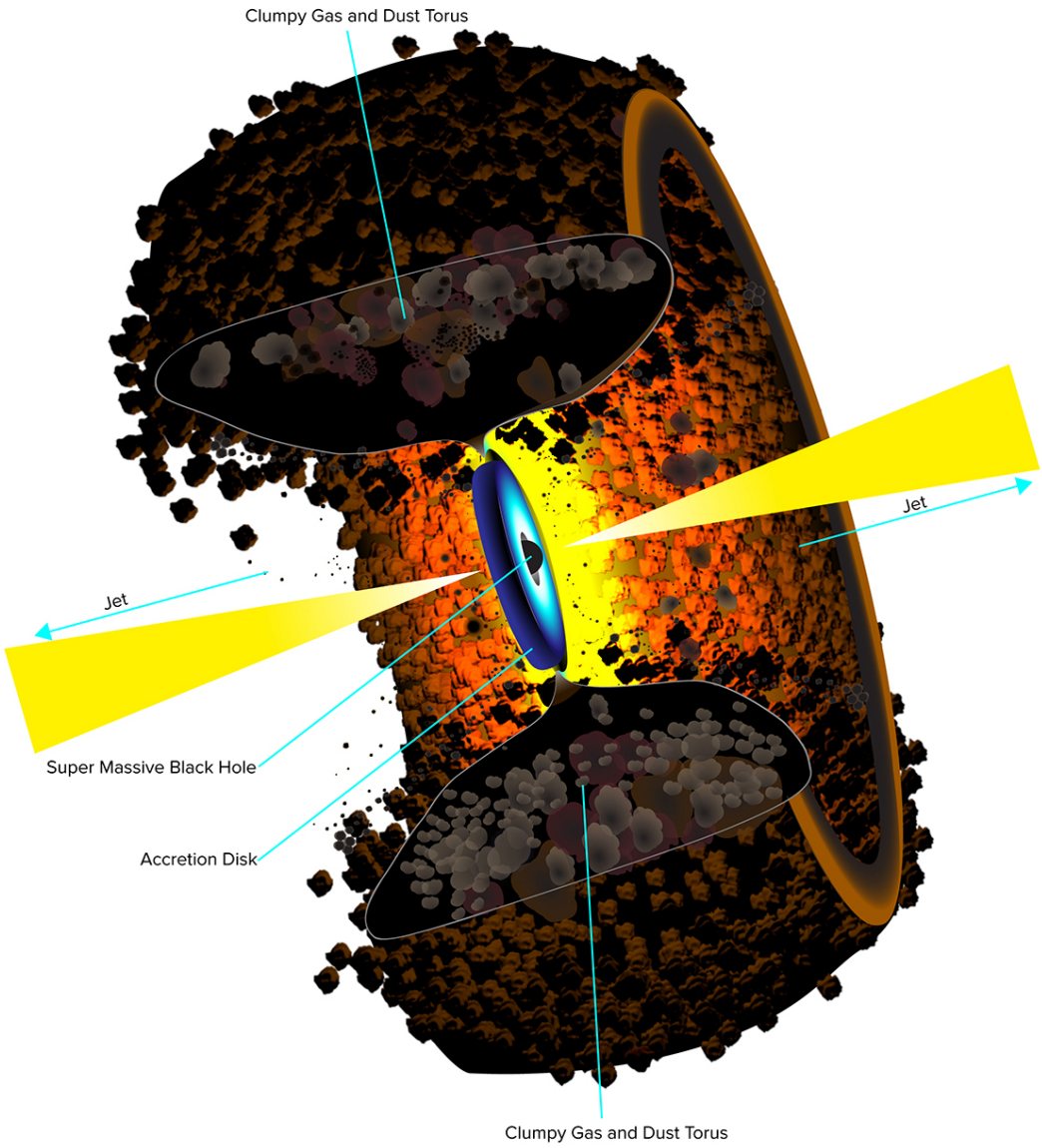


Figure 1.1: Artistic illustration of the AGN unified model. It includes the central black hole, a rotating disk of infalling material surrounding the black hole, and the jets speeding outward from the poles of the disk. In addition, to explain why the same type of object looks different when viewed from different angles, a thick, dusty, doughnut-shaped "torus" is included, surrounding the inner parts. The torus obscures some features when viewed from the side, leading to apparent differences to the observer, even for intrinsically similar objects. Credit: B. Saxton NRAO/AUI/NSF.

Optical/UV selected AGN include unobscured, non-jetted (radio quiet) sources (Type-I), whereas obscured AGN (Type-II) are expected to be missed in this band, although many of them are still selected through their narrow line emission (Baldwin et al., 1981; Kauffmann et al., 2003). Other biases are against LLAGNs where the host galaxy light outshines the light from the AGN (Ho et al., 1997). However, the optical/UV band is essential for the study of AGN because of the huge optical catalogs supplied (e.g. York et al., 2000), and the spectra provided, allowing us to estimate

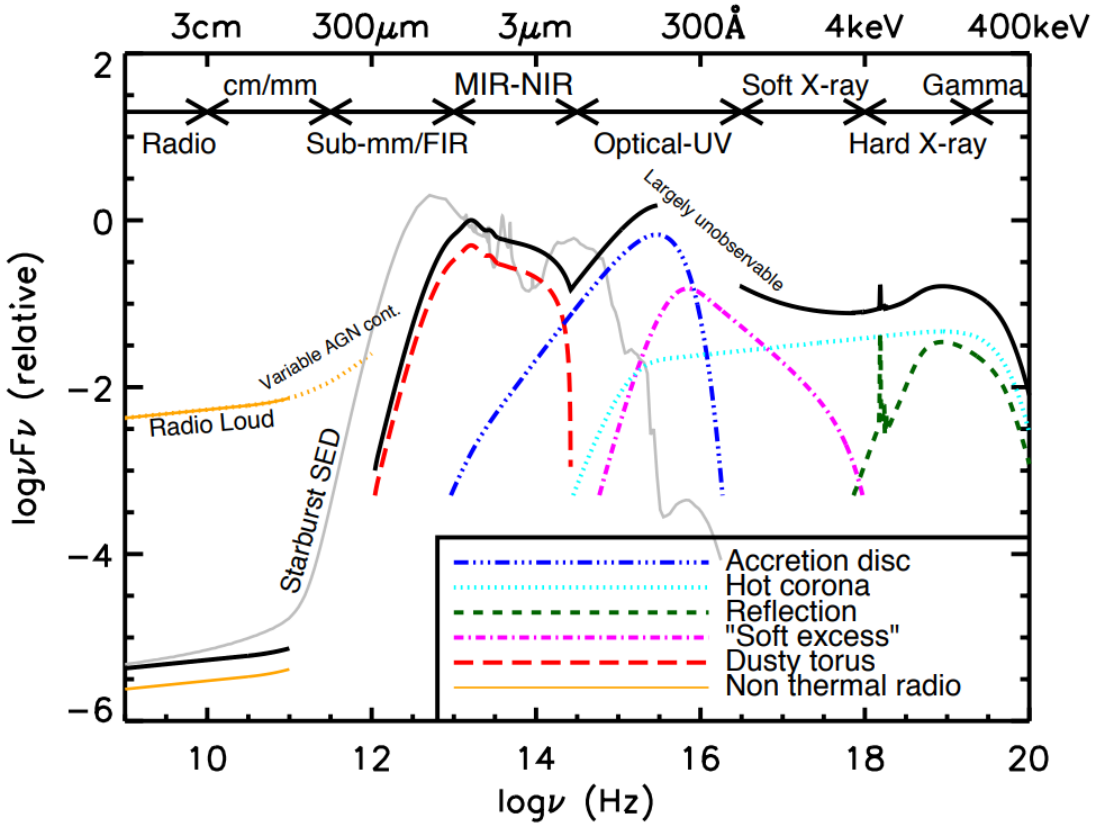


Figure 1.2: Schematic representation of the SED of an unobscured AGN (black curve), separated into the main physical components as indicated by the colored curves. The light gray curve is the SED of a star-forming galaxy for comparison. Credit to Harrison (2014).

the mass of the SMBH through reverberation mapping (e.g. Blandford & McKee, 1982; Peterson, 1993; Grier et al., 2017) and study the AGN spectral diversity.

The SED of an AGN in the optical and UV bands is driven by a featureless (non-stellar) continuum source and atomic emission lines from gas surrounding the central engine (Vanden Berk et al., 2001). The most prominent feature of this continuum is the Big Blue Bump, a considerable rise in flux that starts in the optical spectrum and peaks in the far-UV (Sanders et al., 1989; Elvis et al., 1994). This peak is generally understood to be the thermal signature of a geometrically thin, radiatively efficient accretion disk, where the gravitational potential energy from infalling matter is converted into viscous heat (Shields, 1978; Malkan, 1983; Kolykhalov & Sunyaev, 1984).

1.1.3.2 Infrared

The dust distributed around most AGN is known to absorb optical/UV light from the accretion disk and re-emit in the infrared (IR) band where it dominates the AGN SED at $\lambda \gtrsim 1$ μm up to a few tens of microns (Elvis et al., 1994; Richards et al., 2006).

Most of the emission in the Near-IR (NIR, $\sim 1-5$ μm) and Mid-IR (MIR, $\sim 5-30$ μm) bands is due to secondary dust emission, that is, emission by cold, warm or hot dust grains (e.g. graphite) that are heated by the primary AGN source (Barvainis, 1987), with temperatures of this emitting

dust between 100 and peaks at ∼2000 K (Koshida et al., 2014), temperature at which graphite grains evaporate (Salpeter, 1977). Primary dust emission refers to radiation that is directly related to accretion processes. Most of the thermal Far-IR (FIR, $\sim 30 - 250$ μm) emission is thought to be due to colder dust that is heated by young stars in large star-forming regions in the host galaxy (Sanders & Mirabel, 1996; Elbaz et al., 2011).

The study and sky mapping in IR was pioneered by the *Infrared Astronomical Satellite* (IRAS; Neugebauer et al., 1984), which provided the first all-sky MIR and FIR catalogs. An important milestone in terms of sensitivity and spectral capability was achieved with NASA's *Spitzer Space Telescope* (Werner et al., 2004), whose Infrared Spectrograph (IRS; Houck et al., 2004) mapped fine-structure line and Polycyclic Aromatic Hydrocarbon (PAH) features in AGNs . Most recently, the *James Webb Space Telescope* (JWST; Gardner et al., 2006) has provided unprecedented milliarcsecond spatial resolution and sub-milliJansky sensitivity across the MIR spectrum with its Mid-Infrared Instrument (MIRI; Rieke et al., 2015).

1.1.3.3 X-ray

X-ray images of AGNs typically reveal hot gas, visible across the soft ($\sim 2 - 10$ keV) and hard X-rays ($\gtrsim 10$ keV) in Type-I sources, but restricted to hard X-rays in obscured Type-II AGNs due to dust in the line of sight (Matt et al., 2000; Turner & Miller, 2009). Observations with X-ray telescopes such as the *Chandra X-Ray Observatory* relied on low-resolution data, but the spatial resolution was top notch (Weisskopf et al., 2000). Missions like the *XMM-Newton Observatory* improved the spectral resolution but lacked spatial resolution (Jansen et al., 2001), while the *X-Ray Imaging and Spectroscopy Mission* (XRISM, Kelley & Tashiro, 2024) revealed hundreds of narrow emission and absorption lines. Furthermore, high-energy instruments such as the *Suzaku X-Ray Observatory* (Mitsuda et al., 2007) and *Swift*/BAT (Gehrels et al., 2004; Baumgartner et al., 2013) have extended these low-resolution studies well beyond 100 keV, mapping the full energetic output of the central engine.

The X-ray spectra of unabsorbed Type-I AGN is characterized by an intrinsic power law ($\Gamma \sim 1.8 - 2.0$) originating from the corona, often coupled by a soft X-ray excess below ~ 2 keV (Nandra & Pounds, 1994; Crummy et al., 2006). In contrast, in Type-II sources the severe attenuation of the primary continuum allows reprocessed features to become prominent, such as the iron kα emission line at 6.4 keV (Matt et al., 2000). In Type-I AGN, this feature presents a complex profile, while in Type-II AGN, the line-of-sight column densities reach $N_H \gtrsim 10^{24}$ cm^{-2}, and the primary continuum is completely suppressed below ~ 10 keV (Comastri, 2004). This causes the spectrum to become reflection-dominated, causing the iron Kα line to stand out with equivalent widths of $\sim 1 - 2$ keV (Matt et al., 1996).

1.1.3.4 γ-ray

When we enter the γ-ray regime ($\gtrsim 100$ MeV to $\sim$ 10TeV range), the physical picture of the observed AGN component changes dramatically. It is convenient to divide the γ-ray band into two energy regimes; the high energy (HE) regime goes from 100 MeV to ~ 100 GeV, while the very high energy (VHE) regime covers the ~ 50 GeV to ~ 10 TeV range.

Observations at the HE regime are performed by electron pair-conversion telescopes in space, such as the AGILE (Tavani et al., 2009) and *Fermi* (Atwood et al., 2009). VHE γ-rays on the

other hand, are detected by Imaging Atmospheric Cherenkov Telescopes and Extensive Air Shower observatories on the ground (particle showers are observed at ground level, which are produced by the interaction of VHE γ-ray photons with the top layers of the atmosphere), such as Cangaroo, Hess, Magic, Veritas and HAWC (de Naurois & Mazin, 2015; Abeysekara et al., 2017).

While X-rays probe the emission of components such as the corona, γ-ray emission is dominated by relativistic, highly collimated jets in radio-loud AGN, where around $\sim 92\%$ of them are blazars (Padovani, 2017). It is clear that γ-rays are produced by relativistic jets in their more compact regions (Madejski & Sikora, 2016), but the process through which this occurs is not yet fully understood.

In blazars, the emission is strictly non-thermal and is usually represented by a double-humped SED (Fossati et al., 1998; Ghisellini et al., 1998; Baloković et al., 2016). It is well established that the lower-frequency hump is produced by synchrotron emission, ranging from radio to UV/X-ray bands, while the higher-frequency hump is believed to be due to leptonic processes, resulting in inverse Compton scattering (Blandford et al., 2019). This can happen in two ways; the electrons in the jet scatter their own synchrotron photons (synchrotron self-Compton), or the electrons scatter an external photon field (external inverse Compton) (Padovani, 2017).

1.1.3.5 Radio

AGNs have historically been cataloged as radio-loud/jetted and radio-quiet/non-jetted sources (Kellermann et al., 1989). In radio-loud AGNs, the radio band directly maps the extended structures of the jet, and the emission is entirely non-thermal, produced by synchrotron radiation (Jones et al., 1974). As discussed in the previous section, this is the exact population responsible for generating the lower-frequency bump in broadband SED of blazars (Fossati et al., 1998; Ghisellini et al., 1998). However, while blazars represent an aligned view where the jet points directly on our line of sight (Urry & Padovani, 1995), the macroscopic impact of jets is best mapped in radio galaxies.

The discovery of radio galaxies preceded the optical discovery of AGNs (e.g. Reber, 1944; Jennison & Das Gupta, 1953), except for the paper by Carl Seyfert in 1943. The main features of these sources are single or double-lobe structures with dimensions that can exceed those of the parent galaxy (Jennison & Das Gupta, 1953) and strong radio cores and/or radio jets in some sources that coincide in position with the nucleus of the optical galaxy (Baade & Minkowski, 1954; Wade, 1968). While most AGNs show some radio emission, there seems to be a clear dichotomy in this property. Statistics of a large number of AGNs show that about 10% of the sources are radio loud (Begelman et al., 1984), with some indication that the ratio decreases with redshift.

Much of the radio emission in radio-loud AGNs originates in a pointlike radio core (Blandford & Königl, 1979). The spectrum of such core-dominated radio sources suggests emission by a self-absorbed synchrotron source (Netzer, 2013; Blandford et al., 2019). Except for the self-absorption low-frequency part, most radio galaxies show a synchrotron power-law continuum ($L_\nu \propto \nu^{-\alpha_R}$). Sources with $\alpha_R < 0.5$ are usually referred to as flat-spectrum radio sources, and those with $\alpha_R > 0.5$ are steep-spectrum radio sources (Kellermann & Pauliny-Toth, 1969; Peacock & Wall, 1981). There is a clear connection between the radio structure and the radio spectrum of such sources (Urry & Padovani, 1995). Steep-spectrum radio sources show lobe-dominated radio morphology and are also less variable (Fanaroff & Riley, 1974). Flat-spectrum sources generally have higher luminosity cores, larger amplitude variations, and weak or undetected lobes (Fossati et al., 1998;

Blandford et al., 2019). This dichotomy is interpreted as a dependence on the viewing angle to the core (Antonucci, 1993). In steep-spectrum sources, one is looking away from the direction of the nuclear radio jet, and the radio emission is more or less isotropic. In flat-spectrum sources, we are looking at a small angle into the core. The intensity is boosted due to the relativistic motion of the radio-emitting particles, and the variations are amplified (Blandford & Königl, 1979; Blandford et al., 2019). In many cases, there is evidence for superluminal motion in such sources (Cohen et al., 1977; Blandford et al., 2019).

Understanding radio and γ-ray emission in AGN is essential to the study of jets. These structures play an important role in AGN feedback, as it is understood that these sources can displace material and therefore dictate the evolution of the galaxy via activation or quenching of star formation (Fabian, 2012).

1.1.3.6 Sub-millimeter

Sub-millimeter observations of a number of AGNs are also available, covering the range from 0.4 to about 1.2 mm, connecting the FIR and radio observations. Early work in this area relied on single-dish observations from telescopes such as SCUBA on the James Clerk Maxwell Telescope (Holland et al., 1999) and the IRAM 30-meter telescope (see Baars et al., 1987), which excelled at mapping larger portions of the sky and recovering larger spatial scales compared to interferometers (van Marrewijk et al., 2024). The Atacama Large Millimeter/sub-millimeter Array (ALMA) has revolutionized this area of astronomy with profound implications for both local and very high-redshift AGNs by providing sub-arcsecond spatial resolution observations, allowing the mapping of compact emission (Wootten & Thompson, 2009; Carilli & Walter, 2013).

As we have discussed, obscuration is a major problem when studying AGNs in the optical, UV and X-ray bands (Hickox & Alexander, 2018). Sub-millimeter radiation has longer wavelengths, passing through the obscuration material to image the immediate surroundings of the SMBH. With this, we are able to study the cold molecular gas content of AGNs (Solomon & Vanden Bout, 2005). SMBHs can only efficiently accrete material that is dense and cold enough ($10 - 100$ K) to collapse inward, making the study of cold molecular gas essential to understand black hole growth and galaxy evolution, as it is also the prime material for star formation (Kennicutt & Evans, 2012; Kormendy & Ho, 2013). If the gas is not cold, different accretion regimes take over, such as ADAFs (e.g. Narayan & Yi, 1994, 1995).

Its primary signatures are rotational molecular transitions such as CO, HCN and HCO^+ that emit in the millimeter and sub-millimeter regimes (Gao & Solomon, 2004; Carilli & Walter, 2013). By observing molecular outflows using the mentioned tracers, it is possible to see if the central engine is sweeping the cold molecular gas out of the galaxy, effectively quenching star formation and regulating host galaxy growth (e.g. Cicone et al., 2014; Fluetsch et al., 2021).

1.1.4 AGN feedback

The study of AGN feedback using cold molecular gas is important to understand the morphologies and reservoirs of the raw material that efficiently feeds the SMBH and allows for star formation. The general concept of feedback refers to physical processes, such as black hole activity, star formation, or supernova ionization, that can stop black hole growth and shut down star formation in the host galaxy (Netzer, 2013). AGN feedback is the liberation of energy from the AGN in

the form of outflows, which are high-velocity winds that carry energy, momentum, and radiation into the host galaxy's ISM (e.g. Fabian, 2012; King & Pounds, 2015). AGN feedback can also be related to relativistic jets that can displace the gas used in star-formation processes, directly affecting it and its host galaxy's evolution (Morganti et al., 2013). It is understood that there is a co-evolution between the AGN and its host galaxy (e.g. Kormendy & Ho, 2013), where the activation of the central engine is a phase in the evolution of the galaxy.

There are several ways to convert the emitted radiation to mass outflows and winds that interact more efficiently with the surrounding gas. To estimate the feedback efficiency in such cases, we must consider the wind kinetic energy and its momentum. Whether it is an energy or momentum-conserving outflow depends on if the outflow cools down radiatively or not (Faucher-Giguère & Quataert, 2012; King & Pounds, 2015). For energy-conserved outflows, the wind bubble is too hot and diffuse to cool down radiatively, keeping the thermal energy trapped, causing the gas to expand adiabatically, generating thermal pressure that pushes deep into the host galaxy, driving massive, galactic-scale outflows (Faucher-Giguère & Quataert, 2012). In contrast, momentum-conserving outflows the gas cools down through radiative processes, losing thermal pressure quickly and leaving the wind with only its mechanical impact to push the surrounding gas, driving a far less energetic outflow that typically fails to escape the galaxy's gravitational potential (King, 2010).

A likely mechanism to drive such outflows is radiation pressure force, and the likely launch location of the wind is in the accretion disk, as in the case of Broad Absorption Line (BAL) quasars (Elvis, 2000; Proga et al., 2000). The velocity of such outflows must be close to the escape velocity at the point where the flow is launched. If this is the innermost part of the disk, the velocity is of order $0.1 - 0.2c$ (King, 2010; Faucher-Giguère & Quataert, 2012; King & Pounds, 2015).

Massive outflows of gas, driven either by AGNs or star formation, can affect the evolution of galaxies. Over the past decades, studies of the formation and evolution of galaxies and the role that AGNs play in this process have been at the forefront of extragalactic astronomy. Studies that have explored the role of AGN in star formation have led to ambiguous results, with outflows capable of removing or heating of significant amounts of cold gas from the host galaxy (e.g. Cano-Díaz et al., 2012; Cicone et al., 2014; Shangguan et al., 2018), eventually regulating star formation by quenching it (known as negative feedback), or triggering local star formation (positive feedback) through high-velocity outflows (e.g. Ishibashi & Fabian, 2012; Cresci et al., 2015; Pillepich et al., 2018; Dubois et al., 2021). AGN feedback can also explain the tight correlation between the mass of the central SMBH and the velocity dispersion σ, the mass or luminosity of the host galaxy (e.g. Gültekin et al., 2009; Kormendy & Ho, 2013; McConnell & Ma, 2013; Fiore et al., 2017; Fluetsch et al., 2019).

Studies on galactic winds and outflows have aimed to understand the physical mechanism driving these processes and to verify if some of them can quench star formation. Observations have been made in different gas phases such as the warm ionized (e.g. Bellocchi, Enrica et al., 2013; Cazzoli et al., 2018), the hot, highly ionized (e.g. Tombesi et al., 2013; Nardini et al., 2015), the neutral atomic (e.g. Roberts-Borsani & Saintonge, 2019; Bischetti, M. et al., 2019; Morganti et al., 2016) and molecular gas (e.g. Cicone et al., 2014; Fluetsch et al., 2019; Fluetsch et al., 2021). Now, these studies focus on one outflow phase at a time, resulting in incomplete results, as it has been proven that galactic outflows can be multiphase in a number of studies (e.g. Morganti et al., 2015; Husemann et al., 2019; Herrera-Camus et al., 2020), so working with different wavelength observations allows us to unveil the nature and total energetics of the outflow.

Estimating outflow parameters such as mass outflow rate is extremely difficult and depends, in many cases, on complex filling factors due to an unresolved geometry (Harrison et al., 2018). These unknowns can lead to very high uncertainties in estimating the mass outflow rate and the associated kinetic energy and/or momentum, up to an order of magnitude in some cases (Davies et al., 2020). This can be mitigated using detailed modeling of the geometry and kinematics of the outflow, estimating the mass outflow rate more efficiently (e.g. Marconcini, C. et al., 2025).

1.1.5 Cold Molecular Gas

The cold gas content is a critical parameter in galaxy evolution, serving as the immediate fuel for star formation in galaxies. Research in recent years has resulted in an explosion in the number and type of galaxies detected in molecular line emission, as well as in atomic fine structure line emission, in the distant Universe (e.g. Tacconi et al., 2010; Genzel et al., 2015; Hodge & da Cunha, 2020). Detailed multi–transition, multi–species follow–up has been performed to determine the physical conditions of the gas in some of the brightest high–redshift systems known (Carilli & Walter, 2013).

Typical ISM pressures lie in the range $p/k = nT \sim 10^3 - 10^4$ cm^{-3} K, and because radiative cooling by spectral-line emission depends strongly on temperature, most of the ISM exists in several distinct phases having comparable pressures but quite different temperatures; cold (~ 10 K) dense molecular clouds; cool ($\sim 10^2$ K) neutral Hi gas; warm ($\sim 5 \times 10^3$ K) neutral Hi gas; warm ($\sim 10^4$ K) ionized Hii gas; hot ($\sim 10^6$ K) low-density ionized gas (Condon & Ransom, 2016).

Solomon & Vanden Bout (2005) provided a comprehensive look into the molecular gas content in AGN. In particular, they point out that the observation of emission from CO rotational transitions is the dominant means of tracing interstellar molecular clouds, which consist almost entirely of molecular hydrogen, H_2. This is because cold H_2 is not directly observable in emission, as it is a diatomic molecule with identical nuclei and thus does not possess a permanent dipole moment and corresponding dipolar rotational transitions. The lowest energy transitions of H_2 are its pure rotational quadrupole transitions in the FIR at $\lambda = 28.22$ μm and shorter wavelengths, cataloged as weak due to their long spontaneous decay lifetimes of $\tau_{\rm decay} \sim 100$ years (see Bolatto et al., 2013). The two lowest para and ortho transitions have upper level energies $E/k \approx 510$ K and 1015 K above ground (Dabrowski, 1984), therefore they only get excited in gas with $T \gtrsim 100$ K (Bolatto et al., 2013). This means the cold molecular hydrogen that makes up most of the molecular ISM in galaxies is invisible in emission (e.g. Solomon & Vanden Bout, 2005; Carilli & Walter, 2013).

CO emission is the best tracer of molecular hydrogen for two reasons (see (Bolatto et al., 2013)). It is a very stable molecule and the most abundant after H_2. Second, a weak dipole moment ($\mu_e = 0.11$ Debye) means that CO rotational levels are excited and thermalized by collisions with H_2 at relatively low molecular hydrogen densities. Strong CO emission from interstellar gas dominated by H_2 is ubiquitous.

As discussed before, outflows can quench or trigger star formation in galaxies. In particular, the removal of cold molecular gas is a way to stop SF in a relatively short period of time. This can be considered as evidence for a negative AGN feedback (Netzer, 2013). Observational evidence from FIR spectroscopy by *Herschel* shows several detections of molecular outflows in ULIRGs (e.g. Sturm et al., 2011; Spoon et al., 2013; González-Alfonso et al., 2017). In some of these objects, the terminal outflow velocities exceed 1000 km s^{-1}, and their outflow rates reach ~ 1200 $M_\odot$ yr^{-1} (where $M_\odot$ are solar masses), which are several times larger than their star formation rates (SFRs) (Sturm et al., 2011). There is a clear connection between the outflow velocity and the presence of

AGNs (Sturm et al., 2011; Veilleux et al., 2013; Fiore et al., 2017). The outflows in the observed ULIRGs are able to expel the cold gas reservoirs from the centers of these objects within $10^6 - 10^8$ yr (Sturm et al., 2011). Because of this, it is in our interest to study the molecular gas content and kinematics to better understand the effect of AGN feedback on the suppression or trigger of star formation, SMBH feeding and host galaxy evolution.

1.1.5.1 The CO $J = 2 \rightarrow 1$ Rotational Transition

A molecule is called polar if its permanent electric dipole moment is not zero. Symmetric molecules (e.g., the diatomic hydrogen molecule H_2) do not have a permanent electric dipole moment, but most asymmetric molecules (e.g., the carbon monoxide molecule CO) do have asymmetric charge distributions and are polar. The electric dipole moments of polar molecules rotating with constant angular velocity appear to vary sinusoidally with angular frequency, so polar molecules radiate at their rotation frequencies (Condon & Ransom, 2016).

In order to understand why the CO(2−1) transition is important to the study of cold molecular gas, we must first understand the fundamentals of molecular line frequencies and excitation. The quantization of rotational energy implies that changes in rotational energy are quantized:

$$E_{\rm rot} = \frac{\hbar^2}{2I} J(J+1), \qquad J = 1, 2, ..., \tag{1.2}$$

where $\hbar$ is the reduced Planck constant, I is the moment of inertia of the rotating system and J is the rotational quantum number. The energy change of permitted transitions is further restricted by the quantum-mechanical selection rule

$$\Delta J = \pm 1 \tag{1.3}$$

Going from J to $J-1$ releases energy

$$\Delta E_{\rm rot} = [J(J+1) - (J-1)J]\frac{\hbar^2}{2I} = \frac{\hbar^2 J}{I} \tag{1.4}$$

The frequency of the photon emitted during this rotational transition is

$$\nu = \frac{\Delta E_{\rm rot}}{h} = \frac{\hbar J}{2\pi I}, \qquad J = 1, 2, ... \tag{1.5}$$

where J is the angular-momentum quantum number corresponding to the upper energy level. In terms of the molecular reduced mass m and equilibrium nuclear separation r_e,

$$\nu = \frac{hJ}{4\pi^2 m r_e^2}, \qquad J = 1, 2, ... \tag{1.6}$$

Thus a plot of the radio spectrum of a particular molecular species in an interstellar cloud will look like a ladder (Fig. 1.3):

For the CO molecule, $r_e \approx 1.13 \times 10^{-8}$ cm. Spectral lines emitted by more rapidly rotating $^{12}C^{16}O$ molecules will have frequencies slightly lower than the harmonics $2\nu_{1-0}$, $3\nu_{1-0}, ...$ of the $J = 1 \rightarrow 0$ line; $2\nu_{1-0} = 230.542416$ GHz and the actual $J = 2 \rightarrow 1$ frequency is $\nu_{2-1} = 230.538000$ GHz.

The minimum gas temperature $T_{\rm min}$ needed for significant collisional excitation is

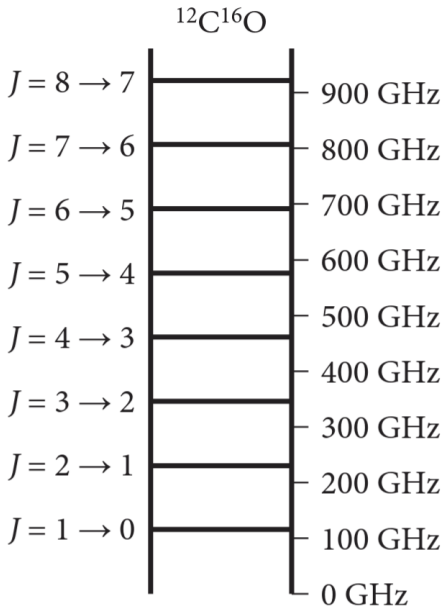


Figure 1.3: The rotational spectrum of $^{12}C^{16}O$ looks like a ladder whose rungs indicate the J levels and line frequencies. The $^{12}C^{16}O$ molecule has a relatively small moment of inertia, so the lowest rung of this ladder is at $\nu \approx 115$ GHz ($\lambda \approx 2.6$ cm); it has no cm-wavelength lines (Condon & Ransom, 2016).

$$T_{\rm min} \sim \frac{E_{\rm rot}}{k} \tag{1.7}$$

From equations 1.1 and 1.5,

$$E_{\rm rot} = \frac{J(J+1)\hbar^2}{2I} \qquad \text{and} \qquad \nu = \frac{hJ}{4\pi^2 I} \tag{1.8}$$

therefore

$$T_{\rm min} \sim \frac{J(J+1)h^2}{2 \cdot 4\pi^2 I k} = \frac{hJ}{4\pi^2 I}\frac{h(J+1)}{2k} = \nu E_{\rm U} \tag{1.9}$$

where $E_{\rm U}$ is the rotational energy of the upper energy level for the transition. Thus a minimum gas kinetic temperature

$$T_{\rm min} \approx \frac{\nu h(J+1)}{2k} \tag{1.10}$$

is required to excite the $J \rightarrow J-1$ transition at frequency ν. With this, it is possible to explain why CO$(2-1)$ is a good cold molecular gas tracer by comparing it to other CO transitions.

Let us compare $T_{\rm min}$ of the CO$(1-0)$, CO$(2-1)$ and CO$(7-6)$ transitions:

$$T_{\rm min,\ CO(1\text{-}0)} = 5.53 \text{ K}, \qquad T_{\rm min,\ CO(2\text{-}1)} = 16.6 \text{ K}, \qquad T_{\rm min,\ CO(7\text{-}6)} = 154.87 \text{ K} \tag{1.11}$$

Cold molecular gas tracers, such as CO$(1-0)$ and CO$(2-1)$ have very low minimum temper-

atures, therefore, it is possible to excite them and expel a photon at very low temperatures, unlike the case with the CO$(7-6)$ transition, which requires higher temperatures to excite them.

There are several CO transitions that can trace cold molecular gas, such as the already mentioned CO$(1-0)$ and CO$(2-1)$ rotational transitions, but according to the definition of cold dense molecular clouds (see Condon & Ransom, 2016), CO$(3-2)$ and CO$(4-3)$ transitions work as well. We will see in the next section that this is actually not sustainable, and at low temperatures, only CO$(1-0)$ and CO$(2-1)$ populations are true tracers of cold molecular gas, as CO$(3-2)$ and CO$(4-3)$ become statistically insufficient to effectively trace gas at these temperatures.

1.1.5.2 Statistical Mechanics

As seen, CO$(2-1)$ has a minimum temperature to excite the molecule and emit a photon. This temperature serves as a lower limit to the excitation of a CO$(2-1)$ molecule, and the issue we have to deal with now is that at higher temperatures this is also achieved. Therefore, in principle, CO$(2-1)$ can also trace the warmer gas as well. To solve this, we must dive into statistical mechanics.

In statistical mechanics, the Boltzmann distribution describes the probability that a system in thermal equilibrium is found in a state with a specific energy. We must assure that we are in thermal equilibrium, therefore we need to check that $n \gg n_{\rm crit}$,

$$n_{\rm crit} = \frac{A_{ul}}{\gamma_{ul}} \tag{1.12}$$

where A_{ul} is the Einstein coefficient for a given rotational transition and γ_{ul} is the collision rate. The data used for these values for the rotational transition $J = 2 \rightarrow 1$ ($u = 3, \quad l = 2$) is obtained from Schöier et al. (2005). The Einstein coefficient is $A_{32} = 6.910 \times 10^{-7}$ s^{-1}, while the collision coefficient is $\gamma_{32} = 6.440 \times 10^{-11}$ cm^3 s^{-1} at 20 K. We select this temperature to study the maximum density threshold to get over. With this,

$$n_{\rm crit} = \frac{6.910 \times 10^{-7}\ \text{s}^{-1}}{6.440 \times 10^{-11}\ \text{cm}^3\ \text{s}^{-1}} \approx 1.073 \times 10^4\ \text{cm}^3 \tag{1.13}$$

The definition of cold molecular gas seen before ($p/k = nT \sim 10^3 - 10^4$ cm^{-3}), sets its density at around $2 \times 10^4 - 2 \times 10^5$ cm^{-3}. The condition for a gas to be in local thermal equilibrium (LTE) is $n \gtrsim n_{\rm crit}$. In this case, n is about the same or 1 order of magnitude higher than the critical density $n_{\rm crit}$,

$$\frac{n}{n_{\rm crit}} \sim 1.86 - 18.6 \tag{1.14}$$

at the selected temperature. Therefore, it is correct to assume that we are in LTE at 20 K, higher than the minimum temperature required for significant collisional excitation. This is done to make sure that our calculations are conservative and serve as a reliable approximation. We have to be careful, because we are at the very limit of the LTE approximation.

We have the Boltzmann distribution

$$P_{J=2} = \frac{N_{J=2}}{N_{\rm total}} = \frac{g_2\ e^{-E_2/kT}}{Z(T)}, \tag{1.15}$$

where $N_{J=2}$ is the density of molecules in the $J = 2$ state, N_{total} is the total density of CO molecules (that is, the sum of all populations of CO molecules; $N_{\text{total}} = \sum_i N_i$), and g_2 is the weight or degeneration of the $J = 2$ level. We use this to analyze the population fraction of the $J = 1, 2, 3, 4, 5$ level of CO at a representative temperature of 20 K. This allows us to demonstrate that a statistically significant fraction of the molecule participates in the CO $(2 - 1)$ transition, confirming the robustness of this line as a tracer of the cold molecular gas. For rigid rotational systems, the degeneracy is given by the multiplicity $2J + 1$. E_2 is the energy of the $J = 2$ level, which can be obtained directly from the data from Schöier et al. (2005), T is the temperature of the system (which we fixed at 20 K), k is the Boltzmann constant and $Z(T)$ is the partition function. The theory of statistical mechanics defines the partition function Z to be

$$Z(T) \equiv \sum_{J=0}^{J_{\text{max}}} g_J \; e^{-E_J/kT} \tag{1.16}$$

We compute the degeneracy, energy, and partition function for all rotational levels in Table 1.1 below.

Table 1.1: Values for degeneracy, energy and partition function for different rotational levels of molecules of CO. The energies are obtained from Schöier et al. (2005).

J	g_J	E_J	$Z_J(T)$
0	1	0 K	1
1	3	5.53 K	2.275
2	5	16.60 K	2.180
3	7	33.19 K	1.332
4	9	55.32 K	0.566
5	11	82.97 K	0.174

Summing all contributions, the total partition function is

$$Z(T) = Z_0 + Z_1 + Z_2 + \cdots = 7.527 \tag{1.17}$$

Therefore, the population factor of CO at the $J = 2$ level is

$$P_{J=2} = \frac{5 \; e^{-16.6/20}}{7.527} = 0.2896 \tag{1.18}$$

This means that $\sim 29\%$ of the population of CO is in the $J = 2$ level. The values for all levels are tabulated in Table 1.2 below:

As we can see, the most populous levels are $J = 1$ and $J = 2$ at 20 K, exactly both rotational levels that are involved in the CO $(J = 2 \to 1)$ transition. Statistical mechanics demonstrates that at the low temperatures characteristic of cold molecular gas, this specific transition dominates over others because its energy levels host the highest fraction of the total molecular population.

Now, this is a really modest estimate, due to higher levels being outside the LTE regime. At these levels, T_{min} increases, which causes density to decrease, to the point where n is no longer much smaller than n_{crit}. For the CO $J = 3 \to 2$ and $J = 4 \to 3$ transitions, we have the following:

Table 1.2: Population values for CO rotational levels $J = 1, 2, 3, 4, 5$.

J	P_J	$P_J(\%)$
0	0.1329	13.29
1	0.3022	30.22
2	0.2896	28.96
3	0.1769	17.69
4	0.0752	7.52
5	0.0231	2.31

$$T_{\text{min, CO(3-2)}} = 33.19 \text{ K}, \qquad n_{\text{crit, CO(3-2)}} = 3.542 \times 10^4 \text{ cm}^{-3} \qquad \frac{n}{n_{\text{crit}}} \sim 0.93 - 9.3 \tag{1.19}$$

and

$$T_{\text{min, CO(4-3)}} = 55.32 \text{ K}, \qquad n_{\text{crit, CO(4-3)}} = 8.348 \times 10^4 \text{ cm}^{-3} \qquad \frac{n}{n_{\text{crit}}} \sim 0.66 - 6.6 \tag{1.20}$$

This means that for $J \gtrsim 3$, the Local Thermal Equilibrium (LTE) approximation is no longer acceptable (it only applies for the higher density limit), and population factors are greatly overestimated. These higher levels are under a double penalty. First, they are intrinsically less populated than $J = 1$ and $J = 2$ levels, and on top of that, because T_{min} is higher at these levels, cloud densities will decrease below the critical density, falling out of LTE. This makes the Boltzmann distribution equation inefficient, overestimating population factors. This means that $\text{CO}(1-0)$ and $\text{CO}(2-1)$ populations are the most efficient cold molecular gas tracers, as $\text{CO}(3-2)$ and $\text{CO}(4-3)$ may happen at these temperatures, but not in enough quantity to be a trustworthy tracer.

Hence, we have demonstrated that the $\text{CO}(1-0)$ and $\text{CO}(2-1)$ transitions are preferred to work with when tracing cold molecular gas. One main reason for why we use $\text{CO}(2-1)$ instead of $\text{CO}(1-0)$, is because it is the most populous transition seen in the ISM, thus, it is easily observable. Another argument comes from ALMA interferometry.

1.2 Observation with ALMA

This section is based on the ALMA Technical Handbook Cycle 13[3] (Cortes et al., 2026). The Atacama Large Millimeter/Submillimeter Array (ALMA) is an aperture synthesis telescope consisting of 66 antennas that can be positioned in a number of different configurations (Wootten & Thompson, 2009). It operates over a broad range of observing frequencies in the millimeter and submillimeter regime of the electromagnetic spectrum.

Of the 66 antennas available, fifty of those are 12-meter antennas in the 12-m Array, used for sensitive, high-resolution imaging. These are complemented by the Atacama Compact Array

[3]https://almascience.eso.org/proposing/technical-handbook

(ACA), composed of twelve closely spaced 7-m antennas (the 7-m Array), and four 12-m antennas for single-dish (or Total Power) observations (the TP array), to recover the emission at the most extended spatial scales.

The 12-m Array : The 12-m Array consists of fifty 12-meter diameter antennas, whose configurations have been designed so that at the highest frequencies in the most extended configurations, the angular resolution will be as small as 5 milliarcsecond at 950 GHz, though the smallest angular resolution that has been offered for Principal Investigator (PI) science is 9 milliarcseconds.

The Atacama Compact Array (ACA) : To achieve high-fidelity imaging of sources with emission on angular scales larger than those corresponding to the minimum spacing of the 12-m Array, ALMA has been designed to include the ACA. The ACA is composed of twelve 7-meter antennas for interferometry (the 7-m Array) and four 12-meter antennas for single-dish observations (TP Array).

i) The 7-m Array : The 7-m Array is composed of twelve 7-meter diameter antennas. Even in its most compact configuration the 12-m Array does have spacings smaller than 15 m. so the array is designed to fill in these shorter spacings from about 9 m to $\sim$ 30 m.

ii) The TP Array : It consists of four 12-m diameter antennas. The TP Array is designed to fill in baseline coverage from 0 m to about 12 m, complementing the 7-m and 12-m Array's baseline coverage.

The ALMA front-end can accommodate up to 10 receiver bands covering most of the wavelength range from 8.5 to 0.32 mm (35-950 GHz). Each band is designed to cover a tuning range which is approximately tailored to the atmospheric transmission windows. These windows and the tuning ranges are outlined in Figure 1.4. This illustrates the broad and deep absorption features, mostly due to H_2O in the lower few km of the atmosphere, as well as some O_2 transitions. The many features seen in this plot are mostly from stratospheric O_3, along with some transitions of CO and other trace species.

1.2.1 Multi-array and Multi-configuration Observations

Depending on the range of angular scales required, an ALMA Science Goal will obtain data from either: a single 12-m Array configuration; two 12-m Array configurations; one or two 12-m Array configurations plus the 7-m Array; or one or two 12-m Array configurations plus the 7-m and Total Power (TP) Arrays. Table 1.3 gives guideline properties of the 12-m and 7-m Array configurations. Each configuration is characterized by an angular resolution $\theta_{\rm res}$, related to the shortest and longest baselines in the configuration, respectively. Due to scheduling and availability of specific antenna pads, configurations are not directly selected, but rather the required angular resolution ($\theta_{\rm res}$) and largest angular scale ($\theta_{\rm LAS}$) is specified by the ALMA Observing Tool (ALMA OT), and projects are observed using array configurations that will achieve the specified science goals.

To achieve the requirements entered by the PI in the OT, ($\theta_{\rm res}$) and ($\theta_{\rm LAS}$), multiple configurations may be needed. Based on the user-entered values of ($\theta_{\rm res}$) and ($\theta_{\rm LAS}$) for a given Science

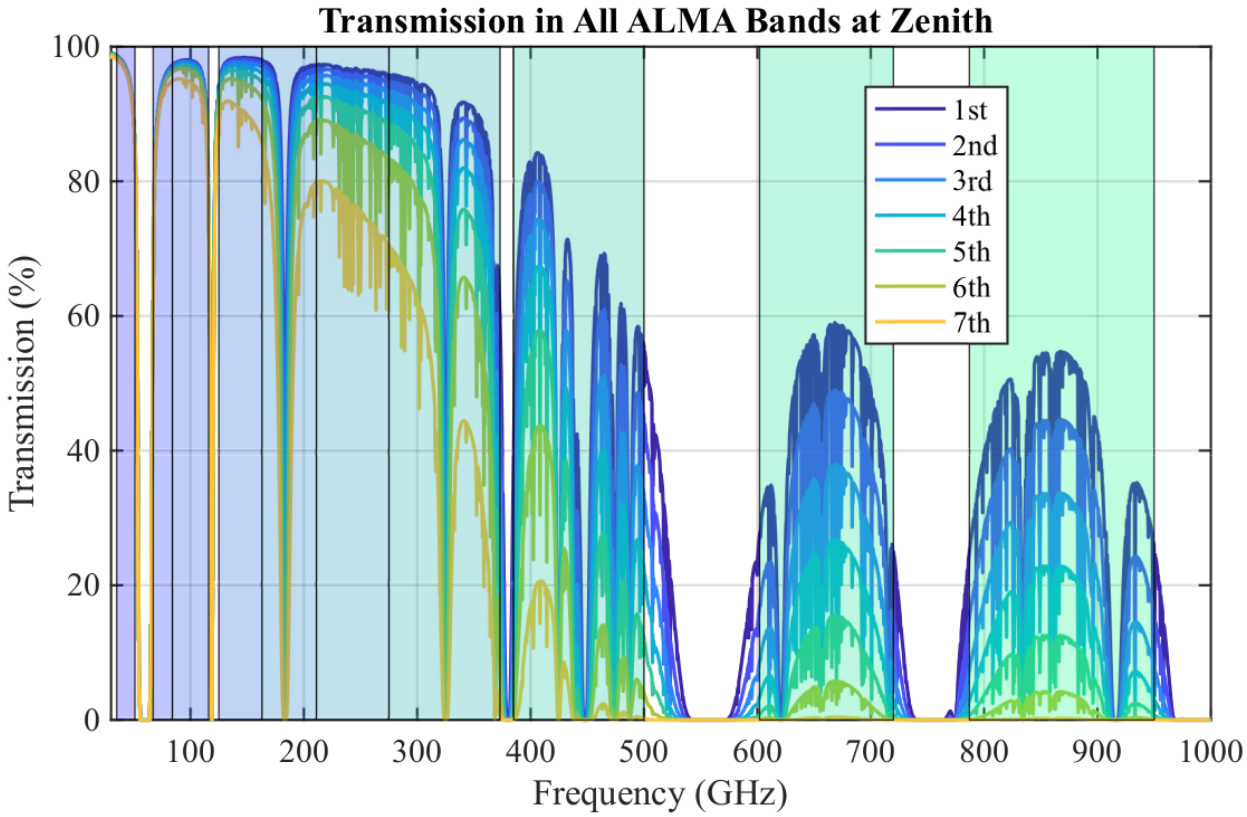


Figure 1.4: The ten ALMA receiver bands along with atmospheric transmission. The receiver coverage is shown shaded, superimposed on a zenith atmospheric transparency plot at the Array Operation Site (AOS) for the first seven octiles of observing conditions at ALMA (Cortes et al., 2026).

Goal, the OT will automatically attempt to choose configurations that will produce a final image with the requested scientific requirements. To provide good quality images, there are some restrictions on which arrays and configurations can be combined within a single Science Goal (e.g. at most, two 12-m Array configurations are allowed, and the most extended configurations (C-10) cannot be combined with any more compact configurations). The permitted multi-array and multi-configurations are shown in Table 1.4.

While the overall integration time is set by the specific requirements of the Science Goal a PI defines, the relative integration times between its component configurations/arrays are determined by general considerations as discussed in Mason & Brogan (2013). The relative integration times do not depend on the details of the Science Goal beyond the fact that the Science Goal definition determines which combination of configurations or arrays are needed. Broadly speaking, because of their smaller collecting areas, the TP and 7-m Arrays require more on-source integration time than the 12-m Array.

Table 1.3: Angular resolution ($\theta_{\rm res}$) values for different 7-m Array and 12-m Array configurations are shown for one representative frequency in each ALMA receiver band (Cortes et al., 2026).

	Band	1	2	3	4	5	6	7	8	9	10
	Freq (GHz)	40	75	100	150	185	230	345	460	650	870
Config											
7-m	$\theta('')$	31.8	16.9	12.7	8.47	6.87	5.52	3.68	2.76	1.95	1.46
C-1	$\theta_{max}('')$	8.28	4.42	3.31	2.21	1.79	1.44	0.96	0.72	0.51	0.38
	$\theta_{min}('')$	7.69	4.10	3.07	2.05	1.66	1.34	0.89	0.67	0.47	0.35
C-2	$\theta_{max}('')$	7.96	4.24	3.18	2.12	1.72	1.38	0.92	0.69	0.49	0.37
	$\theta_{min}('')$	7.31	3.89	2.92	1.95	1.58	1.27	0.85	0.64	0.45	0.34
C-3	$\theta_{max}('')$	5.97	3.19	2.39	1.59	1.29	1.04	0.69	0.52	0.37	0.27
	$\theta_{min}('')$	4.79	2.55	1.91	1.28	1.03	0.83	0.55	0.42	0.29	0.22
C-4	$\theta_{max}('')$	3.54	1.88	1.41	0.94	0.76	0.61	0.41	0.31	0.22	0.16
	$\theta_{min}('')$	2.99	1.60	1.20	0.80	0.65	0.52	0.35	0.26	0.18	0.14
C-5	$\theta_{max}('')$	2.22	1.18	0.89	0.59	0.48	0.39	0.26	0.19	0.14	0.10
	$\theta_{min}('')$	1.80	0.96	0.72	0.48	0.39	0.31	0.21	0.16	0.11	0.083
C-6	$\theta_{max}('')$	1.34	0.72	0.54	0.36	0.29	0.23	0.16	0.12	0.082	0.061
	$\theta_{min}('')$	0.99	0.53	0.40	0.26	0.21	0.17	0.11	0.086	0.061	0.046
C-7	$\theta_{max}('')$	0.74	0.39	0.30	0.20	0.16	0.13	0.086	0.064	0.046	0.034
	$\theta_{min}('')$	0.67	0.36	0.27	0.18	0.14	0.12	0.077	0.058	0.041	0.031
C-8	$\theta_{max}('')$	0.50	0.27	0.20	0.13	0.11	0.087	0.058	0.043	0.031	0.023
	$\theta_{min}('')$	0.31	0.17	0.12	0.083	0.067	0.054	0.036	0.027	0.019	0.014
C-9	$\theta_{max}('')$	0.19	0.10	0.074	0.049	0.040	0.032	0.021	0.016	0.011	0.0085
	$\theta_{min}('')$	0.16	0.083	0.062	0.041	0.034	0.027	0.018	0.013	0.010	0.0071
C-10	$\theta_{max}('')$	0.14	0.076	0.057	0.038	0.031	0.025	0.017	0.012	0.0088	0.0066
	$\theta_{min}('')$	0.13	0.068	0.051	0.034	0.028	0.022	0.015	0.011	0.0078	0.0059

Table 1.4: Allowed ALMA 12-m Array configurations and their compatibility with the 7-m and TP Arrays (ACA).

Category	**Allowed 12-m Configurations**
Most Extended	C43-10
	C43-9 + C43-6
	C43-8 + C43-5
	C43-7 + C43-4
	C43-6 + C43-3 + ACA
	C43-5 + C43-2 + ACA
	C43-4 + C43-1 + ACA
	C43-3 + ACA
	C43-2 + ACA
Least Extended	C43-1 + ACA

1.2.2 Band 6 and Angular Resolution

The Band 6 receiver covers the 211 to 275 GHz spectral range (the 1.3 mm atmospheric window). It allowed an IF (Intermediate Frequency) range of 5-10 GHz, but since Cycle 6 it has been extended further to allow for multiple simultaneous line observations with more bandwidth per spw (Spectral Window); specifically for the ^{12}CO, ^{13}CO and C^{18}O $J = 2 - 1$ combination at 230.538/220.398/219.560 GHz, which has a minimum separation of 10.14 GHz. It now covers the range 4.5-10 GHz.

The angular resolution $\theta_{\rm res}$ of an interferometric array can be estimated in general with the following equation:

$$\theta_{\rm res} = \frac{k\lambda}{L_{\rm max}} \quad \text{[radians]} \tag{1.21}$$

where $\theta_{\rm res}$ is the FWHM of the main lobe of the synthesized beam; k is a factor that depends on the uv-plane weighing function[4]; λ is the observing wavelength in meters; and $\rm L_{max}$ is the longest baseline in meters. Via simulations using the ALMA notional configurations, the following equation was empirically determined:

$$\theta_{\rm res} = \frac{0.574\lambda}{L_{80}} \quad \text{[radians]} \tag{1.22}$$

where $\rm L_{80}$ is the 80$^{\rm th}$ percentile projected baseline uv-distance in meters. We have proved mathematically that the CO molecules that best trace the cold molecular gas content are CO$(1-0)$ and CO$(2-1)$, so it is now our interest to explain why CO$(2-1)$ is chosen over CO$(1-0)$, from an observational standpoint. The CO$(1-0)$ molecule has a rest frequency of 115.271 GHz ($\approx$ 2.6 mm), which means it is observed in Band 3, while the CO$(2-1)$ molecule has a rest frequency of 230.538 GHz ($\approx$ 1.3 mm), seen in Band 6. If we assume that both observations are made in the same physical antenna configuration ($\rm L_{80}$ is identical for both), we can set up a ratio between the resolutions:

$$\frac{\theta_{\text{res, Band 6}}}{\theta_{\text{res, Band 3}}} = \frac{\lambda_{\rm CO(2-1)}}{\lambda_{\rm CO(1-0)}} \approx 0.5 \tag{1.23}$$

Equation 1.23 shows that for any given ALMA configuration, the angular resolution in Band 6 (CO$(2-1)$) is half that of Band 3 (CO$(1-0)$). This implies that the observation of CO$(2-1)$ delivers twice the resolution that of CO$(1-0)$, providing a much enhanced view of the internal structures of galaxies, such as compact nuclear regions, without requiring a more extended, schedule-restricted antenna configuration. This is an important point when it comes to the observation of different molecules. As established earlier, the CO$(1-0)$ molecule is a cleaner cold molecular gas tracer than CO$(2-1)$ due to its lower critical density and excitation temperature, however, when observed, it presents severe operational constraints compared to CO$(2-1)$ due to the resolutions obtained from the different bands used by ALMA. This yields the conclusion that CO$(2-1)$ is the best molecule to observe the cold molecular gas, physically and observationally speaking.

[4]The uv-plane (or Fourier plane) is the mathematical space used to represent the data collected from the interferometer. The process of imaging reconstructs the sky brightness through Fourier Transforms.

Beyond the advantage in angular resolution, the choice between CO$(2-1)$ and CO$(1-0)$ is driven from an observational efficiency standpoint. Flux density S_ν is the power received from a source per unit area and per unit frequency. We can estimate this value for CO$(2-1)$ and CO$(1-0)$ at characteristic cloud temperatures of 10, 15 and 20 K. To do this, we must assume that we are in LTE and that the cloud is optically thick ($\tau \gg 1$), which is proven to be true in some cases (see Zschaechner et al., 2018). In this way we start from the expression

$$S_\nu = \int B_\nu(T)\, d\Omega. \tag{1.24}$$

Therefore, if we assume the source has uniform temperature,

$$S_\nu \propto \frac{\nu^3}{e^{h\nu/kT} - 1}. \tag{1.25}$$

With this, we can compute the flux density ratio between CO$(2-1)$ and CO$(1-0)$ as:

$$\frac{S_{\nu_{21}}}{S_{\nu_{10}}} = \left(\frac{\nu_{21}}{\nu_{10}}\right)^3 \times \left(\frac{e^{h\nu_{10}/kT} - 1}{e^{h\nu_{21}/kT} - 1}\right) \tag{1.26}$$

Because $\nu_{21} = 230.538$ GHz and $\nu_{21} = 115.271$ GHz, then $\nu_{21}/\nu_{10} \approx 2$. Now, let $x = h\nu_{10}/kT$, then

$$\frac{S_{\nu_{21}}}{S_{\nu_{10}}} = 8\left(\frac{e^x - 1}{e^{2x} - 1}\right). \tag{1.27}$$

Using $e^{2x} - 1 = (e^x - 1)(e^x + 1)$:

$$\frac{S_{\nu_{21}}}{S_{\nu_{10}}} = \frac{8}{e^{h\nu_{10}/kT} + 1} \tag{1.28}$$

Using $T = 10$ K:

$$\frac{S_{\nu_{21}}}{S_{\nu_{10}}} \approx 2.92 \tag{1.29}$$

Setting $T = 15$ K:

$$\frac{S_{\nu_{21}}}{S_{\nu_{10}}} \approx 3.26 \tag{1.30}$$

Finally, for $T = 20$ K:

$$\frac{S_{\nu_{21}}}{S_{\nu_{10}}} \approx 3.46 \tag{1.31}$$

Thus, for gas that has sufficient temperature and density to excite the $J = 2$ state, the CO$(2-1)$ line is inherently brighter (in Jy/beam) than the CO$(1-0)$ line due to its higher emission frequency at characteristic cold molecular gas temperatures. When combined with the exceptional sensitivity of ALMA's receivers, achieving the desired Signal-to-Noise Ratio (SNR) at a given resolution requires less time in Band 6 than in Band 3.

1.3 Motivation of the Study

As has been mentioned throughout this work, numerous efforts have been made to study the molecular gas content in AGN to ascertain the effects of feedback produced by these sources. Samples are often limited to specific targets or consider a selection from optical/soft X-ray that can be biased to the most obscured AGN, which can host large amounts of cold molecular gas. This is why for this work, we survey a sample of 18 obscured and unobscured hard X-ray selected AGN from the BAT AGN Spectroscopic Survey (BASS, Koss et al., 2017; Ricci et al., 2017; Oh et al., 2022). The sample consists of low redshift galaxies ($z \lesssim 1$) such that the outflowing gas is spatially resolved down to sub-parsec scales. To achieve this, we use integral field spectrograph[5] MUSE and the interferometer ALMA at subparsec spatial resolutions to study how the ionized outflow characterized from MUSE analysis (Kakkad et al., 2022) is related to their molecular gas contents present here. The combination of $[OIII]_{\lambda 5007}$ MUSE and $CO(2-1)$ ALMA observations in this unique sample allow us to trace the outflow structure in detail and in different gas phases for a representative AGN population, one of the main limitations in previous studies. Additionally, this sample has plenty of ancillary data at different wavelengths, that allow us to characterize their host galaxies and explore feedback effects with a unique view. We seek to characterize cold molecular gas content in our targets using estimations from Gaussian fits to the $CO(2-1)$ emission lines, as well as moment map analysis, $CO(2-1)$ surface brightness radial profiles, VLA radio continuum emission correlations with our cold molecular mass data, and 3D tilted-ring modeling in search for molecular outflows, studying the possible correlation with its ionized counterpart. We also study correlations between molecular gas properties, such as the derived M_{H_2} mass and $FWHM_{CO}$ with the bolometric luminosity L_{bol}, black hole mass M_{BH} and Eddington ratio λ_{edd}.

This document is organized as follows: Sec. 2 describes the sample. In Sect. 3, we report the analysis procedures followed by the results in Sect. 4. We discuss the implications of the results in Sect. 5, and the summary and conclusions are presented in Sect. 6.

[5]Integral Field Unit (IFU) is an specialized instrument used to perform integral field spectroscopy, which is a technique that captures the full spectrum (spectral axis) for every pixel in a 2D image (spatial axis) simultaneously. This product is known as a data cube, which is a 3D array that stores a complete spectrum for every pixel in a field of view.

Chapter 2

Sample

2.1 The BASS survey

The BAT AGN Spectroscopic Survey (BASS, Koss et al., 2017; Ricci et al., 2017; Koss et al., 2022) is an ambitious, large-scale multi-wavelength survey designed to study hard X-ray-detected AGN in the local universe ($z < 2$). The Burst Alert Telescope (BAT, Barthelmy et al., 2005) instrument on the Neil Gehrels Swift Observatory (Gehrels et al., 2004) provides a high-sensitivity all sky hard X-ray survey to sources such as AGN. The BASS survey is the follow-up of $\gtrsim$ 1000 BAT AGN with the aim to uniformly determine AGN properties via continuum, emission and absorption line measurements in multiple wavebands. Consequently, the BASS survey has an abundance of multi-wavelength ancillary data, which allowed the calculation of quantities such as the intrinsic X-ray luminosity and column density (Ricci et al., 2017), black hole mass, bolometric luminosity and Eddington ratio (see Koss et al., 2017; Lamperti et al., 2017; Oh et al., 2017). The high data quality and uniform measurement of black hole and host galaxy properties makes the BASS survey an ideal sample for our work.

2.2 The Selection Criteria

Hard X-ray selection offers the least biased AGN selection due to the low contamination from other sources within galaxies and the high penetration ability of hard X-rays up to large gas column densities (see Ricci et al., 2015). The targets analyzed in this study were selected based on their hard X-ray emission (14-195 keV) from the 70-month Swift-BAT AGN catalog (Baumgartner et al., 2013), with resolved ionized outflows traced by the $[OIII]_{\lambda5007}$ emission lines from the Multi Unit Spectroscopic Explorer (MUSE) instrument (see Kakkad et al., 2022 for more detail), which limits the sample to 18 AGN. Due to missing data cubes, this sample had to be reduced to 22 AGN (Table 2.1). Additionally, they have multi-band ancillary data based on the extensive follow-up studies by the BASS, which make the sample representative in the nearby universe, with $L_{bol} = 10^{42} - 10^{46}$ erg s^{-1}, $\log(M_{BH}/M_{\odot}) = 5.1 - 8.8$, $\log(\lambda_{Edd}) = -3 - 0$, and $\log(N_H/cm^{-2}) = 20.0 - 25.4$ (Koss et al., 2022), including a dedicated X-ray spectral analysis (Ricci et al., 2017) that allow us to include well-defined AGN power tracers in our analysis.

We complement the CO measurements with various galaxy and AGN physical properties from

the BAT AGN Spectroscopic Survey (BASS[1], Koss et al., 2017; Ricci et al., 2017; Koss et al., 2022; Oh et al., 2022). In particular, we use the following information:

(i) BAT ID (Target identifier in the BAT survey)[2]

(ii) Target Name (Optical/IR counterpart name of BAT AGN)

(iii) RA and DEC in J2000 (right ascension and declination of the optical/IR counterpart of the BAT AGN)

(iv) AGN type: (Seyfert type based on diagnostic diagrams, Koss et al., 2022; Oh et al., 2022); redshift (based on optical emission-line fitting, mainly of $[OIII]_{\lambda5007}$, Koss et al., 2022; Oh et al., 2022)

(v) Intrinsic X-ray fluxes and AGN Photon index (Γ) from dedicated X-ray spectral analysis (Ricci et al., 2017)

(vi) Bolometric luminosity L_{bol}; Black Hole Mass M_{BH}; Eddington ratio λ_{Edd}; column density (N_H).

Table 2.1: Properties of BASS ALMA sample. (1) *Swift*-BAT 70 month hard X-ray survey ID; (2) Counterpart name of target; (3) & (4) Optical coordinates of the target (Koss et al., 2017); (5) Redshift of the source measured with the $[OIII]_{\lambda5007}$ line; (6) Distance to the galaxy; (7) AGN type; (8) Black hole mass; (9) Bolometric luminosity; (10) Eddington ratio. (5), (6), (7), (8), (9) & (10) are obtained from Table 9 Koss et al. (2022)

BAT ID	Target Name	RA (deg)	DEC (deg)	$z_{[OIII]}$	Distance (Mpc)	Type	log M_{BH} log ($M_\odot$)	log L_{bol} log (erg s^{-1})	log L/L_{edd}
(1)	(2)	(3)	(4)	(5)	(6)	(7)	(8)	(9)	(10)
57	3C033	01:08:52	+13:20:14	0.0594	266.0	Sy2	8.83	45.32	-1.68
58	NGC 424	01:11:27	-38:05:00	0.0108	51.0	Sy1.9	7.49	44.22	-1.44
62	IC 1657	01:14:07	-32:39:03	0.0116	48.3	Sy2	7.68	43.51	-2.35
127	HE 0224-2834	02:26:25	-28:20:58	0.0598	268.0	Sy1	7.98	44.90	-1.25
134	NGC 985	02:34:37	-08:47:17	0.0430	190.3	Sy1	8.11	44.97	-1.32
197	HE 0351+0240	03:54:09	+02:49:30	0.0355	156.4	Sy1	7.18	44.41	-0.94
213	HE 0412-0803	04:14:52	-07:55:39	0.0382	168.6	Sy1	8.05	44.65	-1.58
216	NGC 1566	04:20:00	-54:56:16	0.0047	17.9	Sy1	6.83	42.73	-2.27
653	NGC 4941	13:04:13	-05:33:05	0.0039	20.4	Sy2	7.00	42.89	-2.29
703	Mrk 463	13:56:02	+18:22:18	0.0501	222.9	Sy1.9	6.72	44.75	-0.15
711	Circinus	14:13:09	-65:20:20	0.0015	4.2	Sy2	6.23	42.96	-1.44
731	NGC 5643	14:32:40	-44:10:28	0.0040	12.7	Sy2	6.43	43.62	-0.98
783	NGC 5995	15:48:24	-13:45:27	0.0248	108.3	Sy1	7.77	44.62	-1.33
817	2MASX J1631+2352	16:31:15	+23:52:57	0.0591	264.6	Sy1.9	8.11	44.75	-1.54
1051	3C403	19:52:15	+02:30:24	0.0584	261.2	Sy2	8.83	45.41	-1.59
1092	IC 5063	20:52:02	-57:04:07	0.0113	45.9	Sy2	8.24	44.19	-2.22
1151	3C445	22:23:49	-02:06:13	0.0561	250.4	Sy1	7.89	45.46	-0.60
1183	Mrk 926	23:04:43	-08:41:08	0.0477	211.9	Sy1	7.98	45.62	-0.54

[1]https://www.bass-survey.com/
[2]https://swift.gsfc.nasa.gov/results/bs70mon/

2.2.1 ALMA Sample

A follow-up of the 22 AGN analyzed with MUSE (Kakkad et al., 2022) was performed with ALMA during Cycle 8 in Band 6 (211–275 GHz) to map the ^{12}CO($J = 2 - 1$) emission (Program 2021.1.01150.S, PI: A.F. Rojas). These observations were conducted between November 2021 and December 2022. We requested a nominal synthesized beam of 0.3" and for extended galaxies the Observing Tool (OT) added two 12-m configurations, as well as 7m and TP arrays, in order to sufficiently resolve CO emission at higher spatial resolution, while recovering most of the flux at large scales. The requested resolution parameters included velocity resolution, which was chosen to be 20 km/s in order to detect the wings of the CO($2 - 1$) line tracing outflowing gas, and synthesized beams from $0.2 - 0.3$" to $0.7 - 0.9$" in order to best compare the results to the previous MUSE analysis, one of the main goals of this survey. The correlator setup was configured in the two sidebands in dual-polarization mode to provide a total frequency coverage spanning roughly 7.5 GHz. One of the four basebands was centered on the CO emission (rest frequency 230.58 GHz) with a more granular resolution of 1128.906 Hz to precisely map the peak of the redshifted line emission within the $\sim$ 1.875 GHz bandwidth. The remaining three basebands were centered at 228, 215, and 213 GHz with a more coarse spectral resolution of 31.250 MHz in order to map the continuum emission.

In Table 2.2, we show the array configurations used for the 18 AGNs of our sample, along with the parameters obtained for each target.

Table 2.2: Observational parameters achieved for the BASS ALMA sample. (1) Counterpart name of target; (2) Frequency observed (not redshift corrected); (3) Synthesized beam size, as Minor/Major beam, respectively; (4) RMS sensitivity achieved; (5) Total observation time for the target. Note that, for the full array combination, the total time is not equal to the sum of the individual times because TP and 7-m Array observations are run in parallel. Therefore, total time is 12-m + ACA; (6) Configuration used in the 12-m Array; (7) Usage of the 7-m Array; (8) Usage of the Total Power Array.

Target Name	Representative Frequency (GHz)	Synthesized Beam (")	RMS Sensitivity (μJy)	Total On-source Time (hours)	12-m Array Config.	7-m Array	TP Array
(1)	(2)	(3)	(4)	(5)	(6)	(7)	(8)
3C 33	217.5677	0.3250 – 0.2850	632.52 – 741.01	0.7	C43-5	No	No
NGC 424	227.8403	0.6135 – 0.6940	1100 – 1140	0.6	C43-5 + C43-2	No	No
IC 1657	227.8046	0.5146 – 0.6422	1100 – 1140	0.6	C43-5 + C43-2	No	No
HE 0224-2834	217.4886	0.3408 – 0.4164	599.81 – 685.47	0.7	C43-5	No	No
NGC 985	220.8934	0.2746 – 0.3226	1130 – 1630	0.4	C43-5	No	No
HE 0351+0240	222.5270	0.1255 – 0.1903	1160 – 1230	0.4	C43-6	No	No
HE 0412-0803	222.0983	0.3664 – 0.4754	1130 – 1260	0.4	C43-5	No	No
NGC 1566	229.3827	0.7605 – 0.8565	1180 – 1270	0.6	C43-5 + C43-2	No	No
NGC 4941	229.6875	0.7308 – 0.9447	1100 – 1150	1.1	C43-5 + C43-2	Yes	No
Mrk 463	219.4801	0.3456 – 0.4953	897.21 – 1000	0.5	C43-5	No	No
Circinus	230.2044	0.3713 – 0.4718	1210 – 1280	1.1	C43-5 + C43-2	Yes	Yes
NGC 5643	229.6218	0.4063 – 0.5052	1100 – 1170	1.1	C43-5 + C43-2	Yes	No
NGC 5995	224.7659	0.2992 – 0.4885	1130 – 1200	0.4	C43-5	No	No
2MASX J1631+2352	217.6570	0.3310 – 0.4521	642.76 – 732.90	0.7	C43-5	No	No
3C 403	217.6941	0.4658 – 0.5567	647.28 – 717.87	0.7	C43-5	No	No
IC 5063	227.9679	0.3970 – 0.4832	1160 – 1210	0.6	C43-5	No	No
3C 445	218.2315	0.2803 – 0.3308	709.77 – 760.42	0.6	C43-5	No	No
Mrk 926	220.1849	0.2823 – 0.3021	990.15 – 1070	0.4	C43-5	No	No

Chapter 3

Analysis

On this chapter, we describe the methods used to analyze the cold molecular gas in our galaxy sample, along with the kinematic specs. We use Gaussian fits, moment maps, radial profiles and VLA contours for the morphological analysis, while ^{3D}BBarolo (Di Teodoro & Fraternali, 2015) was used to perform the kinematic analysis on selected galaxies from our sample. We use these tools to understand the presence of outflows/inflows in our targets with CO$(2-1)$ detections and to characterize the cold molecular gas content in our targets. Throughout our work, we adopt cosmological parameters $H_0 = 70$ km s^{-1} Mpc^{-1}, $\Omega_\Lambda = 0.7$ and $\Omega_\mathrm{M} = 0.3$ (approximated from Planck Collaboration et al., 2020).

3.1 Morphological Properties

3.1.1 CO$(2-1)$ Emission: Gaussian fits and estimation of the Flux-Luminosity

Gaussian fits are mathematical processes that match a bell-shaped Gaussian curve to a set of data points. In the case of our CO$(2-1)$ emission lines, they follow a similar shape, so fitting a Gaussian curve to them will allow us to identify the center, the FWHM and amplitude (peak flux) of the emission line.

To do this we use the fitting tool in CARTA v5.0.3 (Comrie et al., 2026; Wang et al., 2026), which allows us to fit multiple Gaussians to an emission line (e.g. see Combes, F. et al., 2013; Marconcini, C. et al., 2025, where they fit a broad and narrow component to the [Ne V] transition line). These fits were performed on the spectrum extracted over the full spatial extent of the galaxy, as defined by the CO$(2-1)$ moment 0 map. For mergers or galaxies with difficult morphologies, we performed different Gaussian fits to the regions separately to sum up the total CO$(2-1)$ content (see Figs. 7.1-7.17). We used up to 6 Gaussian components, motivated and tested by performing a reduced χ^2 test on different numbers of components, following the usual structure:

$$\chi^2 = \sum_{i=1}^{N} \frac{(O_i - E_i)^2}{\sigma_i^2} \tag{3.1}$$

where O_i is the flux from channel i, E_i is the predicted flux from the model fit at channel i, σ_i is the rms (root mean square) noise and N the number of channels included in the fit. The

reduced χ^2, χ^2_ν is then

$$\chi^2_\nu = \frac{\chi^2}{\nu}, \tag{3.2}$$

where $\nu = N - p$ with p the number of free parameters in the model. For each Gaussian component, $p = 3$. The rms noise is estimated using the mean rms value extracted from 40 channels, ranging from the 10th channel to the 50th in the data cube. In Fig. 3.1 we show the results between using a single component or a double component to fit a single emission line.

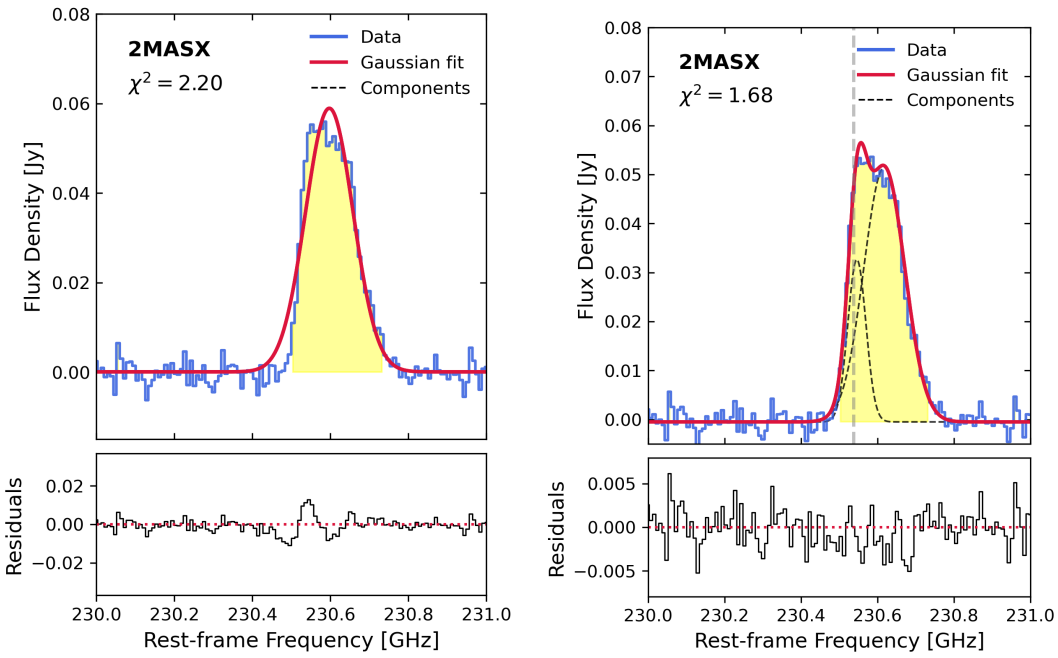


Figure 3.1: χ^2 test for a single and double component Gaussian fit.

To see how many Gaussian components are needed to perform a good fit to the emission line, we use the Bayesian Information Criterion (BIC). It is a statistical tool used to select the best model from a set of candidates. It balances model fit with complexity by penalizing models with more parameters to prevent overfitting. It is calculated as follows:

$$\mathrm{BIC} = k\ \ln(N) + \chi^2 \tag{3.3}$$

where k is the number of parameters the model uses (amplitude, centers, widths and the baseline), N is the number of channels, and χ^2 is the total chi-squared of the fit. For models A and B, the criterion is as follows:

$$\Delta\mathrm{BIC} = \mathrm{BIC_B} - \mathrm{BIC_A} \tag{3.4}$$

If $\Delta\mathrm{BIC} < -10$, then model B is strongly preferred over model A. Similarly, if $\Delta\mathrm{BIC} > 10$, model A is strongly preferred over model B. If ΔBIC is between -10 and 10, then the test is inconclusive. In the latter case, we select the fit that uses the least components.

With the information obtained from the Gaussian fit to the CO line, it is possible to measure

the CO line luminosity, $L'_{\mathrm{CO(2\text{-}1)}}$ in units of K km s^{-1} pc^2, from the integrated line fluxes following the relation given in Solomon et al. (1997).

$$L'_{\mathrm{CO(2\text{-}1)}} = 3.25 \times 10^7 S_{\mathrm{CO(2\text{-}1)}} \nu_{\mathrm{obs}}^{-2} \frac{D_{\mathrm{L}}^2}{(1+z)^3} \tag{3.5}$$

where ν_{obs} the observed frequency in GHz, $\mathrm{D_L}$ the luminosity distance in Mpc and z the redshift of the target and $S_{\mathrm{CO(2\text{-}1)}}$ is the total integrated CO line flux in units of [Jy km s^{-1}]. To compare our results with recent molecular gas studies based on the CO$(1-0)$ transition, we must calculate the luminosity $L_{\mathrm{CO(1\text{-}0)}}$ from the CO$(2-1)$ transition assuming a line ratio of $r_{21} = 0.79$ (Saintonge et al., 2017):

$$L_{\mathrm{CO(1\text{-}0)}} = \frac{L'_{\mathrm{CO(2\text{-}1)}}}{0.79} \tag{3.6}$$

Then, we can estimate the molecular gas mass $M_{\mathrm{H_2}}$ using the α_{CO} CO-to-$\mathrm{H_2}$ conversion factor, corresponding to the value measured for self-gravitating molecular clouds in galaxy disks, following Bolatto et al. (2013):

$$M_{\mathrm{H_2}}(M_\odot) = \alpha_{\mathrm{CO}} \times L_{\mathrm{CO(1\text{-}0)}}, \tag{3.7}$$

where $\alpha_{\mathrm{CO}} = 4.3\ M_\odot$ (K km s^{-1} pc^2)$^{-1}$ in the Milky Way (Bolatto et al., 2013) and for the lower J transitions of CO [e.g. CO$(1-0)$, CO$(2-1)$], $\alpha_{\mathrm{CO}} \approx 0.6 \pm 0.2\ M_\odot$ (K km s^{-1} pc^2)$^{-1}$ (Papadopoulos et al., 2012). Therefore, a good estimation would be to use $\alpha_{\mathrm{CO}} = 4.3$ as an upper limit for the molecular mass, and $\alpha_{\mathrm{CO}} = 0.8$ as a lower limit.

To obtain the galaxy's redshift we use the value found in Table 9 of Koss et al. (2022), while the D_{L} was calculated using the NED Wright's Javascript Cosmology Calculator (Wright, 2006), using the Planck Collaboration et al. (2020) cosmology mentioned above.

We can derive an expression for $S_{\mathrm{CO(2\text{-}1)}}$ starting from a typical normal distribution

$$f(x) = Ae^{-\frac{(x-x_0)^2}{2\sigma^2}}, \tag{3.8}$$

where A is the amplitude. We are interested in the area that gives the total integrated flux ($S_{\mathrm{CO(2\text{-}1)}}$):

$$\mathrm{Area} = \int_{-\infty}^{\infty} Ae^{-\frac{(x-x_0)^2}{2\sigma^2}} dx \tag{3.9}$$

We use a variable change to use the prescription for a Gaussian integral:

$$\int_{-\infty}^{\infty} dx\ e^{-\alpha x} = \sqrt{\frac{\pi}{\alpha}} \tag{3.10}$$

Let u^2 be

$$u^2 = \frac{(x-x_0)^2}{2\sigma^2} \quad \rightarrow \quad u = \frac{x-x_0}{\sqrt{2}\sigma} \tag{3.11}$$

therefore:

$$du = \frac{dx}{\sqrt{2}\sigma} \quad \rightarrow \quad dx = \sqrt{2}\sigma du \tag{3.12}$$

Replacing in Eq. (2.3):

$$S_{\mathrm{CO(2\text{-}1)}} = \sqrt{2}A\sigma \int_{-\infty}^{\infty} e^{-u^2} du = \sqrt{2\pi}A\sigma \tag{3.13}$$

By definition, the FWHM is the distance between two points x where the amplitude is half of the height $(A/2)$. This means:

$$f(x) = A/2 \quad \rightarrow \quad Ae^{-\frac{(x-x_0)^2}{2\sigma^2}} = A/2 \tag{3.14}$$

Solving for $(x - x_0)$ yields:

$$(x - x_0) = \pm\, \sigma\sqrt{2\,\ln 2} \tag{3.15}$$

We simplify things by shifting the gaussian to the center $(x_0 = 0)$:

$$x = \pm\, \sigma\sqrt{2\,\ln 2} \tag{3.16}$$

Now, the FWHM will be the distance between x and $-x$:

$$\mathrm{FWHM} = \sigma\sqrt{2\,\ln 2} - (-\sigma\sqrt{2\,\ln 2}) \;=\; 2\sigma\sqrt{2\,\ln 2} \tag{3.17}$$

This way, we now have an expression for σ in terms of the FWHM:

$$\sigma = \frac{\mathrm{FWHM}}{2\sqrt{2\ln 2}} \tag{3.18}$$

Plugging this into our $S_{\mathrm{CO(2\text{-}1)}}$ expression:

$$S_{\mathrm{CO(2\text{-}1)}} = A\frac{\sqrt{\pi}}{2\sqrt{\ln 2}}\mathrm{FWHM} \tag{3.19}$$

By definition, the amplitude A is the peak flux of the line. Finally, we get our final expression:

$$S_{\mathrm{CO(2\text{-}1)}} = \frac{\sqrt{\pi}}{2\sqrt{\ln 2}}\mathrm{Flux}_{\mathrm{CO(2\text{-}1)}}\mathrm{FWHM}_{\mathrm{CO(2\text{-}1)}} \tag{3.20}$$

with $\mathrm{Flux}_{\mathrm{CO(2\text{-}1)}}$ the peak flux of the $\mathrm{CO}(2-1)$ line emission. In CARTA, this equation is given as the integral of function, so we don't need to calculate it.

The estimations of $S_{\mathrm{CO(2\text{-}1)}}$ and $L'_{\mathrm{CO(2\text{-}1)}}$ will be made for each Gaussian component and then summed with their respective errors. Similar proceedings are followed for the estimation of $\mathrm{FWHM}_{\mathrm{CO}}$ (see Esposito, Federico et al., 2024).

We collect data from the fit, straight from CARTA and then plot the redshift-corrected results with the residuals and χ^2_ν to analyze the goodness of the fit. We will study correlations between parameters ($M_{\mathrm{H_2}}$ and $\mathrm{FWHM}_{\mathrm{CO}}$) with bolometric luminosity L_{bol}, black hole mass M_{BH} and Eddington rate λ_{edd}.

3.1.2 Moment Maps

Moment maps are crucial for our work as they allow us to characterize the cold molecular gas content and distribution with the integrated intensity maps (moment 0), rotation velocity and patterns with the intensity-weighted mean velocity field maps (moment 1) and velocity dispersion maps (moment 2).

To synthesize our moment maps for the sample, we use `bettermoments` (Teague & Foreman-Mackey, 2018), a python tool that creates moment maps of spectral line data. To extract cleaner maps, we use the masking option to cut noisy channels from the cube and select only those that show prominent CO$(2-1)$ emission. Channel selection is performed using the spectral profiler built in CARTA. The threshold clipping option is also used to perform adequate S/N cuts to the maps, based on the resolution of the cube; those galaxies with lower resolutions received a 3-4 σ cut, while the ones with higher resolution were cut from 6 up to 25σ. We added a bar for the physical scale reference in the bottom right panel and the beam in the bottom left panel. All moment maps are corrected for systemic velocity and redshift. The systemic velocity was obtained from the median velocity of the moment 1 FITS file.

3.1.3 Radial Profiles

Radial profiles allow us to identify where CO$(2-1)$ emission is most concentrated in the galaxy by using the surface brightness $\Sigma_{\mathrm{CO(2\text{-}1)}}$ as our indicator.

For our radial profiles and inclination estimations, we use `photutils` (Bradley et al., 2016), a Python library that provides commonly-used tools and key functionality for detecting and performing photometry of astronomical sources. Tools are provided for background estimation, star finding, source detection and extraction, aperture photometry, PSF photometry, image segmentation, centroids, radial profiles, and elliptical isophote fitting. It is a coordinated package of Astropy and integrates well with other Astropy packages, making it a powerful tool for astronomical image analysis.

For our analysis, we use the Elliptical Isophote Analysis tool `photutils.isophote`, which is a package that provides tools to fit elliptical isophotes to a galaxy image, which iterates for the best fit to a certain position angle of a galaxy and models the best elliptical contour of the galaxy. We use this tool on the 3σ cut zeroth moment map, and based on the ellipse information, we broadly estimate the inclination angle of the disk following the formula in Hubble (1926)

$$\cos^2 i = \frac{(b/a)^2 - q_0^2}{1 - q_0^2}, \tag{3.21}$$

where in our case, we consider a thin disk geometry, implying that $q_0 = 0$. We must take into account that this assumption gives uncertain results if a galaxy is close to edge-on, but for our purposes, it serves as a good approximation. We use this same ellipse information given to obtain the PA. We use kpc as the radial scale instead of arcseconds to better understand the physical morphology of the galaxies.

On the other hand, we use the Elliptical Aperture and EllipticalAnnuli tools to compute the radial profiles for each target. The separation between each annuli is of 1 pixel, and they must cover the galaxy as a whole. In order to center the elliptical annuli, central coordinates of the AGN are obtained from NED. We added a bar for the physical scale reference in the bottom right

panel and the beam in the bottom left panel.

3.1.4 Contour Maps with VLA radio emission

Contours from radio continuum observations were overlaid on moment 0 maps to compare the radio emission with our observations, using 1", 3" and 6" apertures. Data were obtained using the *Karl G. Jansky Very Large Array (VLA)*, see Ilha et al. (2025) and Kader et al. (2026). The images correspond to 22 GHz frequency observations obtained with the C configuration of the VLA. We did this for galaxies HE 0412-0803, Mrk 926, NGC 985, NGC 4941 and NGC 5995, which were the only ones in our sample that had these observations. Contours were drawn at 3σ, 4σ, 8σ, 16σ, 32σ, 64σ, 128σ and 256σ, where σ represents the rms noise of each image; negative contours were not included.

3.2 Kinematics

3.2.1 ^{3D}BBarolo

One of the main purposes of this study is to characterize possible cold molecular gas outflows/inflows in our galaxy sample. To see these non-circular movements, we use detailed 3D kinematic models with ^{3D}BBarolo (Di Teodoro & Fraternali, 2015). ^{3D}BBarolo (3D-Based Analysis of Rotating Object via Line Observations) or BBarolo is a tool for fitting 3D tilted-ring models to emission-line data-cubes. The algorithm employs a concentric tilted rings model and performs a Monte Carlo-based three-dimensional fitting to reproduce the observed emission, allowing ^{3D}BBarolo to derive the kinematics of any disk-like object, including galaxy disks, circumnuclear disks, accretion disks and proto-planetary disks, able to reproduce the data of emission line data such as HI, molecular, and recombination lines. The models created by BBarolo allow us to check for non-circular motion regions in the galaxy in the residuals. The 3D fitting and modeling was performed to a selected group of galaxies, motivated by their resolution and disk-like morphologies. These galaxies are the Circinus Galaxy, IC 1657, IC 5063, NGC 1566, NGC 4941, NGC 5643, and NGC 5995, as they all have exceptional resolutions that allow us to use BBarolo without the risk of getting bad fits owing to unresolved emission and noise.

We follow a standard fitting procedure for all targets. We use the ALMA CO(2−1) data cubes as input, and start by fixing initial parameters such as the center of the rotating disk (`XPOS`, `YPOS`) and systemic velocity $V_{\rm sys}$ (estimated through the source finding algorithm ^{3D}BBarolo, as the estimated value is trustworthy. See ^{3D}BBarolo documentation[1]). The INC angle of each tilted ring is treated as a free parameter, whereas the PA will be either fixed or set free, depending on the morphology of the galaxy. Initial guesses for both parameters are obtained from the isophote `photutils` analysis. The parameters `NRADII` (number of rings) and `RADSEP` (angular separation between rings) together define the area covered by the fitting. For each galaxy, several combinations are tested to provide good fitting quality and sufficiently extensive coverage. Because we are working with good resolution data cubes, no constrain was made on the rotational velocity $V_{\rm rot}$ nor the velocity dispersion $V_{\rm disp}$. Because of this, we also use the `THRESHOLD` mask, that uses flux instead of SNR to obtain the mask. We adopted the `AZIMUTHAL` normalization method, as recommended

[1] https://bbarolo.readthedocs.io/en/latest/

by ^{3D}BBarolo (see Di Teodoro & Fraternali, 2015), and set `TWOSTAGE = True` to achieve better convergence on the INC and PAs. All other parameters are kept at their default values. The final output of the algorithm includes moment maps, PV diagrams and a table summarizing the fitted parameters for each ring, including $V_{\rm rot}$, $V_{\rm disp}$, INC, PA and $V_{\rm sys}$. I personally added the reduced χ^2 of each fitted ring to discuss the goodness of each fit.

Chapter 4

Results

In the following chapter, we present the integrated and resolved CO($2-1$) properties of the galaxy sample, such as mass distribution, the CO line luminosity and kinematics from the analysis methods described in Sect. 3.

4.1 Molecular Gas Content

The Gaussian fits performed are shown in Figs. 4.1 and 7.1-7.17. For all targets, a reduced $\chi^2_\nu < 10$ is achieved. The highest χ^2_ν values correspond to targets with better resolution and lower redshift. One possible explanation is that, because these targets are closer to us than others in the sample, small differences between the model and the data result in large residuals. Consequently, small misalignment between the Gaussian component and the emission line will result in a large portion of the flux being left out, worsening the residuals and χ^2_ν.

As shown in Fig. 3.1, most targets required multiple Gaussian components to achieve an acceptable fit. While adding several Gaussian components traditionally increases uncertainties when estimating quantities such as $S_{\rm CO}$, FWHM$_{\rm CO(2\text{-}1)}$ and $L'_{\rm CO(2\text{-}1)}$, Table 4.1 shows that this is not the case. Multi-component fitting performed with CARTA yielded errors well within acceptable boundaries (e.g. Bothwell et al., 2013). Up to 6 Gaussian components were used for lines with non-Gaussian profiles (e.g. Circinus, IC 1657), keeping errors between $\sim 3.5\%$ and $\sim 5.5\%$. Targets such as 3C 33, 3C 403 and NGC 985 have the noisiest emission lines, yielding fit errors ranging from $\sim 14\%$ up to $\sim 31\%$. This is a clear indication that uncertainties are more sensitive to low resolution issues than to the amount of Gaussian components used in the fitting process.

From the BIC tests performed, we can confirm this approach; while adding a second component to certain emission lines yielded negligible improvement while increasing errors, other galaxies required more than 4 components to best represent the data. For some targets such as Circinus, the many components and non-Gaussian distribution in the emission lines may be due to physical processes such as absorption features and spiral arms, while a double-horned profile such as those from IC 1657 and NGC 1566 is directly related to rotating disk kinematics.

Particularly, galaxies with the highest $S_{\rm CO}$ and non-Gaussian emission lines are always best fitted with additional Gaussian components (see Tables 7.1 and 7.2), as residuals are substantial (e.g. NGC 1566, Circinus, NGC 5643). Note that these 3 galaxies in particular are the only ones that have $S_{\rm CO} > 400$ Jy km s^{-1}). Therefore, small differences in the fits of the emission lines from

these targets result in high variations in the reduced chi-squared χ^2_ν and residuals, as the BIC test suggests.

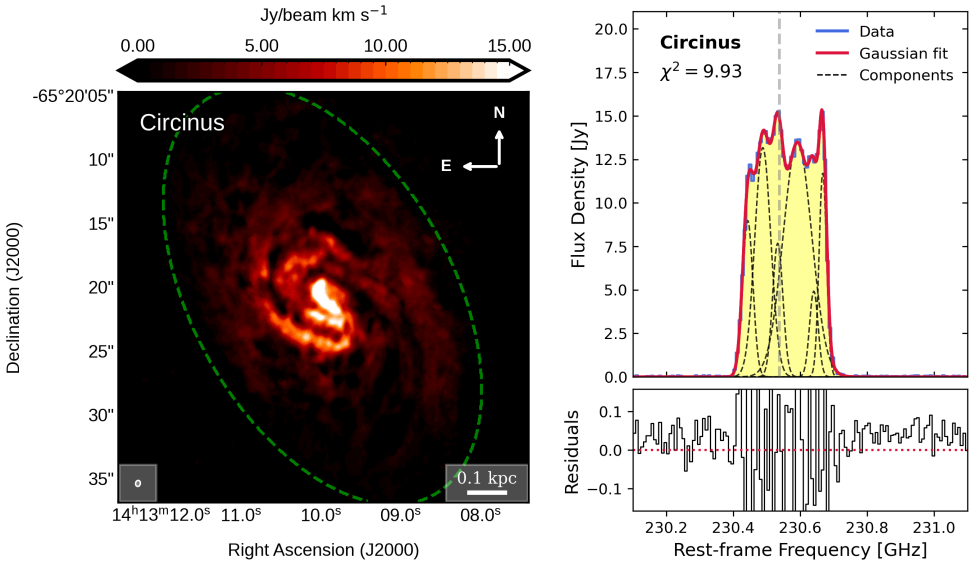


Figure 4.1: Gaussian fit for Circinus, whose $S_{\rm CO}$ value is among the highest from the sample. *Left panel*: Aperture selected (dotted green line) to obtain the emission line overlaid on the moment 0 map. The lines shown are selected by highest flux, as the presence of mergers requires multiple line fits at different regions. For disk-like galaxies, the line shown represents the total emission from the source. *Right panel*: Gaussian fit to the emission line. Solid blue lines represent the spectrum shape, black dotted lines represent the components used to perform the fit and the solid red line is the fitted spectrum. The reduced χ^2 is also added. Residuals are measured as 5σ. The yellow denotes that the line emission is above 3σ.

In Table 4.1 the derived quantities from the Gaussian fits are shown for each galaxy of the sample. As mentioned in Section 3.1.1, we assume a CO$(2-1)$/CO$(1-0)$ line ratio of $r_{21} = 0.79$ and standard galactic H_2-to-CO conversion factor of $\alpha_{\rm CO} = 0.8$ as our lower limit and $\alpha_{\rm CO} = 4.3$ (K km s^{-1} pc^2) as the upper limit. For mergers, the first conversion factor should better represent the molecular gas mass, while for spiral galaxies the latter serves as the best approximation.

Inclinations vary between 20 to 81 degrees, with mergers (NGC 985, HE 0412-0803, Mrk 463, 2MASX J1631+2352 and Mrk 926) lack inclination estimates due to complex, disturbed morphologies. It is important to note that for 3C 33 the inclination was measured from the central point shown on the moment 0 map (see Fig. 8.1), however the brightest component of the galaxy is the feature shown ~ 2 kpc to the east from the central bright spot.

The CO$(2-1)$ properties show a wide variety of contents. The total integrated line flux $S_{\rm CO}$ varies between 0.35 Jy km s^{-1} in the weakest detections and 561 Jy km s^{-1} in the strongest. Galaxies HE 0351+0240 and 3C 445 display no detectable CO$(2-1)$ emission. In terms of the total line width (FWHM), there are some distinctively narrow emission lines (e.g. 3C 33, HE 0412-0803 and NGC 5643), in contrast to others with FWHM $>$ 400 km s^{-1} (e.g. NGC 985, Mrk 463, NGC 5995 and Mrk 926), three of which are mergers, where broad, shock-like kinematic components are frequently observed (e.g. see Soto et al., 2012). $L'_{\rm CO(2\text{-}1)}$ values vary by ~ 1 order of magnitude, and are ~ 2 orders of magnitude smaller than in Bothwell et al. (2013). However,

the latter focused on sources at high redshift, which increases the values of $L'_{\mathrm{CO(2\text{-}1)}}$ as it is highly dependent on the redshift and luminosity distance (Eq. 3.5). Our $L'_{\mathrm{CO(2\text{-}1)}}$ range is fully consistent with local AGN samples (e.g. *XCOLD GASS*, Saintonge et al., 2017), spanning from gas-depleted systems to gas-rich environments.

With the values of $L'_{\mathrm{CO(2\text{-}1)}}$ we estimated molecular gas masses, shown in Table 4.2. Values vary from $1.2 \times 10^7 M_\odot$ to $8.2 \times 10^9 M_\odot$, with large molecular gas reservoirs seen in Mrk 463 and NGC 5995. These values are also consistent with the findings of Saintonge et al. (2017).

Table 4.1: Gaussian fit results and derived CO$(2-1)$ galaxy properties for the ALMA sample.

Target Name	z_{CO}	rms (mJy beam^{-1})	Inclination (deg)	S_{CO} (Jy km s^{-1})	FWHM$_{\mathrm{CO(2\text{-}1)}}$ (km s^{-1})	$L'_{\mathrm{CO(2\text{-}1)}}$ (10^8 K km s^{-1} pc^2)
3C 33	0.0587	0.4538	28 ± 5	0.35 ± 0.05	87.6 ± 16.5	0.14 ± 0.02
NGC 424	0.0117	0.609	56 ± 5	17.14 ± 1.14	196.8 ± 14.03	0.27 ± 0.02
IC 1657	0.0119	0.552	81 ± 5	139.2 ± 6.5	354.2 ± 18.1	2.22 ± 0.10
HE 0224-2834	0.0598	0.4551	64 ± 5	15.89 ± 1.18	334.3 ± 28.1	6.57 ± 0.49
NGC 985	0.0428	0.5106	-	15.77 ± 2.74	445.0 ± 141.5	3.32 ± 0.58
HE 0351+0240	-	0.8582	-	-	-	-
HE 0412-0803	0.0381	0.8617	-	7.16 ± 0.45	116.8 ± 9.6	1.19 ± 0.08
NGC 1566	0.0050	1.2933	42 ± 5	467.5 ± 8.9	234.7 ± 5.2	1.32 ± 0.03
NGC 4941	0.0036	0.8843	41 ± 5	80.00 ± 10.03	297.4 ± 23.3	0.12 ± 0.01
Mrk 463	0.0508	0.6418	-	50.88 ± 5.24	481.9 ± 58.5	15.13 ± 1.56
Circinus	0.0014	1.1916	57 ± 5	420.4 ± 23.1	367.0 ± 13.1	0.92 ± 0.05
NGC 5643	0.0040	1.6684	67 ± 5	561.1 ± 2.04	99.9 ± 0.4	1.01 ± 0.00
NGC 5995	0.0254	1.3581	67 ± 5	168.7 ± 6.64	470.4 ± 16.5	12.37 ± 0.49
2MASX J1631+2352	0.0588	0.6494	-	13.53 ± 0.73	238.1 ± 9.5	5.41 ± 0.29
3C 403	0.058	0.4661	45 ± 5	6.56 ± 1.07	348.9 ± 58.5	2.55 ± 0.42
IC 5063	0.0113	0.8292	75 ± 5	80.00 ± 2.18	390.3 ± 12.3	1.14 ± 0.04
3C 445	-	0.6059	-	-	-	-
Mrk 926	0.0471	0.8491	-	17.01 ± 0.80	424.8 ± 30.7	4.33 ± 0.20

We study the correlations between the molecular gas mass $M_{\mathrm{H_2}}$ and FWHM$_{\mathrm{CO(2\text{-}1)}}$ with galaxy parameters such as bolometric luminosity L_{bol}, black hole mass M_{BH} and the Eddington ratio λ_{edd} (see Fig. 4.2). We find a weak, positive correlation between the molecular mass and bolometric luminosity, as well as a stronger correlation with the Eddington ratio. For the FWHM, no strong correlations are seen, and neither does the molecular mass or the FWHM show correlations with the mass of the black hole. We compare with the results found in Koss et al. (2021), finding good agreement with the findings of that study.

Table 4.2: CO line luminosity and molecular gas mass properties derived using standard H_2-to-CO conversion factors (α_{CO}) as lower and upper limits (Downes & Solomon, 1998; Bolatto et al., 2013). Line luminosities $L_{CO(1\text{-}0)}$ are estimated from observed $CO(2-1)$ intensities assuming a line ratio $r_{21} = L'_{CO(2\text{-}1)}/L_{CO(1\text{-}0)} = 0.79$ (Saintonge et al., 2017).

Target Name	$L_{CO(1\text{-}0)}$ (10^8 K km s^{-1} pc^2)	M_{H_2} $10^8 M_\odot$; $\alpha_{CO} = 0.8$	M_{H_2} $10^8 M_\odot$; $\alpha_{CO} = 4.3$
3C 33	0.18 ± 0.02	0.14 ± 0.02	0.76 ± 0.11
NGC 424	0.36 ± 0.02	0.27 ± 0.02	1.44 ± 0.10
IC 1657	2.81 ± 0.13	2.25 ± 0.11	12.10 ± 0.57
HE 0224-2834	8.32 ± 0.62	6.66 ± 0.49	35.77 ± 2.66
NGC 985	4.20 ± 0.73	3.36 ± 0.58	18.05 ± 3.14
HE 0351+0240	-	-	-
HE 0412-0803	1.50 ± 0.09	1.20 ± 0.08	6.47 ± 0.41
NGC 1566	1.67 ± 0.03	1.33 ± 0.03	7.16 ± 0.14
NGC 4941	0.15 ± 0.02	0.12 ± 0.01	0.64 ± 0.08
Mrk 463	19.15 ± 1.97	15.32 ± 1.58	82.35 ± 8.48
Circinus	1.17 ± 0.06	0.94 ± 0.05	5.03 ± 0.28
NGC 5643	1.280 ± 0.005	1.024 ± 0.004	5.50 ± 0.02
NGC 5995	15.66 ± 0.62	12.53 ± 0.49	67.33 ± 2.65
2MASX J1631+2352	6.85 ± 0.38	5.48 ± 0.30	29.45 ± 1.61
3C 403	3.23 ± 0.53	2.59 ± 0.42	13.90 ± 2.26
IC 5063	1.46 ± 0.05	1.17 ± 0.03	6.27 ± 0.17
3C 445	-	-	-
Mrk 926	5.49 ± 0.26	4.39 ± 0.21	23.59 ± 1.11

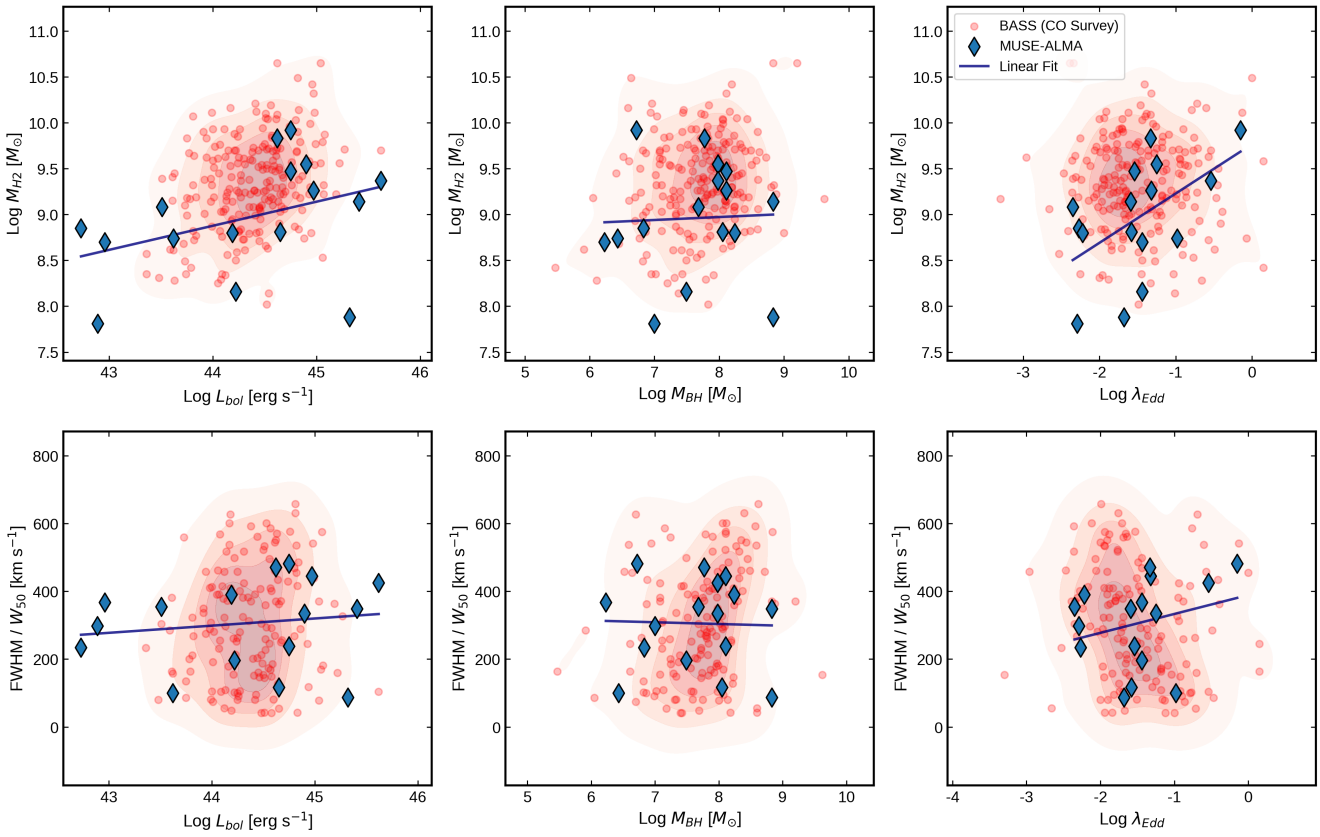


Figure 4.2: Correlations between the molecular gas mass $M_{\rm H_2}$ and $\rm FWHM_{CO(2\text{-}1)}$ with galaxy parameters. In red we plot the results from Koss et al. (2021), while in blue we plot our findings. The solid blue line is the linear fit to our data.

4.2 Spatial Distribution and Kinematics of CO$(2-1)$

The molecular gas distributions and kinematics are shown in the moment maps displayed in Figs. 8.1 - 8.6. Cold molecular gas emission is found in 16 of 18 targets ($\sim$ 89%) in our sample. Distributions vary from extended disks (e.g. NGC 1566, NGC 4941, Circinus) that span $\sim 1-5$ kpc across, dispersed (e.g. NGC 985, HE 0412-0803, Mrk 463, 2MASX 1631+2352) that span as much as $\sim$ 12 kpc, faint (e.g. 3C 33, Mrk 926) and in a ring-like shape (e.g. HE 0224-2834, 3C 403). As mentioned in Section 4.1, the only non detections are HE 0351+0240 and 3C 445, where in the latter the same point-like structure is seen as in the case of 3C 33. Two targets, Mrk 463 and IC 5063 (reported as mergers) possess two bright clumps, which have been categorized as a dual-system. For the 16 detections, cold molecular gas is found in galaxy centers, where in the brightest cases these reach up to 15 Jy/beam km s^{-1}, though most are in the $0.1-3$ Jy/beam km s^{-1} range. NGC 5643 presents a nuclear bar structure spanning $\sim$ 0.35 kpc that shows a direct correlation to its rotational motion.

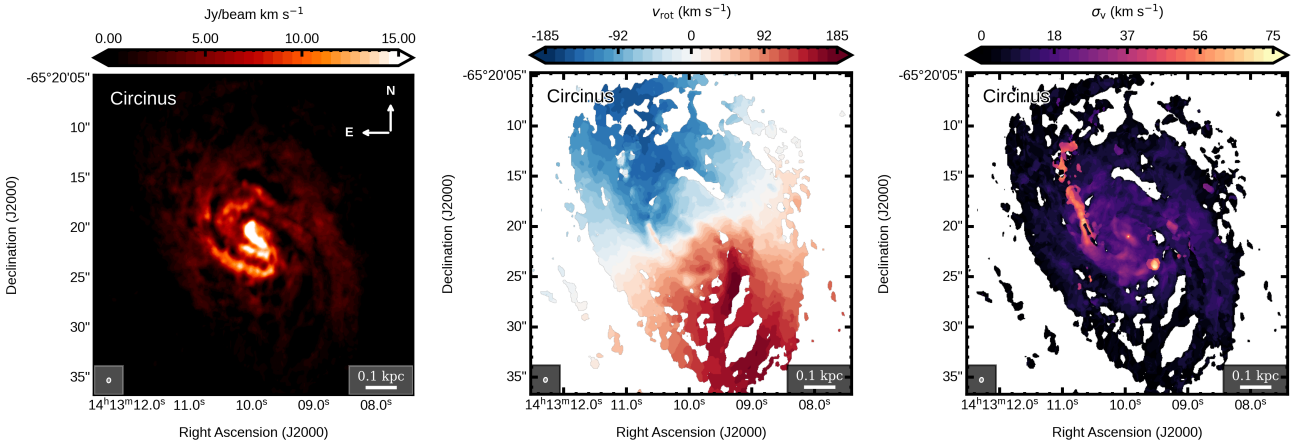


Figure 4.3: ALMA moment maps of cold molecular gas in the central ($\sim$ 1 kpc) region of the Circinus galaxy. *Left panel*: Integrated intensity map (Moment 0) showing an extended disk. *Middle panel*: Intensity-weighted mean velocity field (Moment 1) displaying a regular, large-scale disk rotation pattern. *Right panel*: Velocity dispersion map (Moment 2), exhibiting a high dispersion peak ($\sim$ 60 km s^{-1}) at the AGN position with a localized region of high velocity dispersion at $\sim$ 0.1 kpc southwest of the nucleus. A stream-like high dispersion feature is also located to the east of the nucleus, seen in the moment 1 map as well. Synthesized beam is found in the bottom-left corner, the scale is located at the bottom-right corner and the arrows on the top-right corner indicate North and East.

Similar to the molecular gas distributions, velocity fields and kinematics display significant diversity. While all detected targets follow some sort of rotational pattern, these range from rotating disks (e.g. IC 1657, NGC 1566, NGC 4941, Circinus) reaching $v_{\rm rot} \sim 170$ km s^{-1}, to mergers with complex motions (e.g. NGC 985, HE 0412-0803, Mrk 463), reaching velocities up to $v_{\rm rot} \sim 230$ km s^{-1} . The rings seen in HE 0224-2834 and 3C 403 seem to follow disk-like rotational patterns, with a distinguishable complexity in HE 0224-2834 as rotation seems to be slightly offset from the ring's major axis. Non-circular motion candidates are mostly mergers, such as NGC 985, IC 5063 and Mrk 463, as well as targets such as NGC 424, IC 1657, HE 0224-2834, and NGC

5643 that show velocity gradients which deviate from regular circular rotation patterns. Targets such as NGC 985 and Mrk 463 show complex and extreme velocity gradients, while in the other targets mentioned the geometry of the velocity contours seems to follow an S-shape, which could be indicative of streaming motions along a bar or spiral arm. Flat disk motions are observed in targets such as Circinus, where the geometry of the contour is straight and parallel. In some cases, such as 3C 403 and IC 5063, the zero-velocity line passes offset from the AGN position, possibly pointing out the decoupling between the kinematic center of the gas and the position of the SMBH.

High velocity dispersions are detected at the physical position of the AGN for all detections, peaking at ~ 120 km s^{-1}. Note that 3C 445 shows higher speeds, but the central point-like emission may represent an imaging artifact originating from the reduction process. In the mentioned dual-systems in Mrk 463 and IC 5063 this is clearly seen, where in the non-AGN of Mrk 463 (western lobe) the velocity dispersion is considerably lower than in the AGN (central lobe). One interesting feature seen from these maps is the eastern "stream" like structure in Circinus, as well as a high-velocity dispersion spot ~ 0.1 kpc south-west of the nucleus (Fig. 4.3). The stream-like structure can also be seen in the velocity field map; it appears as a rotational component in discrepancy with the overall rotational motion. In some targets (NGC 1566, NGC 4941, NGC 5643 and NGC 5995) the velocity dispersions appear to be slightly lopsided near the nucleus.

4.3 Radial Distribution of CO$(2-1)$

As mentioned in Section 3.1.3, we use the surface brightness $\Sigma_{\text{CO(2-1)}}$ as our indicator to analyze where the cold molecular gas is concentrated within our AGN sample. In Figs 9.1-9.7 the radial profiles for the ALMA sample are shown.

In general, surface brightness decreases from the center onto the most extended regions. Galaxies with prominent spiral arms (e.g. NGC 1566 and NGC 4941) show a decrease in surface brightness from the central regions, and then a rather constant slope where the spiral arms are located. In mergers, these diagrams are useful when characterizing bright spots far from the AGN. This is the case in the NGC 985, Mrk 463 and 2MASX J1631+2352 mergers, where prominent emission peaks are well represented in the radial profiles. For our two galaxies with molecular gas rings, 3C 403 and HE 0224-2834, only 3C 403 shows a major increase in $\Sigma_{\text{CO(2-1)}}$ on its outer regions ~ 4 kpc from the nucleus. This is because HE 0224-2834 has a ring-like structure west of the nucleus that is not symmetric to the central AGN, thus, this feature is not completely captured by the radial profile, showing a persistent decrease in flux with small fluctuations at ~ 4 kpc, same distance as where the ring in 3C 403 is located. A similar feature in the radial profile can be seen in NGC 424, where it shows a steep decline in surface brightness from the nucleus, with a significant increase at ~ 2 kpc where arm-like structures are located. These arms are not the same as the ring in 3C 403, but the reflected radial profile shows similar features. Another galaxy showing these increases in $\Sigma_{\text{CO(2-1)}}$ far from the central AGN is Mrk 926, where in the zeroth moment it is possible to see prominent emission towards the north-east of the nucleus, accounting for this "bump feature" seen in many profiles. Other galaxies such as IC 1657, Circinus and NGC 5643 show a monotonically decreasing profile, suggesting most of the emission comes from the central regions of the galaxy. As for NGC 5995, the gas distribution shows an important increase in molecular gas ~ 3 kpc from the center, more prominent than in those galaxies with spiral arms (NGC 1566 and NGC 4941). Radial profiles fail to capture the faintest emission as in the case of 3C 33, whose east-side feature

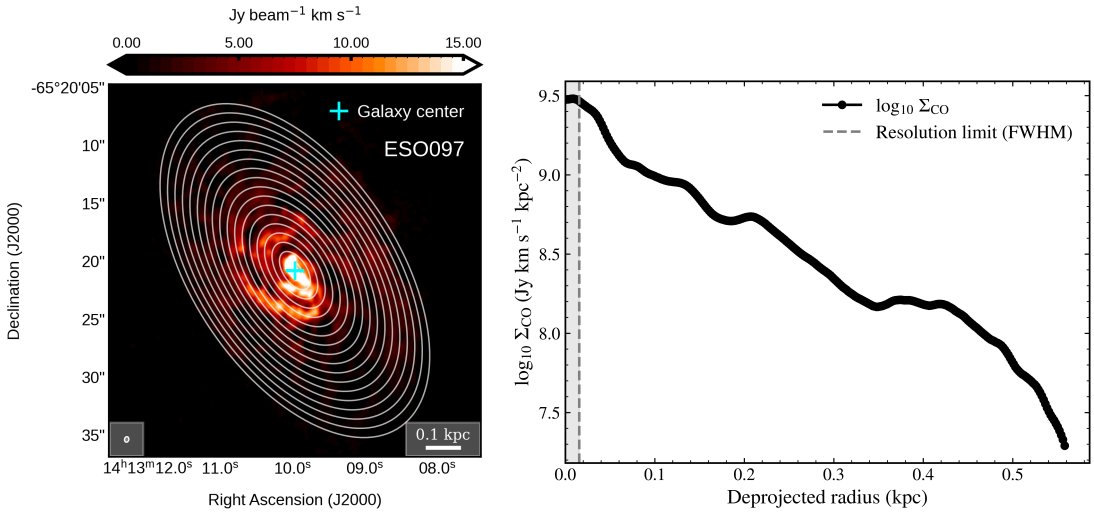


Figure 4.4: Radial profiles for the Circinus galaxy. *Left panel*: Annuli used for the radial profile in the zeroth moment, fixed at the center of the AGN. The cyan cross indicates the AGN position, while the white annuli represent the distribution and extent of the rings that measure $\Sigma_{CO(2\text{-}1)}$. Synthesized beam is found in the bottom-left corner, the scale is located at the bottom-right corner. *Right panel*: Radial surface brightness distribution across the galaxy in logarithmic scale, where each black point marks the surface brightness measure of one ring. The gray area represents the beam major axis threshold. Regions smaller than this area are unresolved.

is not captured as the image is too noisy. Something similar happens with the eastern feature seen in NGC 985, which is enclosed in the outer rings, that does not show in the radial profile. This is because these features are too small and faint, and its signal is being averaged with noise across the rest of the ring circumference.

4.4 Spatial correlations of molecular gas emission radio continuum contours.

Figure 4.5 shows the correlation between our ALMA CO(2−1) emission and VLA radio continuum emission at 22 GHz (Ilha et al., 2025; Kader et al., 2026) with 1”, 2”, 3” and 6” apertures, respectively for NGC 4941. Figs. 10.1-10.6 show the rest of the sample.

For our 5-galaxy VLA sample, all AGN centers are coincident with the radio continuum emission, where in 3 of 5 galaxies this is also the brightest spot in CO(2 − 1) emission (Mrk 926, NGC 4941 and NGC 5995), in the other two, HE 0412-0803 and NGC 985, the brightest cold molecular gas emission is not exactly correlated to the central radio continuum emission.

HE 0412-0803 shows a compact radio knot to the south-west of the nucleus, spatially correlated to one of the brightest spots in the merger. Another feature north-west of the nucleus shows another blob directed towards a bright molecular gas emission spot. In the 3” aperture observation, this latter feature is extended towards the same direction, covering the bright spot mentioned.

1” aperture emission in Mrk 926 shows centered radio emission, with spots towards the north-east of the nucleus which later become part of the large scale radio emission in the 3” observation.

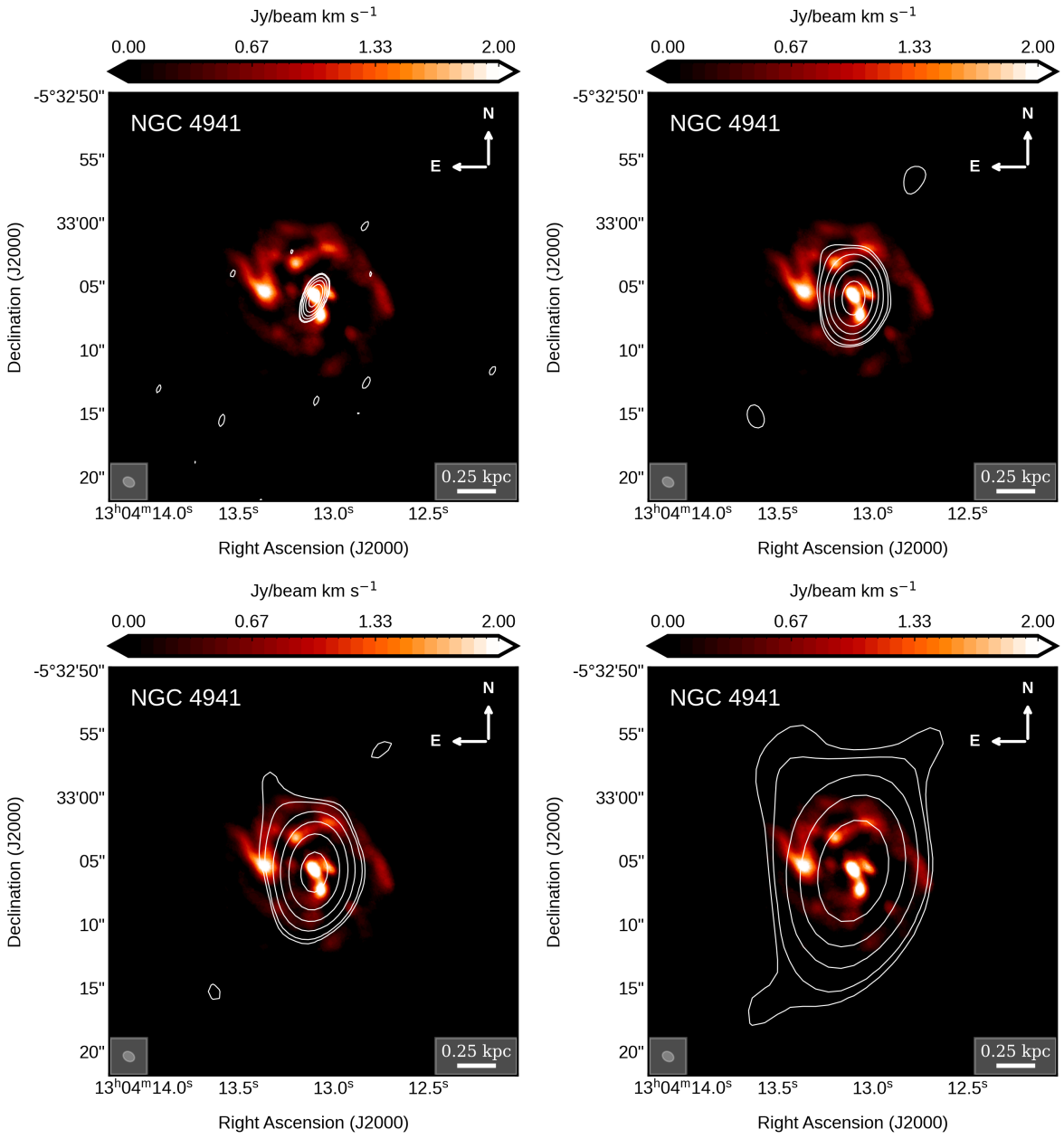


Figure 4.5: ALMA CO$(2-1)$ integrated intensity map (color) with 22 GHz VLA C configuration radio continuum contours (white) of NGC 4941. Contours were drawn at 3σ, 4σ, 8σ, 16σ, 32σ, 64σ, 128σ and 256σ. *Top-left panel*: 1" aperture VLA observation. *Top-right panel*: 2" aperture VLA observation. *Bottom-left panel*: 3" aperture VLA observation. *Bottom-right panel*: 6" aperture VLA observation. Synthesized beam is found in the bottom-left corner, the scale is located at the bottom-right corner and the arrows on the top-right corner indicate North and East.

The molecular gas emission towards the north-east, close to the nucleus (~ 0.5 kpc) seems to be co-spatial with the radio continuum emission. The 3" aperture observation suggests a double-sided radio emission, where in the 6" aperture emission data shows that the most prominent lobe is the one spatially correlated to the north-east CO$(2-1)$ emission. Observations with the B Array were also made, where a small double-lobed structure is seen in the 0.3" image. This is not correlated to the molecular gas emission, nor is the 1" B Array observation, except for the north-eastern component. A larger VLA radio continuum map was imaged over a larger field of view to capture faint radio emission. In this image we can see an X-shaped morphology, with one of the "arms" being co-spatial with the molecular gas emission from the north-eastern region close to the nucleus, the rest of the radio emission does not seem to have any co-spatial relation with the cold molecular gas content.

An interesting feature is present in VLA maps for NGC 985, where all aperture observations (1", 3" and 6") are co-spatial with the south-western emission components of the merger. This can be seen specially in 1" aperture imaging, where a lobe extends from the central regions towards the mentioned feature, closely coinciding with the spatial extent of the molecular gas. On a larger scale, the radio emission is primarily one-sided, as it extends towards the west of the galaxy, with a small "pointy" feature to the east.

As seen in Fig. 4.5, the 2" aperture image shows the radio continuum emission is co-spatial with a small bright CO$(2-1)$ emitting region to the north-east of the galactic center, as well as in the 3" aperture image, which also enclosures a similar molecular gas feature to the north-west of the nucleus. The radio emission in general seems to be co-spatial with that from the cold molecular gas, with the exception of the lobes shown in the 6" aperture image, where no molecular gas extends to the distance of the lobes (~ 1 kpc).

Finally, in NGC 5995, radio emission is co-spatial in all apertures with a feature separated ~ 2 kpc from the center to the west. The best correlation is found in the 2" and 3" images, where the radio lobe extends primarily to the west, exactly where the molecular gas feature is located.

4.5 3D Kinematics Modeling

As mentioned in Sect.3.2.1, we explore the kinematics and non-circular motions of selected galaxies with the ^{3D}BBarolo modeling tool. The best fits for each target are shown in Figs. 11.1-11.17, as well as position-velocity (PV) diagrams, channel maps, and best-fit parameters.

Circinus Galaxy : For this fit, `NRADII = 40` and `RADSEP = 0.471853`, the latter being the value of BMAJ (major axis of the beam). The mask used corresponds to a `THRESHOLD` mask of value 0.035, which means that all pixels with flux below this threshold are blanked (NaN data points). The central position was fixed at the AGN location, namely `XPOS = 263.92` and `YPOS = 265.92` in pixels. We find that the best value for the PA is 205°, and for this fit it is fixed. The inclination was estimated to be 57°, in agreement with the value found with isophote analysis, therefore, this is the value we use as our initial value for the fit.

The best-fitting model and parameters are shown in Figs. 4.6 and 4.8. Inclination values show variance between 55° and 62.5°, higher inclinations characterizing the outer regions of the galaxy. In the moment maps, we can see how the model adjusted to the data. The residuals will show non-rotational motions, morphological differences, and rotational pattern differences. Using the

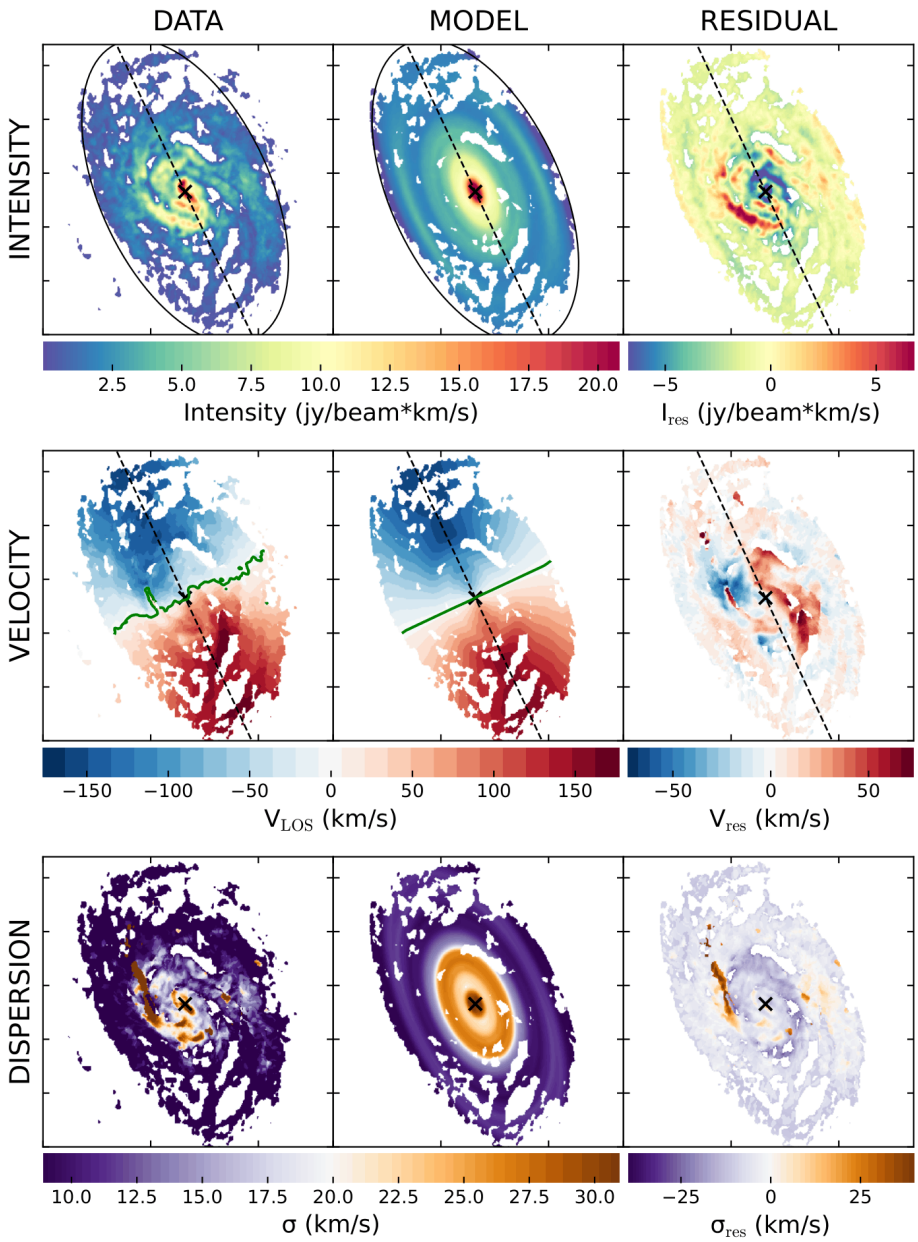


Figure 4.6: ALMA CO$(2-1)$ kinematics model by ^{3D}BBarolo for the Circinus galaxy. *Left row (Data)*: Observed integrated intensity (Moment 0, top), intensity-weighted velocity field from the line of sight (Moment 1, middle) and velocity dispersion (Moment 2, bottom). *Middle Row (Model)*: Corresponding moment maps reconstructed from the best fitted tilted-ring model. *Right Row (Residuals)*: Residual maps showing the differences between the data and the model. The last ring modeled is shown as a solid black ring on moment 0 plots, with the dotted black line being the major axis of the outer ring.

`AZIMUTHAL` normalization instead of the `LOCAL` one allows us to interpret interesting features in the moment 0 maps. Comparing the data with the ^{3D}BBarolo models, we can see that Circinus appears to have an inner disk with different rotational patterns from the general, more extended

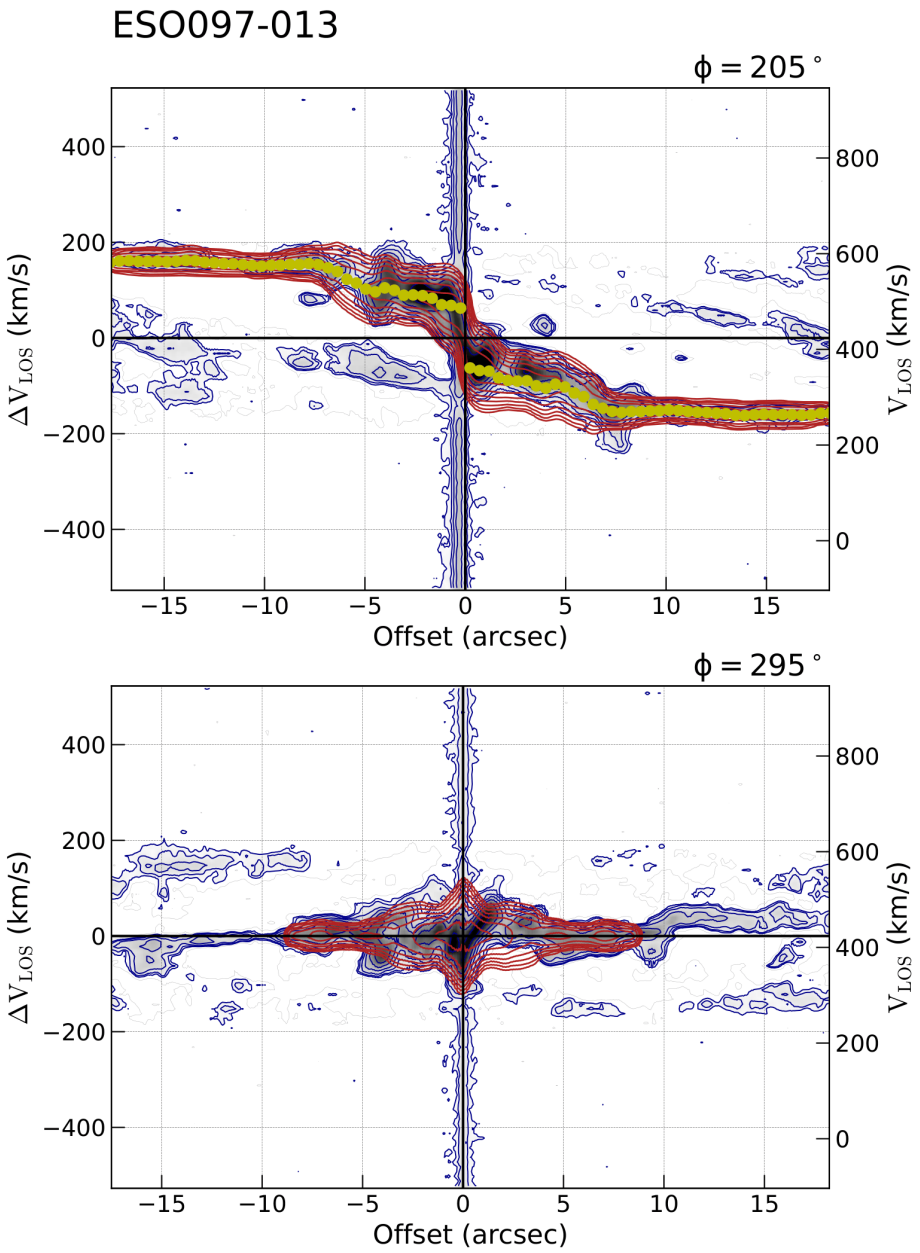


Figure 4.7: ALMA CO$(2-1)$ position-velocity (PV) diagram and PV model by ^{3D}BBarolo for the Circinus galaxy. The grayscale intensity background represents the observed data, where overlaid blue contours indicate positive line emission, whereas gray contours indicate negative noise levels. The ^{3D}BBarolo model is overlaid as red contours ($1\sigma, 2\sigma, 4\sigma, 8\sigma, 16\sigma, 32\sigma$ and 64σ) evaluated at the same flux levels as the data. The solid black line marks the spatial center and systemic velocity $V_{\rm sys}$ (corresponding to $\Delta V_{\rm LOS} = 0$ km s^{-1}). ϕ indicates the best-fit for the position angle (PA) of the kinematic axis in degrees. *Top panel*: Major axis PV diagram. Yellow dots indicate the ^{3D}BBarolo best-fit rotational velocity points projected at each ring. *Bottom panel*: Minor axis PV diagram.

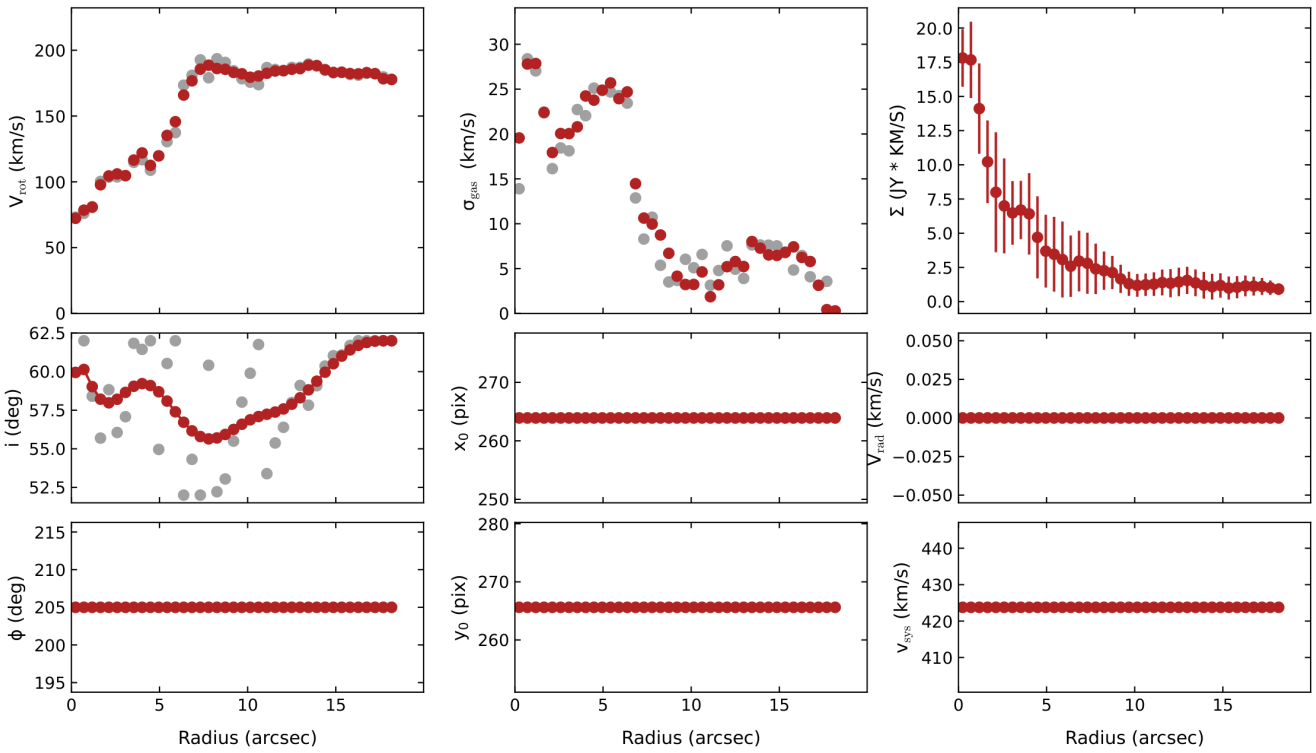


Figure 4.8: Best fitted parameters by ^{3D}BBarolo for the Circinus galaxy. Gray points represent the observed data, whereas red points represent the ^{3D}BBarolo fit. Each point corresponds to a ring in the fit. *Top-left panel*: Rotational velocity in km s^{-1}. *Top-middle panel*: Velocity dispersion in km s^{-1}. *Top-right panel*: Modeled CO$(2-1)$ brightness in Jy km s^{-1}. *Middle-left panel*: Inclination of each fitted ring in degrees. *Middle panel*: Central position of the AGN in the x axis in pixels. *Middle-right panel*: Radial velocity in km s^{-1}. This value is always fixed at zero. *Bottom-left panel*: Position Angle inclination (PA) in degrees. *Bottom-middle panel*: Central position of the AGN in the y axis in pixels. *Bottom-right panel*: Systemic velocity, automatically estimated by ^{3D}BBarolo.

rotation of the molecular gas. The residuals in both moment 1 and 2 suggest that this galaxy possesses an inner disk that rotates at a different PA than the rest of the galaxy. This could be an explanation for the swings in inclination values in the middle region of the galaxy compared to the outer region. The "stream-like" feature mentioned in Sect.4.2 is well detected in the residuals of the moment 2 maps, and seen fainter in moment 1 residuals. Compared to our model, that feature alone is about 30 km s^{-1} faster than the predicted velocity dispersion by the model. This argument is supported by the residuals in moment 1 maps, where this feature is seen as a red tail piercing into blueshifted motions, as seen also in 4.3. There are also smaller spots seen in the moment 2 residuals, which show velocity dispersion speeds of about 60 km s^{-1}.

Position-velocity diagrams (Fig. 4.7) map the spatial position of celestial objects against their Doppler-shifted velocity. For Circinus, it shows line-of-sight speeds of $\sim \pm 200$ km s^{-1}, derived from the major axis PV diagram. In the minor axis PV diagram, small regions suggest velocity dispersions of ~ 100 km s^{-1}.

IC 1657 : In this fit, `NRADII = 25` and `RADSEP = 0.642214`, with a `THRESHOLD` mask of value 0.003. The central position was fixed at the AGN location, this being `XPOS = 275.54` and `YPOS = 262.41` in pixels. We find that the best value for the PA is 175°, and for this fit it is fixed. The inclination was estimated to be 79°, in agreement with the value found with isophote analysis, therefore, this is the value we use as our initial value for the fit.

The best-fitting model and parameters are shown in Figs. 11.1 and 11.3. Inclination estimations yield a fixed value of 83°, in agreement with the inclinations estimated with isophotes. The residuals in moment 1 suggest a different rotational pattern, as if the kinematic PA was offset from the morphological PA of the galaxy. This phenomenon can be easily explained by the fact that this galaxy is nearly edge-on, and therefore what is seen in the residuals are the spiral arms of the galaxy. Rotational velocities are $\sim$ 200 km s^{-1}, with high residuals of $\sim$ 50 km s^{-1}. In the moment 2 maps we can see some residuals that have $\sim$ 20 km s^{-1} more velocity dispersion than the model predicted. These residuals can be seen across the entire galaxy center.

Now, from the PV diagrams (PVDs) we can see coherent rotational motions all across the galaxy, with some very faint emission not being modeled at Offset = 10 (see Fig. 11.2). The PVDs agree with rotational speeds of $\sim$ 200 km s^{-1} (major axis PVD) while velocity dispersions reach more than 100 km s^{-1} (minor axis PVD). In the minor axis PVD, there is faint emission that the model cannot capture, at both sides of the offset around $\pm$3.

IC 5063 : Here we fit only the central region of the merger, due to its complicated morphology. We used `NRADII = 7` with `RADSEP = 0.483193`, using a `THRESHOLD` mask at 0.004 flux. The same procedure is followed, fixing the center of the AGN at coordinates `XPOS = 267.54` and `YPOS = 271.37` in pixels. We find that the best value for the PA is 110°, fixing it for the fit. The estimated inclination is 70°, about 5 degrees off of our initial estimate. We use this value for our inclination estimations.

The best-fitting model and parameters are shown in Figs. 11.4 and 11.6. Immediately from the moment 0 map we see a massive 10 Jy beam^{-1} km s^{-1} residual from the western component. This shows that CO(2$-$1) emission here is extremely bright. A similar case occurs with the feature next to the AGN center, where a bright residual appears as well. These two bright spots are also seen in moment 2 residual maps. Here the residual shows a massive $\sim$ 500 km s^{-1} difference between the model and data, suggesting high velocity dispersions in these features. Moment 1 residuals showcase the complex rotational patterns the galaxy follows. The zero-velocity component appears to be slightly off from the AGN center, causing the residuals to be more blueshifted.

PVDs (Fig. 11.5) show extreme motions, starting with the western component showing up to $>$ 200 km s^{-1} rotational speeds, whereas the eastern side of the galaxy rotates at $\sim$ 200 km s^{-1}, showing a discrepancy between rotation speeds, suggesting asymmetric motions. The two vertical lines at Offset = -0.5 and 1.5 could be the same construct mentioned for the Circinus galaxy. However, in this case, the component is significantly broader, with well-defined contours showing signs of emission. On the minor axis PVD, we see faint emission showing velocity dispersions of $\sim \pm$200 km s^{-1}.

NGC 1566 : For this target, `NRADII = 16` with `RADSEP = 0.856477`, with a `THRESHOLD` mask at 0.008 flux. We fix the AGN center at `XPOS = 269.3` and `YPOS = 270` pixels. We find that the best value for the PA is 240°, and for this fit it is a free parameter to obtain a better fit of the zero-velocity line. The inclination was estimated to be 32°, about 10 degrees from that obtained from

isophote analysis. However, this inclination is obtained from the kinematic PA inclination, which is different from the morphological PA. We use both inclination and PA values as first estimations for the algorithm.

The best-fitting model and parameters are shown in Figs. 11.7 and 11.9. Both the inclination and PA show changes across the galaxy. Towards extended regions of the galaxy, both inclination and PA seem to increase, with the inclination fluctuating between $\sim 30°$ and $\sim 35°$, which is consistent enough given that errors of $\pm 5°$ are withing acceptable boundaries. The PA variations can be seen in the zero-velocity region, exhibiting an S-shape across. In the moment 0 residuals we can see a nuclear bar in red, with an arm feature west of the nucleus. Velocity dispersion residuals show higher values are co-spatial with higher residual values from the moment 0 map. The blue spots on the moment 0 residuals appear to be co-spatial with high velocity dispersion residuals in the center of the galaxy. Moment 1 maps display non-rotational features to the north side of the nucleus, as well as a north-western component that forms part of the spiral arm. High velocity residuals are found in the latter feature, as well as to the south-east of the nucleus, showing that residuals are present even at considerable distances from the central, high velocity dispersion regions.

The PVDs (Fig. 11.8) show coherent rotational motions, with the model correctly representing the data at all point of the major axis PVD, with velocities reaching ± 200 km s^{-1}. The same vertical lines that Circinus PVDs displayed are seen here as well. An interesting feature is seen at Offset = 6 on the minor axis PVD. A clump is seen that is not fitted by the model, showing dispersion speeds of ~ 30 km s^{-1}. Velocity dispersions show values below 100 km s^{-1}.

NGC 4941 : For the fit, we adopted `NRADII = 8` with `RADSEP = 0.944707` with a `THRESHOLD` mask at 0.005 flux. The central position of the AGN is fixed at `XPOS = 270.43` and `YPOS = 270.02` pixels. We find that the best value for the PA is 230°, and for this fit it is a free parameter due to the complexity of the zero-velocity line. The inclination was estimated to be 41°, in agreement with that obtained from isophote analysis. We use both inclination and PA values as first estimations for the algorithm.

The best-fitting model and parameters are shown in Figs. 11.10 and 11.12. A stable value for the inclination was found, this being 45°, while the PA decreased dramatically from $\sim 260°$ to $\lesssim 200°$. This is seen as the same S-shape we mentioned earlier, that matches the rotation curve of the data neatly. In moment 0 residuals we can see bright emission components in the spiral arms, showing concentrations of cold molecular gas. In the moment 1 residuals we see a redshifted feature to the west of the nucleus, possibly a non-rotation motion, as well as a very prominent blueshifted residual to the north-western side of the nucleus. The possible non-rotating motion spot found is co-spatial with the most prominent velocity dispersion residual.

PVDs (Fig. 11.11) show that the model was not able to fit certain features. In the major axis PVD, we can distinguish two important structures, that being the center and a spiral arm. The central region shows speeds up to ~ -100 km s^{-1} and ~ 70 km s^{-1}, rotating faster on one side than the other. This could be due to the westen feature close to the nucleus that popped up in the moment 1 and 2 residuals. The possible spiral arm feature at Offset = -5 shows speeds up to 200 km s^{-1}. In the minor axis PVD we can see the model does not fit the contents correctly, as a large mass of molecular gas from Offset = -5 to Offset = -1 sits above the fit, reaching velocity dispersions of ~ 80 km s^{-1}. In the central regions something similar happens compared to the major axis PVD, where the central emission reaches higher velocity dispersion values than the

model shows. Some part of this could come from the high velocity dispersion feature seen in moment 2 residuals. This central feature reaches up to ± 150 km s^{-1}.

NGC 5643 : Similar to the proceedings for IC 5063, on this galaxy we only focus on fitting the central region as its morphology is complicated enough such that the `AZIMUTHAL` normalization is unable to produce good fits. We set `NRADII = 11`, with `RADSEP = 0.505241` and a `THRESHOLD` mask at 0.008 flux. The center of the AGN is fixed at `XPOS = 282.08` and `YPOS = 280.910` pixels. We find an inclination of 30°, which is 30 degrees off from that estimated with isophotes due to the region of study being central, not portraying the full morphology of the galaxy. The PA was estimated at 320°. Due to the complex geometry of the zero-velocity line of the galaxy, both parameters are left free. We use the reported values as initial parameters for the algorithm.

The best-fitting model and parameters are shown in Figs. 11.13 and 11.15. A fixed value for the inclination was found at $\sim 35°$, while the PA varies between $\sim 300°$ and $\sim 355°$, as expected. Moment 0 residuals reveal the already mentioned nuclear bars (Sect.4.2), with residuals in the order of 3 Jy/beam km s^{-1}. Residuals from moment 1 maps show a bid redshifted residual north of the AGN position, as well as small features south-west of the nucleus. The residuals reach more than 50 km s^{-1}, which is almost the same magnitude as the nuclear rotation velocity seen in the data panel. Moment 2 residuals show clear high velocity dispersion features north and south of the nucleus.

Major axis PVDs (Fig.11.14) shows a good correlation between the model and the data. However, fast components are seen in the vertical, suggesting rotational motions in the central regions reaching more than ± 200 km s^{-1} velocities. Similarly, in the minor axis PVD this same feature is seen, displaying velocity dispersions that reach up to ± 250 km s^{-1}. Some blobs are also seen, at Offset = -3, 3 and 4. The model seems to neatly represent the data, though a noticeable discrepancy is seen between Offset = 2-4. They could be indicators of non-circular motions, since the model is not entirely co-spatial with this feature.

NGC 5995 : In this fit, we had to leave out the feature seen at ~ 2 kpc west of the nucleus, as it would have required a bigger ring that would enclosure too much noise. This is motivated by the procedures done in IC 5063 and NGC 5643, where the fit was performed only to central regions. In this fit we use `NRADII = 12` with separation of `RADSEP = 0.488532` and a `THRESHOLD` mask of 0.0075 flux. The center was fixed at `XPOS = 273.07` and `YPOS = 269.87` pixels. We estimated inclination values at 65°, in agreement with that found in the isophote analysis, which we adopt as our initial parameter. The PA was estimated at 320°, and it is kept fixed for this fit.

The best-fitting model and parameters are shown in Figs. 11.16 and 11.18. A stable value for the inclination was found to be 70°. Moment 0 maps show a common feature in this sample, which appear to be nuclear bars, where residuals show vast amounts of cold molecular gas in these features ($\sim$ 2.5 Jy/beam km s^{-1}). This bright residual bar component is co-spatial with high velocity dispersion residuals, where in the latter the distribution is clearer. Moment 1 residuals note 2 distinguishable features, one is the blueshifted residual located south-east of the nucleus, and what appears to be a sign of non-circular motions close to the AGN.

The major axis PVD (Fig. 11.17) shows a coherent rotation curve, which the model neatly represents. There are a couple of features worth noting. The first is the faint emission seen at Offset = -2, which seems to rotate slower than the rest of the molecular mass. The other feature

is the slightly vertical component at Offset = 0 that reaches $\sim$ 300 km s^{-1}, rotating faster than than the maximum disk rotation speed of $\sim$ 200 km s^{-1}. On the minor axis PVD, we see that the model does not fit the data as well as seen before. Velocity dispersions reach $\sim$ 350 km s^{-1}, and appear to be highly asymmetric in a V-shaped contour, oriented upside down. This could be another signal of non-circular motions.

Chapter 5

Discussion

In this study, we have presented the cold molecular gas properties of X-ray selected AGN with ionized outflow signatures, using the CO(2 − 1) rotational transition as tracer. In this section, we discuss the implications of the results presented in Chapter 4 and explore the possibility of molecular gas outflows in our AGN sample.

We find cold molecular gas in ∼ 89% of our sample, reporting CO(2 − 1) line luminosities ranging between 1.2×10^7 and 1.5×10^9 K km s^{-1} pc^2, in agreement with recent low-redshift CO(2 − 1) AGN studies (e.g. Saintonge et al., 2017; Rosario et al., 2018). The estimation of the total molecular gas mass $M_{\rm H_2}$ yields values ranging from 1.2×10^7 $M_\odot$ and 8.2×10^9 $M_\odot$, similar to those found in Saintonge et al. (2017). We followed a standard H_2-to-CO luminosity ratio $r_{21} = 0.79$ (Saintonge et al., 2017) for the estimations, using conversion factors of $\alpha_{\rm CO} = 0.8$ as a lower mass limit, and $\alpha_{\rm CO} = 4.3$ as the upper limit.

To investigate potential outflowing motions, line widths FWHM$_{\rm CO}$ were estimated through CO(2 − 1) emission line multi-component Gaussian fits, ranging from 90 − 480 km s^{-1}. A common procedure in determining outflowing motions is the detection of broad wings in emission lines, where FWHM $\gtrsim$ 800 km s^{-1} (e.g. Feruglio et al., 2010), however, in our AGN sample we do not detect classic broad emission-line wings. One could make an argument for Mrk 463 and IC 1657, but the emission line is likely to show these extra components on each side due to redshifted components instead of high-speed outflowing gas. Our FWHM do not meet the criteria by themselves to categorize outflowing motions in our targets, as all FWHMs are below 500 km s^{-1}. The targets with the broadest emission lines (FWHM$_{\rm CO}$ ¿ 300 km s^{-1}) in our sample are IC 1657, HE 0224-2834, Mrk 463, Circinus, NGC 5995, 3C 403, IC 5063 and Mrk 926. Of these targets, IC 5063, Circinus, NGC 5643 and Mrk 463 have studied CO outflows/inflows (Morganti et al., 2015; Zschaechner et al., 2016; García-Bernete, I. et al., 2021; Treister et al., 2018).

Molecular gas distributions are concentrated mainly in the central regions of the galaxies, decaying exponentially with the radius. In the logarithmic scale, this is seen as a linear decrease, where in some targets increments are seen due to features such as spiral arms or ring-like structures (e.g. 3C 403 and HE 0224-2834). As mentioned above, both targets show FWHM$_{\rm CO}$ ¿ 300 km s^{-1}, so the rings could be an indicator of displaced cold molecular gas from the central regions of the galaxy due to AGN feedback. This is discussed in depth in the following.

In targets with available VLA observations, direct spatial correlations between CO(2 − 1) emission and radio continuum emission are seen. From our molecular outflow candidates, this can be seen for Mrk 926 and NGC 5995, where extended radio emission appears to be correlated to

extended molecular gas features in these sources. For Mrk 926, this extended emission seen in the 3" aperture is not due to a relativistic jet, as this galaxy is radio quiet, but rather by self-absorbed synchrotron emission (Mundell et al., 2000) or AGN winds/outflows. In NGC 5995, extended radio emission is seen in the 2" and 3" apertures, however, this is also a radio-quiet AGN and therefore rather than a jet, this could also be a result of AGN activity, such as an outflow. For both targets, an explanation to the compact radio emission could be shock-generated synchrotron emission, where free electrons are accelerated at the shock front by first-order Fermi acceleration, creating co-located synchrotron radio emission with the multi-phase outflowing gas.

In other sources such as HE 0412-0803 and NGC 985, extended radio emission is seen, related to jet activity and star-forming activity, respectively (Doi & Inoue, 2016; Weaver et al., 2026). The extended radio component in HE 0412-0803 is not co-spatial with our cold molecular gas emission, therefore not related to a possible outflow of CO$(2-1)$ molecular gas. This is further evidence that this target does not possess a molecular outflow of cold molecular gas, as $\mathrm{FWHM_{CO}} = 117$ km s^{-1}.

5.1 Molecular Gas Rings in 3C 403 and HE 0224-2834

We focus on the molecular gas rings found in 3C 403 and HE 0224-2834, as these structures could be signs of displaced cold molecular gas. In 3C 403, an interesting feature is seen, as the zero velocity is not centered on the AGN, but rather this structure seems blueshifted at the galaxy center, with high speeds (~ 150 km s^{-1}) towards the south-west and north-eastern regions. The rotation seems to be coherent with no signs of merger activity. This can also be seen in the velocity dispersion map, where higher dispersions come from the central region only, showing < 20 km s^{-1} speeds. There is a small, unresolved spot in the south-west region, but this feature alone is not enough evidence to show this ring-like structure was caused by high-speed outflows or jet activity. The possible reorientation of the jet seen in 3C 403 has been discussed in a number of studies (e.g. Dennett-Thorpe et al., 2002; Tarchi, A. et al., 2007), as VLA data show an X-shape, common feature in jet reorientation targets. The "younger" jet is oriented roughly NE-SW, the more extended, weaker one in the SE-NW direction. This reorientation is not due to recent merger activity in the host galaxy, as this kind of activity is ruled out in the last $\sim 10^8$ years (Dennett-Thorpe et al., 2002; Landt et al., 2010). The most plausible explanation for realignment is a binary black hole system in the source (Dennett-Thorpe et al., 2002; Tarchi, A. et al., 2007). The weaker jet is not spatially correlated to our CO$(2-1)$ emission, so it supports the argument that it is unlikely that AGN jet feedback is responsible for the ring-shaped morphology seen in 3C 403. We can also rule out spiral arms or bars forming this ring, since 3C 403 is an elliptical galaxy. One plausible explanation for this feature could be radiative feedback. The AGN emits X-rays and possesses strong narrow-line emission, with a radiative disk (Dennett-Thorpe et al., 2002; Kakkad et al., 2022), so winds produced by instabilities on the accretion disk could shape the ring-like structure seen. As mentioned, recent merger activity is discarded for this source. However, if the galaxy merger occurred $\sim 10^8$ there would no longer be gaseous tracers of this activity (Begelman et al., 1980). Due to the low velocity dispersion of the ring, thus, it is possible that it was formed during a merger event before the jet realignment, showing no merger features now.

In the case of HE 0224-2834, it lacks a radio jet, being cataloged as a low-luminosity QSO. It is reported as a possible merger or merger remnant, with irregular morphology and unclear barred-

ness, with an extragalactic source within 340 kpc (König et al., 2009). The ring-like structure, like in 3C 403, may be due to accretion disk instabilities or merger activity. Although both rings could be explained by AGN-driven winds or outflows, we can reject the idea that the feedback is jet-driven. Further study to gas kinematics with 3D modeling could provide an enhanced view on the kinematics of the cold molecular gas phase for these targets, especially HE 0224-2834 since it shows a massive CO$(2-1)$ reservoir.

5.2 Notes on Individual Targets

In the following section, we present the results of the data analysis described above for the individual targets.

3C 33 : This is a Fanaroff-Riley type II (FRII) radio galaxy, cataloged as a high-excitation galaxy (HEG), with its radio emission showing two extended lobes and symmetric jets aligned with a large-scale structure that extends up to 120 kpc each (Leahy & Perley, 1991; Giovannini et al., 2005). This jet emission is not spatially correlated with the eastern CO$(2-1)$ feature ~ 3 kpc from the nucleus, however, it seems to be oriented in the same direction of [O III]$_{\lambda 5007}$, Hα and [S II]$_{\lambda 6717}$ emission (Couto et al., 2017). This region traces the ionized outflow reported byCouto et al. (2017), however, despite the ionized outflow being directed in the same direction of our feature, we do not find evidence for a molecular outflow in this galaxy due to its low velocity dispersions ~ 50 km s^{-1} and narrow line profiles FWHM$_{\rm CO} = 87$ km s^{-1}, meaning its most likely been depleted by the powerful jet. The ionized outflow is not likely driven by the radio jet, but by radiation released by accretion processes (Speranza et al., 2021).

NGC 424 : This target is cataloged as a heavily obscured Seyfert type II galaxy. A multi-wavelength study on the ionized outflow present in this galaxy was done by Marconcini, C. et al. (2025), where they find that the CO$(2-1)$ emission originates from ordered motions within the gaseous disk, with no evidence of molecular gas outflows from PVD and Gaussian fits. We come to the same conclusions in this study, where we find FWHM$_{\rm CO} = 197$ km s^{-1} and low velocity dispersions of ~ 70 km s^{-1}. Also, a difference between this study and Marconcini, C. et al. (2025) is that for the Gaussian fit we used a larger aperture, capturing emission from the arms to better characterize the molecular gas content, whereas they performed the Gaussian fit to the central region only.

IC 1657 : This galaxy is a barred spiral, highly obscured Seyfert type II, which is highly inclined at a reported 78°. There is sparse literature on this target, limiting direct observational comparisons. This galaxy has a bi-conical outflow structure perpendicular to the disk plane, which is understood to be driven by star formation winds (López-Cobá et al., 2020). In our sample, IC 1657 is one of the galaxies with broader lines, with FWHM$_{\rm CO} = 354$ km s^{-1}, with possible molecular outflow signatures. We analyze this possibility with $^{\rm 3D}$BBarolo tilted-ring modeling, finding a non-circular motion in the minor axis PV diagram. The non-circular motion is observed at Offset $= \pm 4$", which corresponds to ~ 700 pc. The typical amplitudes are ~ 100 km s^{-1}, showing a blueshifted and redshifted component. In the surface brightness radial profile, a small

bump can be seen at the same distance where the inflow is located, possibly showing a grouping of cold molecular gas due to non-circular motions. We cannot differentiate between an inflow and an outflow, because of the inclination of this galaxy, detecting the far and near side of the galaxy towards us is complicated. As mentioned, this target has a well understood bi-conical outflow perpendicular to the galactic plane (López-Cobá et al., 2020), so this would be the most plausible explanation to our non-circular motions seen in the cold molecular gas phase, suggesting a possible correlation with the ionized outflow.

HE 0224-2834 : As discussed earlier, this galaxy is cataloged as as a low-luminosity QSO. It is reported to be a possible merger with irregular morphology and unclear barredness, with an extragalactic source within 340 kpc (König et al., 2009). A ring-like structure can be seen ~ 2.5 kpc west of the AGN, possibly attributed to merger activity. The latter could explain the asymmetrical ring, as in this galaxy the atomic gas is much more extended than the molecular gas, showing distortions in the disk with optical DSS images revealing morphological signs of interaction with a close companion (König et al., 2009). Apart from the relatively high $CO(2-1)$ line width of $FWHM_{CO} = 334$ km s^{-1}, no cold molecular gas outflows are detected. However, emission line widths are similar to those of IC 1657, which was determined to possess an inflow in the central regions of the galaxy, and therefore a thorough kinematic analysis should determine whether non-circular motions are present in this source.

NGC 985 : This source is reported to be a luminous Seyfert type I galaxy, which showed prominent signatures of high frequency excess in the radio continuum spectra and is understood to be undergoing a merger process. This galaxy also contains a double nucleus, the Seyfert type I and a non-AGN separated by ~ 2.5 kpc (Doi & Inoue, 2016). Obscuration of the AGN is due to winds associated to the accretion disk. For this target, no molecular outflow signs are seen, with $FWHM_{CO} = 215$ km s^{-1} and low velocity dispersions (~ 50 km s^{-1}).

HE 0351+0240 : This galaxy is an ongoing merger system, with an unobscured QSO. In recent cold molecular gas studies, there is no evidence for star formation as no $CO(1-0)$ is detected, as the gas in the two interacting galaxies was likely redistributed due to their tidal interactions (Powell et al., 2018). The same argument could be made for our case, as this target does not present any $CO(2-1)$, making this target severely molecular gas deficient.

HE 0412-0803 : This target is cataloged as a Seyfert type I galaxy, with bulgy morphology and non-interacting (Husemann et al., 2022). This galaxy was studied in $CO(1-0)$ and $CO(2-1)$, however, no detection was achieved in either transition according to Bertram et al. (2007). We do find cold molecular gas reservoirs in this target, with $M_{H_2} = 1.2 \times 10^8 - 6.5 \times 10^8$ $M_\odot$. Also, VLA observations on this target show collimated radio continuum emission spatially correlated to our $CO(2-1)$ data, but there is no evidence for cold molecular gas outflows, as the $CO(2-1)$ emission line width is among the narrowest in our sample ($FWHM_{CO} = 117$ km s^{-1}).

NGC 1566 : This source is a low-luminosity AGN, classified as a Seyfert, though its position between Seyfert types I and II varies in the literature. In the radial profiles of gas distribution we find an increase in surface brightness at ~ 1 kpc due to spiral arms seen in the $CO(2-1)$. This

structure is directly correlated to the double-peaked Gaussian profile seen, with $\mathrm{FWHM_{CO}} = 234$ km s^{-1}. The central regions of NGC 1566 have been thoroughly studied in the cold and warm molecular gas phases (Combes et al., 2014; Slater et al., 2019), finding cold molecular masses of $1.1 \times 10^8 M_\odot$ in the inner ~ 1.28 kpc. In our study, we find $1.33 \times 10^8 M_\odot$ in the 4-5 kpc central emission with $\alpha_{\mathrm{CO}} = 0.8$, and $7.16 \times 10^8 M_\odot$ for $\alpha_{\mathrm{CO}} = 4.3$. The discrepancy in values comes from different fields of view in observations.

The central regions have been well studied for the presence of non-circular motions in these regions (Slater et al., 2019). In our major axis PVD we can see that in Offset = ±3" rotational speeds are higher than in Offset > ±5", reaching velocities of ~ 180 km s^{-1}. This is a sign that gas is rotating faster in the inner ~ 300 pc of the galaxy. In the minor axis PVD, we can see that the far side (left side in PVD) shows inflow signatures in the inner regions of the galaxy disk (~ 7 arcsec; ~ 750 pc) and spiral arms (~ -10" to ~ -15"; $\sim 1-1.5$ kpc) with speeds of ~ 50 km s^{-1}, as well as inflowing motions in the near side (right side in PVD) seen at ~ 6" or ~ 600 pc with similar speeds. This flow inward has been well documented, with nuclear bars transporting the material into the innermost regions and towards the SMBH. This particular feature can be seen in moment 0 residuals, showing one bar east of the AGN and one roughly west.

Outflowing motions can also be seen in the innermost regions at $\sim \pm 1$ arcsec or ~ 100 pc with characteristic speeds of ~ 90 km s^{-1}, almost half of the outflow velocity found in Slater et al. (2019). In the moment 1 residuals the non-circular motions are present in the inner disk, as well as the spiral arm roughly south-west of the nucleus which showed inflow signatures.

NGC 4941 : This source is classified as a Seyfert type II galaxy with a morphological class of Sa (unbarred spiral galaxy). It shows strong evidence for a bar-like structure in CO, which is not apparent in the stellar light distribution (Stuber et al., 2023). We find a multiple arm structure that can be seen as a triple-peaked Gaussian profile, and also reflected in a surface brightness increase where the arms are located (~ 0.2 kpc). They report a molecular gas mass M_{H_2} of $5.13 \times 10^8 M_\odot$, which is several times more than that found for our targets. There is no literature on molecular outflows in this galaxy, but in our study we find evidence for this. In recent studies, only tentative evidence for a $50-100$ km s^{-1} molecular outflow (García-Burillo et al., 2021), while a compact outflow has been associated to a radio jet in the north-west direction, while a small outflow counterpart could also be possible, not seen in the radio map (Barbosa et al., 2009). In Sect. 3.1.4 we discussed the mentioned NW radio continuum feature in the 6" aperture image, where an extension can also be seen towards the south-east region.

By analyzing residuals and PV diagrams, we can characterize the presence of a molecular outflow if there is one. In the minor axis PVD, the near side of the galaxy is towards the east and the far side towards the west. The south-east (left side) region shows a redshifted component to about ~ 80 km s^{-1}, $\sim 80-400$ pc from the AGN, as well as in the north-west direction (right side), reaching ~ 100 km s^{-1} at $\sim 250-400$ pc from the AGN, meaning gas is inflowing from the spiral arms and nuclear regions towards the AGN. There are also signs of outflowing motions that reach ~ 150 km s^{-1} in the innermost regions (~ 170 pc), which point in the same direction of the radio jet mentioned earlier and seen in our VLA maps. There are also signs of inflowing motions in the nuclear regions of the NW direction of the minor axis PVD (~ 2"; ~ 170 pc), which could be the cause for the high-velocity dispersion feature seen in moment 2 residual maps, west of the AGN center. Seeing outflowing/inflowing motions in the same region of the disk, but at different scales, could suggest that the inflowing material from possible nuclear arms is fueling the outflow

seen in the central regions of the galactic disk.

In the major axis PV diagram, we see a high-velocity component that does not follow the rotation of the galaxy at ~ 4" or ~ 340 pc. This could be a faster-spinning spiral arm, seen in the moment 1 maps as the most redshifted component.

Mrk 463 : This galaxy has been classified as an ongoing merger with dual AGN, based on *Chandra* X-ray observations. The two nuclei, Mrk 463E (east) and Mrk 463W (west) are separated by ~ 3.8 kpc and have heavily obscured AGNs. It is understood that the AGN in Mrk 463E is energetically more important to the system than the one in Mrk 463W. An interesting feature is that almost no CO$(2-1)$ emission overlaps with the AGN location on our maps, which is also seen in Treister et al. (2018). We obtain molecular gas masses of $\sim 8.24 \times 10^9$ using $\alpha_{\rm CO} = 4.3$, similar to that found in Treister et al. (2018), although they calculate it for the emission surrounding Mrk 463E and Mrk 463W, obtaining $1.36 \times 10^9 M_\odot$ and $5.39 \times 10^8 M_\odot$, respectively. We report smaller velocity gradients than those in (Treister et al., 2018), ranging from ~ 420 km s^{-1} in the eastern nucleus to ~ 150 km s^{-1} in the western nucleus. It is also reported that despite displaying a bi-conical ionized outflow, molecular outflows are not detected, but rather inflowing motions that feed the SMBH. This can be seen in moment 1 and 2 maps, where the high velocity dispersion (~ 180 km s^{-1}) spot in the position of Mrk 463E is co-spatial with the high velocity gradients mentioned above, as well as the emission line profiles that show the broadest components seen in our sample, at FWHM$_{\rm CO} \sim 480$ km s^{-1}.

Circinus : Circinus is a Seyfert type II galaxy and is also the closest AGN to us, so this target has been thoroughly studied over the years. We find substantial amounts of cold molecular gas in the ~ 1 kpc of the galaxy, documented as a starburst region, and a dip in surface brightness in the edges (Curran et al., 2008). This source has shown signs of a multiphase outflow in the inner regions of the galaxy driven by the AGN, oriented in the NW-SE direction (Zschaechner et al., 2016). We have noted two distinct features in our moment maps and tilted-ring model residuals, the "stream-like" motion seen ~ 125 pc to the east of the nucleus as a redshifted component piercing into blueshifted rotational motions with ~ 30 km s^{-1} higher velocity dispersion than the rest of the disk, and the ~ 300 pc inner disk that seems to rotate differently, attributed to starburst activity (e.g. Elmouttie et al., 1998). The stream-like feature is most likely a wind caused by the starburst seen in the region, as Elmouttie et al. (1998) suggests.

The tilted-ring modeling to Circinus suggests the presence of cold molecular non-circular motions. In the major axis PVD we see a blueshifted motion at ~ -5" (~ 160 pc) and ~ -12" (~ 400 pc), which could be a direct indication of the NW-SE outflow reported in several studies, showing that the effect on this outflow could accelerate the cold molecular gas up to ~ 400 pc from the AGN. A better look on this can be seen in the minor axis PVD, where a blueshifted and redshifted component is seen moving at ~ 100 km s^{-1} in the NW-SE direction. In addition, symmetric inflow motions are observed in $\sim \pm 15$" (~ 500 pc), reaching high speeds of ~ 200 km s^{-1} in the NW-SE direction as well. This inflow could be caused by starburst dynamics rather than pure gravitational free-fall, due to the high velocities. This means that a system seen in some galaxies could be showing in Circinus as well, where the inflow transports material into the SMBH, driving the bi-conical outflow.

NGC 5643 : This galaxy is a barred Seyfert type II galaxy, seen almost face-on. NGC 5643 has a radio jet pointing in the east-west direction of the AGN, related to a bi-conical ionized outflow in the central regions (Riffel et al., 2018; Alonso-Herrero et al., 2018; García-Bernete, I. et al., 2021), causing a positive feedback effect (Cresci et al., 2015). This can be seen by overlapping [O III] with Hα emission, as well as the cold molecular gas content (see Fig. 9 of Alonso-Herrero et al., 2018), where concentrations of Hα emission is seen in the termination of the jet.

In our study with cold molecular gas, we find substantial amounts with $M_{H_2} = 5.5 \times 10^8 M_\odot$, however, no broad emission lines are seen (FWHM$_{CO} \sim 100$ km s^{-1}). This is interesting since this target is well studied in the cold molecular gas phase (e.g. Alonso-Herrero et al., 2018; García-Bernete, I. et al., 2021) showing clear inflow and outflow signs, with outflow masses of $\sim 5.2 \times 10^7 M_\odot$. Another feature seen in the literature and in our study is the concentration of cold molecular mass in the east and west spiral arm, where García-Bernete, I. et al. (2021) estimate that the east arm has $50 - 70\%$ the mass of the western arm, which can be seen in our moment 0 maps that display higher fluxes in the western region than in the east region. We also see a region east-side where no molecular gas is seen from ~ 50 to ~ 100 pc from the nucleus. Both of these features can be explained by the radio jet displacing the cold molecular gas and concentrating it ~ 100 pc from the nucleus, while creating a zone with no concentration and a depletion in the eastern arm.

Our kinematic analysis yields results identical to those shown in Alonso-Herrero et al. (2018), where they also fit the inner ~ 750 pc of the CO$(2-1)$ emission. The residuals in moment 1 and 2 maps resemble our NGC 1566 fit quite well in the central region, displaying residuals indicative of non-circular motions, redshifted towards the north-east of the galaxy and blueshifted towards the south-west direction. Taking the north-east as the far side, and south-west as the near side of the galaxy, we can analyze the PV diagrams to characterize this non-circular motions. As briefly mentioned in Sect. 4.5, the major axis PVD shows higher velocities (~ 250 km s^{-1}) in the inner $\sim \pm 1$" (~ 80 pc) than the average rotation speed (~ 100 km s^{-1}). This is also seen in the minor axis PVD, where in this central region velocities reach ~ 250 km s^{-1}, which is a sign of outflow motions in the innermost regions of the galactic disk. We can observe blueshifted motions at ~ -7" (~ 600 pc) and redshifted motions at ~ 3" (~ 250 pc), both signs of inflowing material. This could be a sign of nuclear bars present in the central regions of the galaxy, which can be seen in moment 0 maps and residuals. Outflowing motions may also be present at ~ -3" (~ 250 pc) from the nucleus, with speeds of ~ 50 km s^{-1}.

NGC 5995 : This target is documented as a Seyfert type II galaxy, containing an hidden BLR (HBLR) with broad Hβ and Hα emission lines (Lumsden et al., 2001). No previous studies have been done on this galaxy to the extent we reach in our work, so the literature on this source is limited.

We find significant amounts of CO$(2-1)$ up to ~ 7 kpc, with vast reservoirs in the central ~ 1 kpc of the galaxy. Our emission line profile is similar to that found in Salvestrini et al. (2022), showing a broad (FWHM$_{CO} \sim 470$ km s^{-1}) double-peaked Gaussian distribution due to spiral arm motion. We find a larger separation between peaks in comparison to the values reported in the study mentioned. Molecular gas masses coincide with the literature, estimating $M_{H_2} = 6.7 \times 10^9 M_\odot$ in our study, while values of $M_{H_2} = 7.24 \times 10^9$ are found in the literature (Salvestrini et al., 2022). We used a typical conversion parameter $\alpha_{CO} = 4.3 M_\odot$, whereas they decided to use the prescription by Narayanan et al. (2012), estimating $\alpha_{CO} = 1.78 M_\odot$ for NGC 5995. We report 3 times less S_{CO}

than Salvestrini et al. (2022).

No studies on kinematics and outflowing motions have been previously studied for this target. To analyze the minor axis PVD, we must know which side of the galaxy is the nearest and which side is the farthest. To do so, we analyze the trailing spiral arms and compare this motion to the redshifted and blueshifted sides of the rotation of the galaxy. The spiral arms show tails to the north-west (on the lower part of the galaxy) and south-east (on the higher part of the galaxy), therefore, concluding the gas rotation is counterclockwise. With this, we can conclude that the near side of the galaxy is in the NE direction, and the far side in the SW direction.

In the major axis PVD we can see a small feature ~ -2" from the AGN that shows a slightly redshifted motion compared to that of the galaxy, as well as peaks in speed at ~ -1" and ~ 0", suggesting a faster rotation in the inner regions of the galaxy compared fo the spiral arms. The minor axis PVD shows the inverted "V-shape" mentioned in Sect. 4.5, displaying clear signs of non-circular motions, which can also be seen in the residuals of the moment 1 maps. We can distinguish that the V-shape is mostly redshifted up to ~ -1.5" ($\sim$ 700 pc) from the nucleus, which means there is a massive inflow with speeds of $\sim$ 300 km s^{-1}. This can be seen in a lesser magnitude up to $\sim$ 1" ($\sim$ 500 pc), with speeds of $\sim$ 200 km s^{-1}. This can be directly related with the spiral arms seen in velocity dispersion map residuals, with the NE side showing higher velocity dispersions (hence the higher inflowing speeds), reaching $\sim$ 150 km s^{-1}, while the SW arm shows lower velocity dispersions ($\sim$ 100 km s^{-1}). Because this V-shape extends to both sides of the PVD, there must also be signs of outflows, at around the same regions of the inflows, displaying speeds of $\sim$ 200 km s^{-1} in the SW side and $\sim$ 150 km s^{-1} in the NE side. While the spatial overlap of inflowing and outflowing material in the same region appears contradictory, this behavior can be explained by a bi-conical outflow inclined relative to the galactic disk. In this geometry, the gas streams inward along the galaxy plane, while the expanding outflow extends out of the galactic plane. In the minor axis PVD we can see more content following an outflowing motion in the NE side than in the SW side, indicating that we are primarily detecting the near-side outflow cone emerging above the galactic disk, while the far-side cone remains obscured behind the molecular gas plane.

2MASX J1631+2352 : This target is cataloged as a triple merger, with 2 AGNs (determined via *Chandra* X-ray detections). In our observations, we only see SDSS $J163115.52 + 235257.5$ (alternate name) and the NE nucleus, both cataloged as AGNs (Foord et al., 2021). For simplicity, we will call each nucleus 2MASX and 2MASX NE.

The molecular gas content shows a vast reservoir of cold molecular gas in 2MASX NE, while almost no CO$(2-1)$ emission is seen in 2MASX, as seen in the moment 0 map. The depletion of CO$(2-1)$ from the AGN center in 2MASX could be a direct consequence of merger interaction (e.g. via tidal gas stripping). Fixing the center at 2MASX, there is not a clear rotational pattern, as the gas is mostly dispersed around the nucleus and is mostly unresolved. 2MASX NE shows a completely blueshifted motion compared to 2MASX, but this component does show a rotational pattern roughly along the NW-SE axis. Both nuclei show velocity dispersions of $\sim$ 50 km s^{-1}, but 2MASX seems to have the fastest velocity dispersions. Because there is no sign of steep velocity gradients (such as the ones seen in Mrk 463) and emission line with FWHM$_{CO} \sim$ 238 km s^{-1}, we cannot state that this target possesses outflowing motions of cold molecular gas.

3C 403 : This target is classified as a high-excitation radio galaxy (HERG), showing prominent optical emission lines. As discussed, this galaxy contains a radio jet that is understood to have undergone a reorientation due to a dual black hole system (Dennett-Thorpe et al., 2002; Tarchi, A. et al., 2007), and while this jet could be the mechanism by which the ionized outflow is driven, this was disproved, as it is believed that the winds are likely accelerated by the radiation released by the accretion process and not by the radio jet (Speranza et al., 2021).

The ring-like structure seen in this target, seen in moment maps and radial profiles, is not likely related to jet activity but rather to these accretion disk winds. The latter could have displaced the gas long enough ago for velocity dispersions on the ring to be very low (< 20) km s^{-1}. Another explanation could be ancient merger activity, more than 10^8 years ago, for which gaseous tracers of this activity would not be seen (Begelman et al., 1980). An interesting thing to note, is that the cocoon is co-spatial with the ionized flux emission in $[\mathrm{OIII}]_{\lambda 5007}$ corresponding to the ionized outflow, so there may be a connection between the ionized outflowing material and the CO$(2-1)$ ring.

In the moment 1 maps, we can see that the zero velocity is not centered on the AGN, but rather this structure seems blueshifted at the galaxy center, with high speeds (~ 150 km s^{-1}) towards the SW and NE regions. We find obvious signatures of CO$(2-1)$ reservoirs with $M_{\mathrm{H_2}} = 2.55 \times 10^8 M_\odot$, similar to that estimated in Speranza et al. (2021), mainly concentrated in the ring-like structure. Despite showing line widths of FWHM$_{\mathrm{CO}} \sim 350$ km s^{-1}, we cannot state that this is a sign of a molecular outflow, but rather the large width is likely due to the extended ring (~ 4 kpc).

IC 5063 : This target is a Seyfert type II hosted by an early-type galaxy, cataloged as one of the most radio bright Seyfert objects. It is well known for its jet-cloud interactions, as radio jets is present, colliding with dense ISM clouds at the two radio lobes, $\sim 300-500$ pc away from the nucleus, driving outflows.

We find large amounts of CO$(2-1)$ emission, corresponding to a total mass of $M_{\mathrm{H_2}} = 6.3 \times 10^8 M_\odot$, which is 57% less than that found in Morganti et al. (2015), however, this can be explained by the field of view used, as they used a 27" FOV, while we have a 16" FOV. We also find one of the broadest emission lines at FWHM$_{\mathrm{CO}} \sim 390$ km s^{-1}, with a similar profile to that of Morganti et al. (2015). The mass also seems to be concentrated in the 3 inner lobes, which can be seen in the radial profiles as 3 peaks in surface brightness. In this regions is where the bi-conical ionized outflow is located, more specifically in the western lobe, that is also the brightest in our CO$(2-1)$ data.

A thorough kinematic analysis has been done in several studies (e.g. Morganti et al., 2015; Mukherjee et al., 2018; Dasyra et al., 2024) to the gas and jet to understand the multi-phase outflow seen. We provide the tilted-ring fit performed on the inner regions (~ 1.5 kpc) of the galaxy, where the three most prominent lobes lie. From moment 1 residuals, we can observe that the zero-velocity is not situated at the exact AGN position, but rather east of the center, which causes massive blueshifted residuals seen north of the AGN position. An interesting feature seen in moment 1 maps and residuals is a redshifted region, roughly co-spatial with the bi-conical outflow seen (see Fig. 8 of Dasyra et al., 2024). Reported outflows are also seen on the SE and NW edges, which are seen in our mean velocity maps where rotation speeds reach ~ 315 km s^{-1}. This regions are not fitted with $^{3\mathrm{D}}$BBarolo, so we cannot see the residuals this incredibly fast moving gas produces. Velocity dispersions around the AGN and the western lobe reach up to ~ 185 km s^{-1}, whereas the eastern lobe shows velocity dispersions of ~ 40 km s^{-1}, which shows that the highest

velocity dispersions are displayed near the bi-conical outflow and AGN, as well as the western lobe.

PV diagram analysis will show the outflowing motions mentioned. Assuming that roughly NE corresponds to the far side and SW to the near side of the galaxy, we can observe outflowing motions in the minor axis PVD up to ~ -3" (~ 700 pc) from the AGN position, reaching speeds of ~ 150 km s^{-1}, and a ~ 200 km s^{-1} outflow roughly ~ 1" (~ 200 pc) west of the AGN position, where the bi-conical outflow is located. In the major axis PVD, we see non-rotational motions showing speeds of ~ 400 km s^{-1} in discrepancy with the normal rotational motion of the galaxy. We can see the blob roughly at the AGN position and the western lobe showing different rotation speeds compared with the rest of the gas in the galaxy, which can be attributed to the outflows seen in these regions.

3C 445 : The 3C 445 galaxy is cataloged as a Fanaroff-Riley type II radio galaxy in an isolated environment. It is listed as a source that has two tentative companions, as well as a non-detection of CO (Tadhunter et al., 2024). This source has two hotspots, one on the north side with an S-shape that is ~ 4.2 kpc in size, and a southern hotspot that is ~ 6.4 kpc in angular size (Orienti et al., 2020). Unlike 3C 33 and 3C 403, this source is cataloged as a broad-line object (BLO), however, the ionized outflow in these objects is also driven by radiation released by the accretion disk rather than the jet (Speranza et al., 2021). Among BLOs, this target shows the maximum velocity reached in the ionized phase traced by $[OIII]_{\lambda 5007}$.

This galaxy is the other non-detection in CO$(2-1)$, and one possibility for the depletion of the cold molecular gas from the central regions of the galaxy are radiatively driven accreting-disk winds. Another possibility is ancient merger interaction, since this galaxy has two potential companions, it is possible that at some moment these sources interacted with one another in a system like the one seen in 2MASX J1631+2352, where there is a triple merger system.

Mrk 926 : Mrk 926 is a Seyfert type I galaxy with very broad emission lines, its Balmer and helium lines having widths of more than 10000 km s^{-1}, known to be a very variable AGN, capable of dropping 50% of its luminosity in a period of 2.5 months (Kollatschny et al., 2022). It is the brightest member in a double system, with its companion located 1' to the south. No studies in the CO molecular gas phase have been done to this target.

The total CO$(2-1)$ mass estimated is $M_{H_2} = 2.4 \times 10^9 M_\odot$, making it one of the galaxies with the biggest cold molecular reservoirs in our sample, displaying broad (FWHM$_{CO} \sim 425$ km s^{-1}) emission lines as well in the central regions of the galaxy. As seen in the VLA map contours, Mrk 926 does contain radio emission in the central regions of the galaxy, some being co-spatial with the CO$(2-1)$ feature seen NW of the AGN, ~ 500 pc from the center. Although this galaxy is not cataloged as radio loud due to the lack of a prominent radio jet, there is significant emission in the direction of this CO$(2-1)$ feature, seen in 3" imaging of the radio continuum. This radio emission could be an indicator of shocks in the ISM due to an outflow, or it could very well be a small-scale central jet interacting with the surrounding gas. The fact that the gas seems displaced toward the NE region, the correlation between VLA observations and this feature, and the broad emission line could lead us to conclude that there is a molecular outflow in Mrk 926, driven by either an accretion disk wind or a small, compact jet. A future kinematic analysis with ^{3D}BBarolo could determine if this is the case or not, though evidence is strong enough to conclude the case that there is a molecular outflow in this source.

Chapter 6

Summary and Conclusions

In this work we have presented ALMA observations of the nuclear regions of X-ray selected AGN with ionized outflows, aimed at observing the cold molecular gas using CO$(2-1)$ as a tracer. The main conclusions from this work are the following:

i) We traced the cold (CO$(2-1)$) molecular gas phase in our 18 galaxy sample, detecting CO$(2-1)$ in 16 of 18 targets. We provide estimations of the CO line luminosities $L'_{\rm CO(2\text{-}1)}$ through multi-component Gaussian fits, finding luminosities range between 1.2×10^7 and 1.5×10^9 K km s^{-1} pc^2. Molecular gas masses $M_{\rm H_2}$ were estimated using a standard $\rm M_{H_2}$-to-CO conversion factor, finding masses range between 6.4×10^7 and 8.2×10^9 $M_\odot$ throughout our sample.

ii) No correlations were found between the molecular gas mass and $\rm FWHM_{CO}$ with the black hole mass. The molecular gas mass is correlated to the bolometric luminosity and Eddington ratio, whereas the $\rm FWHM_{CO}$ shows a small correlation only to the Eddington ratio.

iii) We provide integrated intensity, intensity-weighted mean velocity field and velocity dispersion maps, finding a wide range of CO$(2-1)$ intensities, rotational velocities and velocity dispersions. We characterized correlations with the radio continuum by comparing our CO$(2-1)$ data with archival VLA observations. We find that in NGC 4941 and Mrk 926 there are signs of outflowing motions that are co-spatial with the VLA observations, suggesting that the mechanism producing the radio continuum emission should also be responsible for the outflow. We also described the radial distribution of the cold molecular gas using radial profiles, finding that most targets exponentially decrease their CO$(2-1)$ surface brightness with the radius, with the exception of targets that display clear spiral arms or rings.

iv) We study two targets, 3C 403 and HE 0224-2834, in which we find prominent emission in the form of a ring-like structure at ~ 4 kpc away from the AGN, which could be the residual of ancient merger activity or powerful winds associated to accretion disk radiative processes. We find broad emission line widths of $\rm FWHM_{CO} \sim 348$ km s^{-1} and $\rm FWHM_{CO} \sim 334$ km s^{-1} for 3C 403 and HE 0224-2834, respectively, suggesting fast-rotating gas. We do not find clear evidence for non-circular motions, and a kinematic analysis on these sources is needed to determine whether non-circular motions are present.

v) We used tilted-ring modeling with ^{3D}BBarolo in the search of outflows for selected targets in our sample, from which we find evidence for non-circular motions in all sampled galaxies (IC 1657, NGC 1566, NGC 4941, Circinus, NGC 5643, NGC 5995 and IC 5063). Inflows were found in NGC 1566, NGC 4941, Circinus, NGC 5643 and NGC 5995, while outflows were seen in all targets mentioned, with the addition of IC 5063. Non-circular motions are reported in IC 1657, however, we are unable to describe if the motion is an inflow or outflow due to the highly inclined ($i \sim 81°$) galaxy plane. In the literature, there is a well studied bi-conical outflow in this target, perpendicular to the galaxy plane, so we argue the non-circular motion seen in our PV diagrams is due to this feature.

In conclusion, in this work we have exploited ALMA and archival VLA data to characterize the cold molecular gas phase in X-ray selected AGN with ionized outflows, in the search for correlations between the ionized and molecular phases of the documented outflows and understanding how feedback affects the evolution of the host galaxy. In particular, we study the $CO(2-1)$ rotational transition, estimating the molecular gas mass M_{H_2}, describing the cold molecular gas content, distribution, and kinematics, using tilted-ring modeling to look for non-circular motions.

Bibliography

Abeysekara, A. U., Albert, A., Alfaro, R., et al. 2017, The Astrophysical Journal, 843, 40, doi: 10.3847/1538-4357/aa7556

Adams, T. F. 1977, , 33, 19, doi: 10.1086/190416

Alatalo, K., Lacy, M., Lanz, L., et al. 2015, , 798, 31, doi: 10.1088/0004-637X/798/1/31

Alonso-Herrero, A., Pereira-Santaella, M., García-Burillo, S., et al. 2018, , 859, 144, doi: 10.3847/1538-4357/aabe30

Antonucci, R. 1993, , 31, 473, doi: 10.1146/annurev.aa.31.090193.002353

Asmus, D. 2019, , 489, 2177, doi: 10.1093/mnras/stz2289

Atwood, W. B., Abdo, A. A., Ackermann, M., et al. 2009, , 697, 1071, doi: 10.1088/0004-637X/697/2/1071

Baade, W., & Minkowski, R. 1954, , 119, 206, doi: 10.1086/145812

Baars, J. W. M., Hooghoudt, B. G., Mezger, P. G., & de Jonge, M. J. 1987, , 175, 319

Baldwin, J. A., Phillips, M. M., & Terlevich, R. 1981, , 93, 5, doi: 10.1086/130766

Baloković, M., Paneque, D., Madejski, G., et al. 2016, , 819, 156, doi: 10.3847/0004-637X/819/2/156

Barbosa, F. K. B., Storchi-Bergmann, T., Cid Fernandes, R., Winge, C., & Schmitt, H. 2009, , 396, 2, doi: 10.1111/j.1365-2966.2009.14485.x

Barthelmy, S. D., Barbier, L. M., Cummings, J. R., et al. 2005, Space Science Reviews, 120, 143–164, doi: 10.1007/s11214-005-5096-3

Barvainis, R. 1987, , 320, 537, doi: 10.1086/165571

Baumgartner, W. H., Tueller, J., Markwardt, C. B., et al. 2013, , 207, 19, doi: 10.1088/0067-0049/207/2/19

Begelman, M. C., Blandford, R. D., & Rees, M. J. 1980, , 287, 307, doi: 10.1038/287307a0

Begelman, M. C., Blandford, R. D., & Rees, M. J. 1984, Rev. Mod. Phys., 56, 255, doi: 10.1103/RevModPhys.56.255

Bellocchi, Enrica, Arribas, Santiago, Colina, Luis, & Miralles-Caballero, Daniel. 2013, AA, 557, A59, doi: 10.1051/0004-6361/201221019

Bentz, M. C., & Katz, S. 2015, , 127, 67, doi: 10.1086/679601

Bertram, T., Eckart, A., Fischer, S., et al. 2007, , 470, 571, doi: 10.1051/0004-6361:20077578

Bischetti, M., Maiolino, R., Carniani, S., et al. 2019, AA, 630, A59, doi: 10.1051/0004-6361/201833557

Blandford, R., Meier, D., & Readhead, A. 2019, , 57, 467, doi: 10.1146/annurev-astro-081817-051948

Blandford, R. D., & Königl, A. 1979, , 232, 34, doi: 10.1086/157262

Blandford, R. D., & McKee, C. F. 1982, , 255, 419, doi: 10.1086/159843

Blandford, R. D., & Payne, D. G. 1982, , 199, 883, doi: 10.1093/mnras/199.4.883

Blandford, R. D., & Rees, M. J. 1978, , 17, 265, doi: 10.1088/0031-8949/17/3/020

Blandford, R. D., & Znajek, R. L. 1977, , 179, 433, doi: 10.1093/mnras/179.3.433

Bolatto, A. D., Wolfire, M., & Leroy, A. K. 2013, , 51, 207, doi: 10.1146/annurev-astro-082812-140944

Bothwell, M. S., Smail, I., Chapman, S. C., et al. 2013, , 429, 3047, doi: 10.1093/mnras/sts562

Boyle, B. J., Fong, R., Shanks, T., & Peterson, B. A. 1987, , 227, 717, doi: 10.1093/mnras/227.3.717

Bradley, L., Sipocz, B., Robitaille, T., et al. 2016, Photutils: Photometry tools, Astrophysics Source Code Library, record ascl:1609.011. http://ascl.net/1609.011

Cano-Díaz, M., Maiolino, R., Marconi, A., et al. 2012, , 537, L8, doi: 10.1051/0004-6361/201118358

Carilli, C. L., & Walter, F. 2013, , 51, 105, doi: 10.1146/annurev-astro-082812-140953

Cazzoli, S., Márquez, I., Masegosa, J., et al. 2018, , 480, 1106, doi: 10.1093/mnras/sty1811

Churazov, E., Brüggen, M., Kaiser, C. R., Böhringer, H., & Forman, W. 2001, , 554, 261, doi: 10.1086/321357

Cicone, C., Maiolino, R., Sturm, E., et al. 2014, , 562, A21, doi: 10.1051/0004-6361/201322464

Cohen, M. H., Kellermann, K. I., Shaffer, D. B., et al. 1977, , 268, 405, doi: 10.1038/268405a0

Comastri, A. 2004, in Astrophysics and Space Science Library, Vol. 308, Supermassive Black Holes in the Distant Universe, ed. A. J. Barger, 245, doi: 10.1007/978-1-4020-2471-9_8

Combes, F., García-Burillo, S., Casasola, V., et al. 2014, , 565, A97, doi: 10.1051/0004-6361/201423433

Combes, F., García-Burillo, S., Casasola, V., et al. 2013, AA, 558, A124, doi: 10.1051/0004-6361/201322288

Comrie, A., Wang, K.-S., Hwang, Y.-H., et al. 2026, CARTA: The Cube Analysis and Rendering Tool for Astronomy, 5.1, Zenodo, doi: 10.5281/zenodo.18477253

Condon, J. J., & Ransom, S. M. 2016, Essential Radio Astronomy

Cortes, P. C., Asaki, Y., Cerrigone, L., et al. 2026, ALMA Technical Handbook, ALMA Doc. 13.3, ver. 1.0, ALMA, doi: 10.5281/zenodo.18793803

Couto, G. S., Storchi-Bergmann, T., & Schnorr-Müller, A. 2017, Monthly Notices of the Royal Astronomical Society, 469, 1573, doi: 10.1093/mnras/stx962

Cresci, G., Mainieri, V., Brusa, M., et al. 2015, , 799, 82, doi: 10.1088/0004-637X/799/1/82

Croton, D. J., Springel, V., White, S. D. M., et al. 2006, , 365, 11, doi: 10.1111/j.1365-2966.2005.09675.x

Crummy, J., Fabian, A. C., Gallo, L., & Ross, R. R. 2006, , 365, 1067, doi: 10.1111/j.1365-2966.2005.09844.x

Curran, S. J., Koribalski, B. S., & Bains, I. 2008, , 389, 63, doi: 10.1111/j.1365-2966.2008.13574.x

Dabrowski, I. 1984, Canadian Journal of Physics, 62, 1639, doi: 10.1139/p84-210

Dasyra, K. M., Paraschos, G. F., Combes, F., et al. 2024, , 977, 156, doi: 10.3847/1538-4357/ad89ba

Davidson, K., & Netzer, H. 1979, Rev. Mod. Phys., 51, 715, doi: 10.1103/RevModPhys.51.715

Davies, R., Baron, D., Shimizu, T., et al. 2020, Monthly Notices of the Royal Astronomical Society, 498, 4150, doi: 10.1093/mnras/staa2413

de Naurois, M., & Mazin, D. 2015, Comptes Rendus. Physique, 16, 610–627, doi: 10.1016/j.crhy.2015.08.011

Dennett-Thorpe, J., Scheuer, P. A. G., Laing, R. A., et al. 2002, , 330, 609, doi: 10.1046/j.1365-8711.2002.05106.x

Di Teodoro, E. M., & Fraternali, F. 2015, , 451, 3021, doi: 10.1093/mnras/stv1213

Doi, A., & Inoue, Y. 2016, , 68, 56, doi: 10.1093/pasj/psw052

Downes, D., & Solomon, P. M. 1998, , 507, 615, doi: 10.1086/306339

Dubois, Y., Beckmann, R., Bournaud, F., et al. 2021, , 651, A109, doi: 10.1051/0004-6361/202039429

Duras, F., Bongiorno, A., Piconcelli, E., et al. 2017, , 604, A67, doi: 10.1051/0004-6361/201731052

Duras, F., Bongiorno, A., Ricci, F., et al. 2020, , 636, A73, doi: 10.1051/0004-6361/201936817

Elbaz, D., Dickinson, M., Hwang, H. S., et al. 2011, , 533, A119, doi: 10.1051/0004-6361/201117239

Elitzur, M., Nenkova, M., & Ivezić, Z. 2004, in Astronomical Society of the Pacific Conference Series, Vol. 320, The Neutral ISM in Starburst Galaxies, ed. S. Aalto, S. Huttemeister, & A. Pedlar, 242, doi: 10.48550/arXiv.astro-ph/0309040

Elitzur, M., & Shlosman, I. 2006, , 648, L101, doi: 10.1086/508158

Elmouttie, M., Krause, M., Haynes, R. F., & Jones, K. L. 1998, , 300, 1119, doi: 10.1046/j.1365-8711.1998.02002.x

Elvis, M. 2000, , 545, 63, doi: 10.1086/317778

Elvis, M., Wilkes, B. J., McDowell, J. C., et al. 1994, , 95, 1, doi: 10.1086/192093

Esposito, Federico, Alonso-Herrero, Almudena, García-Burillo, Santiago, et al. 2024, AA, 686, A46, doi: 10.1051/0004-6361/202449245

Fabian, A. C. 2012, , 50, 455, doi: 10.1146/annurev-astro-081811-125521

Fabian, A. C., Lohfink, A., Kara, E., et al. 2015, , 451, 4375, doi: 10.1093/mnras/stv1218

Fanaroff, B. L., & Riley, J. M. 1974, , 167, 31P, doi: 10.1093/mnras/167.1.31P

Faucher-Giguère, C.-A., & Quataert, E. 2012, Monthly Notices of the Royal Astronomical Society, 425, 605, doi: 10.1111/j.1365-2966.2012.21512.x

Feruglio, C., Maiolino, R., Piconcelli, E., et al. 2010, , 518, L155, doi: 10.1051/0004-6361/201015164

Fiore, F., Feruglio, C., Shankar, F., et al. 2017, , 601, A143, doi: 10.1051/0004-6361/201629478

Fluetsch, A., Maiolino, R., Carniani, S., et al. 2019, , 483, 4586, doi: 10.1093/mnras/sty3449

Fluetsch, A., Maiolino, R., Carniani, S., et al. 2021, Monthly Notices of the Royal Astronomical Society, 505, 5753, doi: 10.1093/mnras/stab1666

Foord, A., Gültekin, K., Runnoe, J. C., & Koss, M. J. 2021, , 907, 72, doi: 10.3847/1538-4357/abce5e

Fossati, G., Maraschi, L., Celotti, A., Comastri, A., & Ghisellini, G. 1998, , 299, 433, doi: 10.1046/j.1365-8711.1998.01828.x

Gao, Y., & Solomon, P. M. 2004, , 606, 271, doi: 10.1086/382999

García-Burillo, S., Alonso-Herrero, A., Ramos Almeida, C., et al. 2021, , 652, A98, doi: 10.1051/0004-6361/202141075

García-Bernete, I., Alonso-Herrero, A., García-Burillo, S., et al. 2021, AA, 645, A21, doi: 10.1051/0004-6361/202038256

Gardner, J. P., Mather, J. C., Clampin, M., et al. 2006, , 123, 485, doi: 10.1007/s11214-006-8315-7

Gehrels, N., Chincarini, G., Giommi, P., et al. 2004, , 611, 1005, doi: 10.1086/422091

Genzel, R., Tacconi, L. J., Lutz, D., et al. 2015, , 800, 20, doi: 10.1088/0004-637X/800/1/20

Ghisellini, G., Celotti, A., Fossati, G., Maraschi, L., & Comastri, A. 1998, , 301, 451, doi: 10.1046/j.1365-8711.1998.02032.x

Ghisellini, G., Tavecchio, F., Foschini, L., et al. 2010, , 402, 497, doi: 10.1111/j.1365-2966.2009.15898.x

Ghisellini, G., Tavecchio, F., & Ghirlanda, G. 2009, , 399, 2041, doi: 10.1111/j.1365-2966.2009.15397.x

Giovannini, G., Taylor, G. B., Feretti, L., et al. 2005, The Astrophysical Journal, 618, 635, doi: 10.1086/426106

González-Alfonso, E., Fischer, J., Spoon, H. W. W., et al. 2017, , 836, 11, doi: 10.3847/1538-4357/836/1/11

Green, R. F., Schmidt, M., & Liebert, J. 1986, , 61, 305, doi: 10.1086/191115

Grier, C. J., Trump, J. R., Shen, Y., et al. 2017, , 851, 21, doi: 10.3847/1538-4357/aa98dc

Gültekin, K., Richstone, D. O., Gebhardt, K., et al. 2009, , 698, 198, doi: 10.1088/0004-637X/698/1/198

Haardt, F., & Maraschi, L. 1991, , 380, L51, doi: 10.1086/186171

Haidar, H., Rosario, D. J., Alonso-Herrero, A., et al. 2024, , 532, 4645, doi: 10.1093/mnras/stae1596

Harrison, C. 2014, PhD thesis, Durham University, UK

Harrison, C. M., Costa, T., Tadhunter, C. N., et al. 2018, Nature Astronomy, 2, 198, doi: 10.1038/s41550-018-0403-6

Herrera-Camus, R., Janssen, A., Sturm, E., et al. 2020, , 635, A47, doi: 10.1051/0004-6361/201936434

Hickox, R. C., & Alexander, D. M. 2018, , 56, 625, doi: 10.1146/annurev-astro-081817-051803

Ho, L. C. 2008, , 46, 475, doi: 10.1146/annurev.astro.45.051806.110546

Ho, L. C., Filippenko, A. V., & Sargent, W. L. W. 1997, , 112, 315, doi: 10.1086/313041

Hodge, J. A., & da Cunha, E. 2020, Royal Society Open Science, 7, 200556, doi: 10.1098/rsos.200556

Holland, W. S., Robson, E. I., Gear, W. K., et al. 1999, , 303, 659, doi: 10.1046/j.1365-8711.1999.02111.x

Hönig, S. F., Kishimoto, M., Tristram, K. R. W., et al. 2013, , 771, 87, doi: 10.1088/0004-637X/771/2/87

Houck, J. R., Roellig, T. L., van Cleve, J., et al. 2004, , 154, 18, doi: 10.1086/423134

Hubble, E. P. 1926, , 64, 321, doi: 10.1086/143018

Husemann, B., Scharwächter, J., Davis, T. A., et al. 2019, , 627, A53, doi: 10.1051/0004-6361/201935283

Husemann, B., Singha, M., Scharwächter, J., et al. 2022, , 659, A124, doi: 10.1051/0004-6361/202141312

Ilha, G. S., Harrison, C. M., Mainieri, V., et al. 2025, , 704, A293, doi: 10.1051/0004-6361/202555730

Ishibashi, W., & Fabian, A. C. 2012, , 427, 2998, doi: 10.1111/j.1365-2966.2012.22074.x

Jansen, F., Lumb, D., Altieri, B., et al. 2001, , 365, L1, doi: 10.1051/0004-6361:20000036

Jennison, R. C., & Das Gupta, M. K. 1953, , 172, 996, doi: 10.1038/172996a0

Jones, T. W., O'Dell, S. L., & Stein, W. A. 1974, , 188, 353, doi: 10.1086/152724

Kader, J. A., U, V., Barcos-Muñoz, L., et al. 2026, Science, 391, 911, doi: 10.1126/science.adp8989

Kakkad, D., Sani, E., Rojas, A. F., et al. 2022, , 511, 2105, doi: 10.1093/mnras/stac103

Kauffmann, G., Heckman, T. M., Tremonti, C., et al. 2003, , 346, 1055, doi: 10.1111/j.1365-2966.2003.07154.x

Kellermann, K. I., & Pauliny-Toth, I. I. K. 1969, , 155, L71, doi: 10.1086/180305

Kellermann, K. I., Sramek, R., Schmidt, M., Shaffer, D. B., & Green, R. 1989, , 98, 1195, doi: 10.1086/115207

Kellermann, K. I., & Verschuur, G. L. 1988, Galactic and Extragalactic Radio Astronomy

Kelley, R., & Tashiro, M. 2024, in American Astronomical Society Meeting Abstracts, Vol. 243, American Astronomical Society Meeting Abstracts #243, 117.01

Kennicutt, R. C., & Evans, N. J. 2012, , 50, 531, doi: 10.1146/annurev-astro-081811-125610

Khachikian, E. E., & Weedman, D. W. 1971, Astrofizika, 7, 389

Kim, D. E., Di Gesu, L., Marin, F., et al. 2024, Galaxies, 12, 20, doi: 10.3390/galaxies12030020

King, A., & Pounds, K. 2015, , 53, 115, doi: 10.1146/annurev-astro-082214-122316

King, A. R. 2010, Monthly Notices of the Royal Astronomical Society, 402, 1516, doi: 10.1111/j.1365-2966.2009.16013.x

Kollatschny, W., Ochmann, M. W., Kaspi, S., et al. 2022, , 657, A122, doi: 10.1051/0004-6361/202142007

Kolykhalov, P. I., & Sunyaev, R. A. 1984, Advances in Space Research, 3, 249, doi: 10.1016/0273-1177(84)90100-5

König, S., Eckart, A., García-Marín, M., & Huchtmeier, W. K. 2009, , 507, 757, doi: 10.1051/0004-6361/200912546

Kormendy, J., & Ho, L. C. 2013, , 51, 511, doi: 10.1146/annurev-astro-082708-101811

Koshida, S., Minezaki, T., Yoshii, Y., et al. 2014, The Astrophysical Journal, 788, 159, doi: 10.1088/0004-637X/788/2/159

Koss, M., Trakhtenbrot, B., Ricci, C., et al. 2017, , 850, 74, doi: 10.3847/1538-4357/aa8ec9

Koss, M. J., Strittmatter, B., Lamperti, I., et al. 2021, , 252, 29, doi: 10.3847/1538-4365/abcbfe

Koss, M. J., Ricci, C., Trakhtenbrot, B., et al. 2022, , 261, 2, doi: 10.3847/1538-4365/ac6c05

Lamperti, I., Koss, M., Trakhtenbrot, B., et al. 2017, Monthly Notices of the Royal Astronomical Society, 467, 540, doi: 10.1093/mnras/stx055

Landt, H., Cheung, C. C., & Healey, S. E. 2010, , 408, 1103, doi: 10.1111/j.1365-2966.2010.17183.x

Lawrence, A. 1991, , 252, 586, doi: 10.1093/mnras/252.4.586

Leahy, J. P., & Perley, R. A. 1991, , 102, 537, doi: 10.1086/115892

Leftley, J. H., Nesvadba, N. P. H., Bicknell, G. V., et al. 2024, , 689, A314, doi: 10.1051/0004-6361/202449848

López-Cobá, C., Sánchez, S. F., Anderson, J. P., et al. 2020, , 159, 167, doi: 10.3847/1538-3881/ab7848

Lumsden, S. L., Heisler, C. A., Bailey, J. A., Hough, J. H., & Young, S. 2001, , 327, 459, doi: 10.1046/j.1365-8711.2001.04741.x

Macchetto, F., Capetti, A., Sparks, W. B., Axon, D. J., & Boksenberg, A. 1994, , 435, L15, doi: 10.1086/187583

Madejski, G. G., & Sikora, M. 2016, , 54, 725, doi: 10.1146/annurev-astro-081913-040044

Malkan, M. A. 1983, , 268, 582, doi: 10.1086/160981

Marconcini, C., Feltre, A., Lamperti, I., et al. 2025, AA, 701, A113, doi: 10.1051/0004-6361/202554797

Mason, B. S., & Brogan, C. 2013, Relative Integration Times for the ALMA 12-m, 7-m, and Total Power Arrays, Tech. Rep. NAASC Memo #113, National Radio Astronomy Observatory (NRAO)

Matt, G., Brandt, W. N., & Fabian, A. C. 1996, Monthly Notices of the Royal Astronomical Society, 280, 823, doi: 10.1093/mnras/280.3.823

Matt, G., Fabian, A. C., Guainazzi, M., et al. 2000, Monthly Notices of the Royal Astronomical Society, 318, 173, doi: 10.1046/j.1365-8711.2000.03721.x

McConnell, N. J., & Ma, C.-P. 2013, , 764, 184, doi: 10.1088/0004-637X/764/2/184

McNamara, B. R., & Nulsen, P. E. J. 2007, , 45, 117, doi: 10.1146/annurev.astro.45.051806.110625

Mitsuda, K., Bautz, M., Inoue, H., et al. 2007, Publications of the Astronomical Society of Japan, 59, S1, doi: 10.1093/pasj/59.sp1.S1

Morganti, R. 2017, Frontiers in Astronomy and Space Sciences, 4, 42, doi: 10.3389/fspas.2017.00042

Morganti, R., Fogasy, J., Paragi, Z., Oosterloo, T., & Orienti, M. 2013, Science, 341, 1082, doi: 10.1126/science.1240436

Morganti, R., Oosterloo, T., Oonk, J. B. R., Frieswijk, W., & Tadhunter, C. 2015, , 580, A1, doi: 10.1051/0004-6361/201525860

Morganti, R., Veilleux, S., Oosterloo, T., Teng, S. H., & Rupke, D. 2016, , 593, A30, doi: 10.1051/0004-6361/201628978

Mukherjee, D., Wagner, A. Y., Bicknell, G. V., et al. 2018, , 476, 80, doi: 10.1093/mnras/sty067

Mundell, C. G., Wilson, A. S., Ulvestad, J. S., & Roy, A. L. 2000, The Astrophysical Journal, 529, 816, doi: 10.1086/308318

Nandra, K., & Pounds, K. A. 1994, Monthly Notices of the Royal Astronomical Society, 268, 405, doi: 10.1093/mnras/268.2.405

Narayan, R., & Yi, I. 1994, , 428, L13, doi: 10.1086/187381

—. 1995, , 444, 231, doi: 10.1086/175599

Narayanan, D., Krumholz, M. R., Ostriker, E. C., & Hernquist, L. 2012, , 421, 3127, doi: 10.1111/j.1365-2966.2012.20536.x

Nardini, E., Reeves, J. N., Gofford, J., et al. 2015, Science, 347, 860, doi: 10.1126/science.1259202

Nelson, C. H., & Whittle, M. 1996, , 465, 96, doi: 10.1086/177405

Nenkova, M., Ivezić, Ž., & Elitzur, M. 2002, , 570, L9, doi: 10.1086/340857

Nenkova, M., Sirocky, M. M., Ivezić, Ž., & Elitzur, M. 2008, , 685, 147, doi: 10.1086/590482

Netzer, H. 2013, The Physics and Evolution of Active Galactic Nuclei

Neugebauer, G., Habing, H. J., van Duinen, R., et al. 1984, , 278, L1, doi: 10.1086/184209

Nicastro, F. 2000, The Astrophysical Journal, 530, L65, doi: 10.1086/312491

Oh, K., Schawinski, K., Koss, M., et al. 2017, Monthly Notices of the Royal Astronomical Society, 464, 1466, doi: 10.1093/mnras/stw2467

Oh, K., Koss, M. J., Ueda, Y., et al. 2022, , 261, 4, doi: 10.3847/1538-4365/ac5b68

Orienti, M., Migliori, G., Brunetti, G., et al. 2020, , 494, 2244, doi: 10.1093/mnras/staa777

Osterbrock, D. E., & Ferland, G. J. 2006, Astrophysics of gaseous nebulae and active galactic nuclei

Padovani, P. 2017, Frontiers in Astronomy and Space Sciences, 4, 35, doi: 10.3389/fspas.2017.00035

Padovani, P., Alexander, D. M., Assef, R. J., et al. 2017, , 25, 2, doi: 10.1007/s00159-017-0102-9

Papadopoulos, P. P., van der Werf, P., Xilouris, E., Isaak, K. G., & Gao, Y. 2012, The Astrophysical Journal, 751, 10, doi: 10.1088/0004-637X/751/1/10

Peacock, J. A., & Wall, J. V. 1981, , 194, 331, doi: 10.1093/mnras/194.2.331

Peterson, B. M. 1993, , 105, 247, doi: 10.1086/133140

Pillepich, A., Springel, V., Nelson, D., et al. 2018, , 473, 4077, doi: 10.1093/mnras/stx2656

Planck Collaboration, Aghanim, N., Akrami, Y., et al. 2020, , 641, A6, doi: 10.1051/0004-6361/201833910

Pogge, R. W. 1989, , 345, 730, doi: 10.1086/167945

Powell, M. C., Husemann, B., Tremblay, G. R., et al. 2018, , 618, A27, doi: 10.1051/0004-6361/201833424

Proga, D., Stone, J. M., & Kallman, T. R. 2000, , 543, 686, doi: 10.1086/317154

Readhead, A. C. S., Cohen, M. H., Pearson, T. J., & Wilkinson, P. N. 1978, , 276, 768, doi: 10.1038/276768a0

Reber, G. 1944, , 100, 279, doi: 10.1086/144668

Ricci, C., Ueda, Y., Koss, M. J., et al. 2015, , 815, L13, doi: 10.1088/2041-8205/815/1/L13

Ricci, C., Trakhtenbrot, B., Koss, M. J., et al. 2017, , 233, 17, doi: 10.3847/1538-4365/aa96ad

Richards, G. T., Lacy, M., Storrie-Lombardi, L. J., et al. 2006, , 166, 470, doi: 10.1086/506525

Rieke, G. H., Wright, G. S., Böker, T., et al. 2015, , 127, 584, doi: 10.1086/682252

Riffel, R. A., Hekatelyne, C., & Freitas, I. C. 2018, , 35, e040, doi: 10.1017/pasa.2018.31

Roberts-Borsani, G. W., & Saintonge, A. 2019, Monthly Notices of the Royal Astronomical Society, 482, 4111, doi: 10.1093/mnras/sty2824

Rosario, D. J., Burtscher, L., Davies, R. I., et al. 2018, , 473, 5658, doi: 10.1093/mnras/stx2670

Saintonge, A., Catinella, B., Tacconi, L. J., et al. 2017, , 233, 22, doi: 10.3847/1538-4365/aa97e0

Salpeter, E. E. 1977, , 15, 267, doi: 10.1146/annurev.aa.15.090177.001411

Salvestrini, F., Gruppioni, C., Hatziminaoglou, E., et al. 2022, , 663, A28, doi: 10.1051/0004-6361/202142760

Sanders, D. B., & Mirabel, I. F. 1996, , 34, 749, doi: 10.1146/annurev.astro.34.1.749

Sanders, D. B., Phinney, E. S., Neugebauer, G., Soifer, B. T., & Matthews, K. 1989, , 347, 29, doi: 10.1086/168094

Sanders, D. B., Soifer, B. T., Elias, J. H., et al. 1988, , 325, 74, doi: 10.1086/165983

Schmitt, H. R., Donley, J. L., Antonucci, R. R. J., Hutchings, J. B., & Kinney, A. L. 2003, , 148, 327, doi: 10.1086/377440

Schöier, F. L., van der Tak, F. F. S., van Dishoeck, E. F., & Black, J. H. 2005, A&A, 432, 369, doi: 10.1051/0004-6361:20041729

Shakura, N. I., & Sunyaev, R. A. 1973, , 24, 337

Shangguan, J., Ho, L. C., & Xie, Y. 2018, , 854, 158, doi: 10.3847/1538-4357/aaa9be

Shields, G. A. 1978, , 272, 706, doi: 10.1038/272706a0

Slater, R., Nagar, N. M., Schnorr-Müller, A., et al. 2019, , 621, A83, doi: 10.1051/0004-6361/201730634

Solomon, P. M., Downes, D., Radford, S. J. E., & Barrett, J. W. 1997, , 478, 144, doi: 10.1086/303765

Solomon, P. M., & Vanden Bout, P. A. 2005, , 43, 677, doi: 10.1146/annurev.astro.43.051804.102221

Soto, K. T., Martin, C. L., Prescott, M. K. M., & Armus, L. 2012, , 757, 86, doi: 10.1088/0004-637X/757/1/86

Speranza, G., Balmaverde, B., Capetti, A., et al. 2021, , 653, A150, doi: 10.1051/0004-6361/202140686

Spoon, H. W. W., Farrah, D., Lebouteiller, V., et al. 2013, The Astrophysical Journal, 775, 127, doi: 10.1088/0004-637X/775/2/127

Storchi-Bergmann, T., Wilson, A. S., & Baldwin, J. A. 1992, , 396, 45, doi: 10.1086/171696

Stuber, S. K., Schinnerer, E., Williams, T. G., et al. 2023, , 676, A113, doi: 10.1051/0004-6361/202346318

Sturm, E., González-Alfonso, E., Veilleux, S., et al. 2011, , 733, L16, doi: 10.1088/2041-8205/733/1/L16

Tacconi, L. J., Genzel, R., Neri, R., et al. 2010, , 463, 781, doi: 10.1038/nature08773

Tadhunter, C., Oosterloo, T., Morganti, R., et al. 2024, , 532, 4463, doi: 10.1093/mnras/stae1745

Tadhunter, C., & Tsvetanov, Z. 1989, , 341, 422, doi: 10.1038/341422a0

Tarchi, A., Brunthaler, A., Henkel, C., et al. 2007, AA, 475, 497, doi: 10.1051/0004-6361:20078317

Tavani, M., Barbiellini, G., Argan, A., et al. 2009, , 502, 995, doi: 10.1051/0004-6361/200810527

Teague, R., & Foreman-Mackey, D. 2018, Research Notes of the American Astronomical Society, 2, 173, doi: 10.3847/2515-5172/aae265

Terlevich, E., Diaz, A. I., & Terlevich, R. 1990, , 242, 271, doi: 10.1093/mnras/242.3.271

Tombesi, F., Cappi, M., Reeves, J. N., et al. 2013, , 430, 1102, doi: 10.1093/mnras/sts692

Treister, E., Privon, G. C., Sartori, L. F., et al. 2018, , 854, 83, doi: 10.3847/1538-4357/aaa963

Turner, T. J., & Miller, L. 2009, , 17, 47, doi: 10.1007/s00159-009-0017-1

Ueda, Y., Akiyama, M., Ohta, K., & Miyaji, T. 2003, , 598, 886, doi: 10.1086/378940

Ulrich, M.-H., Maraschi, L., & Urry, C. M. 1997, Annual Review of Astronomy and Astrophysics, 35, 445, doi: https://doi.org/10.1146/annurev.astro.35.1.445

Urry, C. M., & Padovani, P. 1995, , 107, 803, doi: 10.1086/133630

van Marrewijk, J., Morris, T. W., Mroczkowski, T., et al. 2024, The Open Journal of Astrophysics, 7, doi: 10.33232/001c.127571

Vanden Berk, D. E., Richards, G. T., Bauer, A., et al. 2001, The Astronomical Journal, 122, 549–564, doi: 10.1086/321167

Veilleux, S., Meléndez, M., Sturm, E., et al. 2013, , 776, 27, doi: 10.1088/0004-637X/776/1/27

Wade, C. M. 1968, , 73, 876, doi: 10.1086/110727

Wang, K.-S., Simmonds, R., Comrie, A., et al. 2026, , 138, 024506, doi: 10.1088/1538-3873/ae3eb4

Weaver, K. A. A., Cann, J. M., Pfeifle, R., et al. 2026, Frontiers in Astronomy and Space Sciences, Volume 13 - 2026, doi: 10.3389/fspas.2026.1790876

Weisskopf, M. C., Tananbaum, H. D., Van Speybroeck, L. P., & O'Dell, S. L. 2000, in X-Ray Optics, Instruments, and Missions III, ed. J. E. Truemper & B. Aschenbach, Vol. 4012 (SPIE), 2–16, doi: 10.1117/12.391545

Weizsäcker, C. F. 1948, Zeitschrift Naturforschung Teil A, 3, 524, doi: 10.1515/zna-1948-8-1118

Werner, M. W., Roellig, T. L., Low, F. J., et al. 2004, , 154, 1, doi: 10.1086/422992

Woo, J.-H., & Urry, C. M. 2002, , 579, 530, doi: 10.1086/342878

Wootten, A., & Thompson, A. 2009, Proceedings of the IEEE, 97, 1463–1471, doi: 10.1109/jproc.2009.2020572

Wright, E. L. 2006, , 118, 1711, doi: 10.1086/510102

York, D. G., Adelman, J., Anderson, Jr., J. E., et al. 2000, , 120, 1579, doi: 10.1086/301513

Zschaechner, L. K., Walter, F., Bolatto, A., et al. 2016, The Astrophysical Journal, 832, 142, doi: 10.3847/0004-637x/832/2/142

Zschaechner, L. K., Bolatto, A. D., Walter, F., et al. 2018, , 867, 111, doi: 10.3847/1538-4357/aadf32

Chapter 7

Appendix A: Gaussian fits

Figures 7.1 and 7.2 show the Gaussian fits performed to the ALMA CO$(2-1)$ emission lines. The BIC test was performed using Equations 3.3 and 3.4, and results are shown in Tables 7.1 and 7.2. As mentioned in 3.1, we perform this test only for emission lines that can be represented by more than one Gaussian component.

Table 7.1: Goodness-of-fit statistics and model comparison for the number of Gaussian components fitted to an emission line. ΔBIC is defined relative to the preferred model (BIC $-$ BIC$_{\rm min}$). The model in bold letters is the preferred one for the fit. One-component Gaussian fits are excluded.

Target	Components	χ^2	d.o.f.	$\chi^2_{\rm red}$	BIC	ΔBIC
NGC 424	**1**	**327.99**	**242**	**1.355**	**350.01**	**0**
	2	322.92	239	1.351	361.45	11.44
	3	304.42	236	1.290	359.47	9.46
IC 1657	1	1419.27	242	5.865	1441.29	1066.25
	2	444.25	239	1.859	482.79	107.75
	4	329.31	233	1.413	400.88	25.84
	6	**270.44**	**227**	**1.191**	**375.04**	**0**
HE 0224-2834	1	427.16	243	1.758	449.2	70.85
	2	**339.79**	**240**	**1.416**	**378.35**	**0**
	3	316.48	237	1.335	371.58	-6.77
NGC 985	1	391.53	240	1.631	413.52	31.07
	2	**343.97**	**237**	**1.451**	**382.45**	**0**
	3	337.34	234	1.442	392.32	9.87
NGC 1566	1	16635.01	240	69.313	16657.00	15109.16
	2	1800.96	237	7.599	1839.44	291.6
	3	**1492.86**	**234**	**6.380**	**1547.84**	**0**

Table 7.2: Continued.

Target	Components	χ^2	d.o.f.	$\chi^2_{\rm red}$	BIC	ΔBIC
NGC 4941	1	1605.44	241	6.662	1627.44	1178.93
	2	606.01	238	2.546	644.52	196.01
	3	546.54	235	2.326	601.55	153.04
	4	**376.99**	**232**	**1.625**	**448.51**	**0**
Mrk 463	1	317.46	239	1.328	339.43	76.56
	2	277.14	236	1.174	315.59	52.72
	3	265.66	233	1.140	320.59	57.72
	4	**191.46**	**230**	**0.832**	**262.87**	**0**
Circinus	1	411307.21	242	1699.617	411329.23	408970.68
	2	157054.29	239	657.131	157092.83	154734.28
	3	61106.19	236	258.925	61161.24	58802.69
	4	19900.72	233	85.411	19972.29	17613.74
	5	11098.36	230	48.254	11186.45	8827.9
	6	**2253.95**	**227**	**9.929**	**2358.55**	**0**
NGC 5995	1	4205.18	239	17.595	4227.15	3692.17
	2	1626.15	236	6.890	1664.60	1129.62
	3	722.34	233	3.100	777.27	242.29
	4	**463.57**	**230**	**2.016**	**534.98**	**0**
2MASX J1631+2352	1	804.95	239	3.368	826.92	391.58
	2	**396.88**	**236**	**1.682**	**435.34**	**0**
3C 403	**1**	**278.87**	**239**	**1.167**	**300.85**	**0**
	2	273.34	236	1.158	311.79	10.94
IC 5063	**1**	**694.23**	**242**	**2.869**	**716.25**	**0**
	2	668.94	239	2.799	707.48	-8.77
	3	658.38	236	2.790	713.43	-2.82
Mrk 926	**1**	**402.99**	**239**	**1.686**	**424.96**	**0**
	2	394.92	236	1.673	433.37	8.41

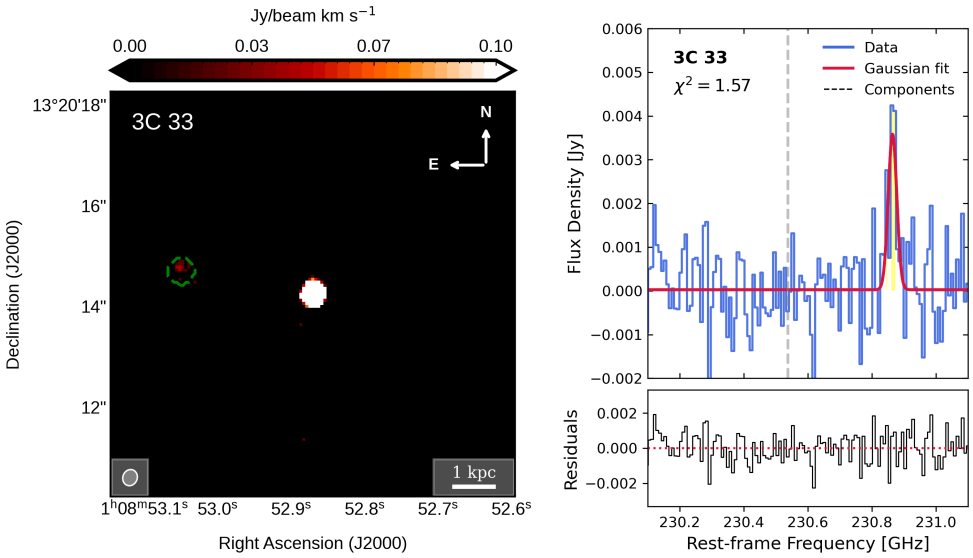


Figure 7.1: Gaussian fit for 3C 33, whose $S_{\rm CO}$ value is among the highest from the sample. *Left panel*: Aperture selected to obtain the emission line overlaid in the moment 0 map. The lines shown are selected by highest flux (such as in this case), as the presence of mergers requires multiple line fits at different regions. For disk-like galaxies, the line shown represents the total emission from the source. *Right panel*: Gaussian fit to the emission line. Solid blue lines represent the spectrum shape, black dotted lines represent the components used to perform the fit, solid red line is the fitted spectrum and the dotted green region is the aperture used. The reduced χ^2 is also added. Residuals are measured as 5σ. The yellow denotes that the line emission is above 3σ.

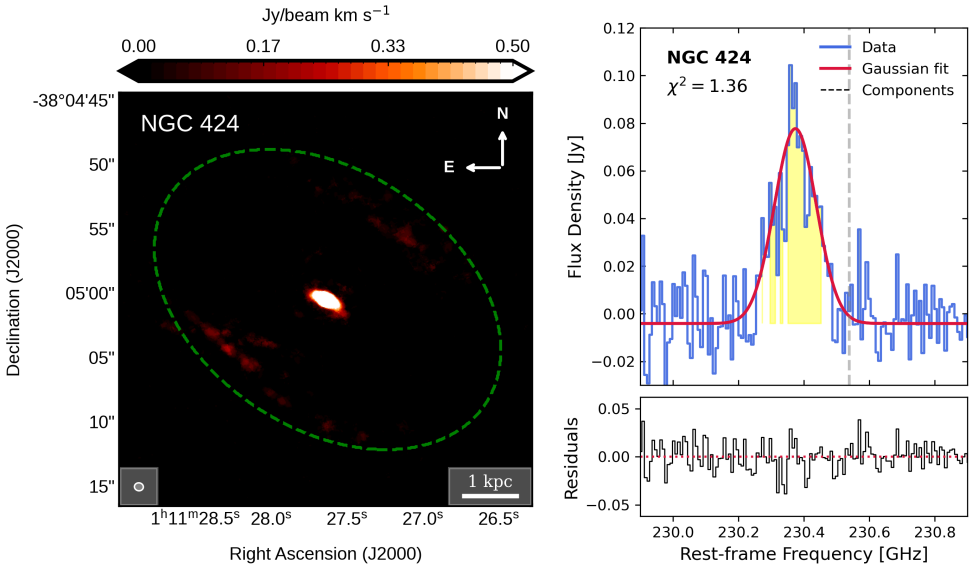


Figure 7.2: Same as 7.1 but for NGC 424.

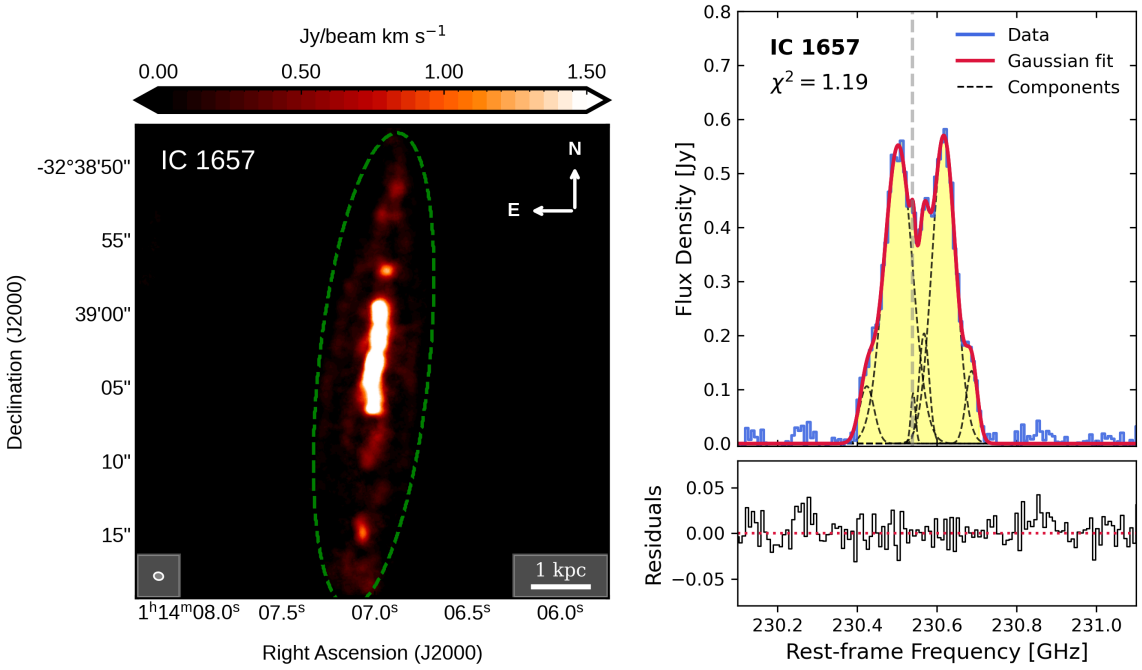


Figure 7.3: Same as 7.1 but for IC 1657.

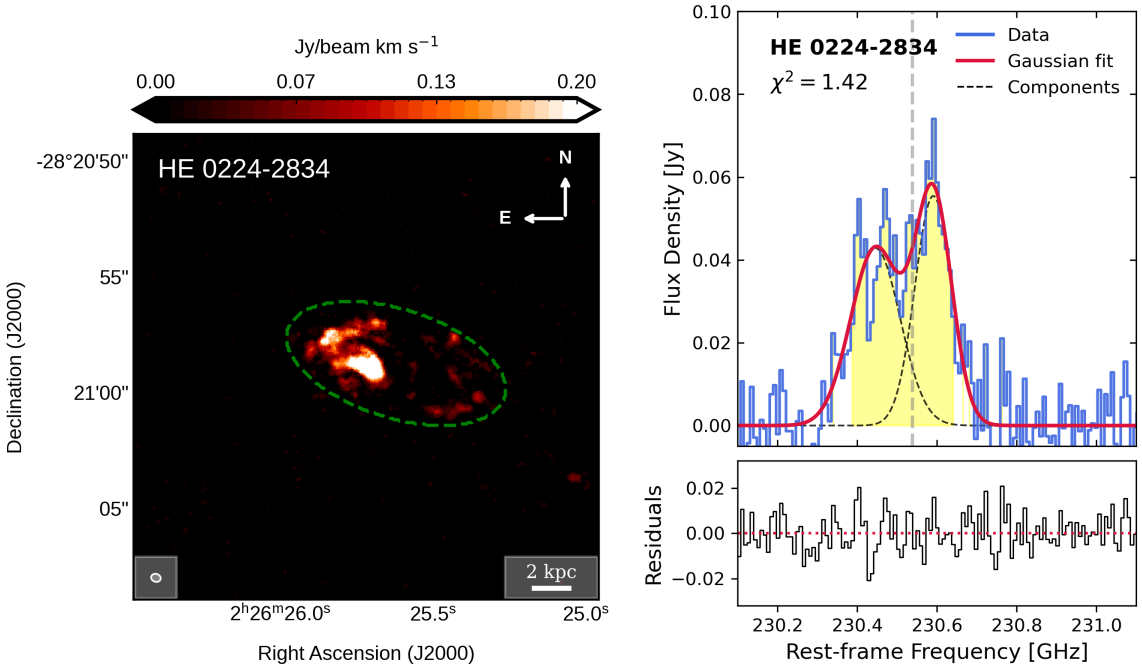


Figure 7.4: Same as 7.1 but for HE 0224-2834.

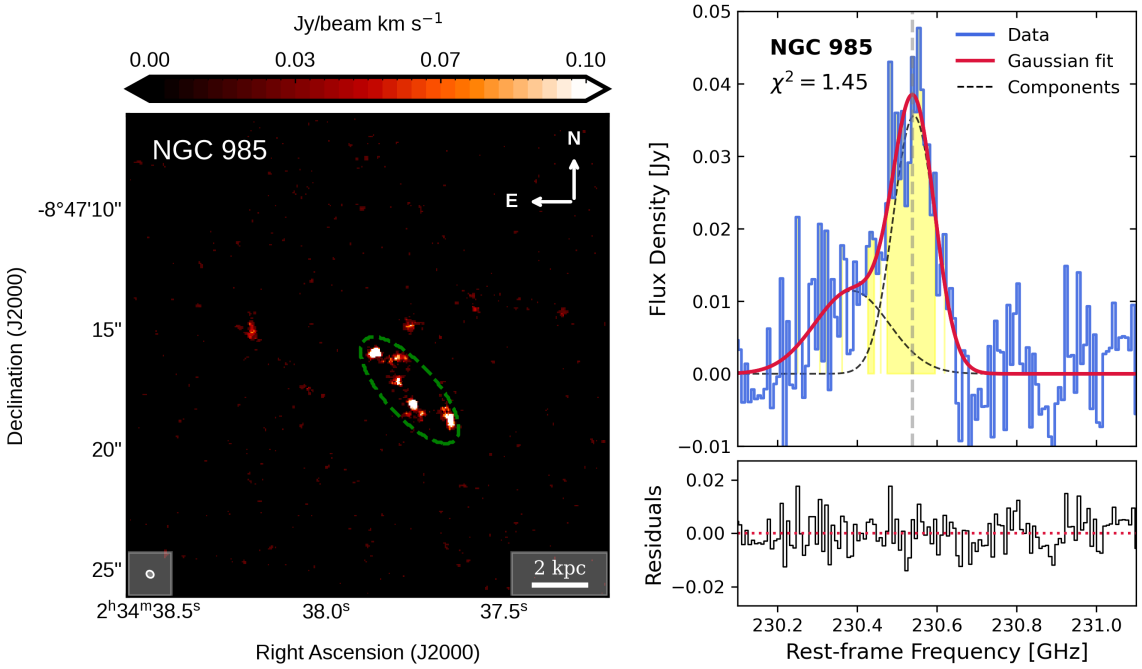


Figure 7.5: Same as 7.1 but for NGC 985.

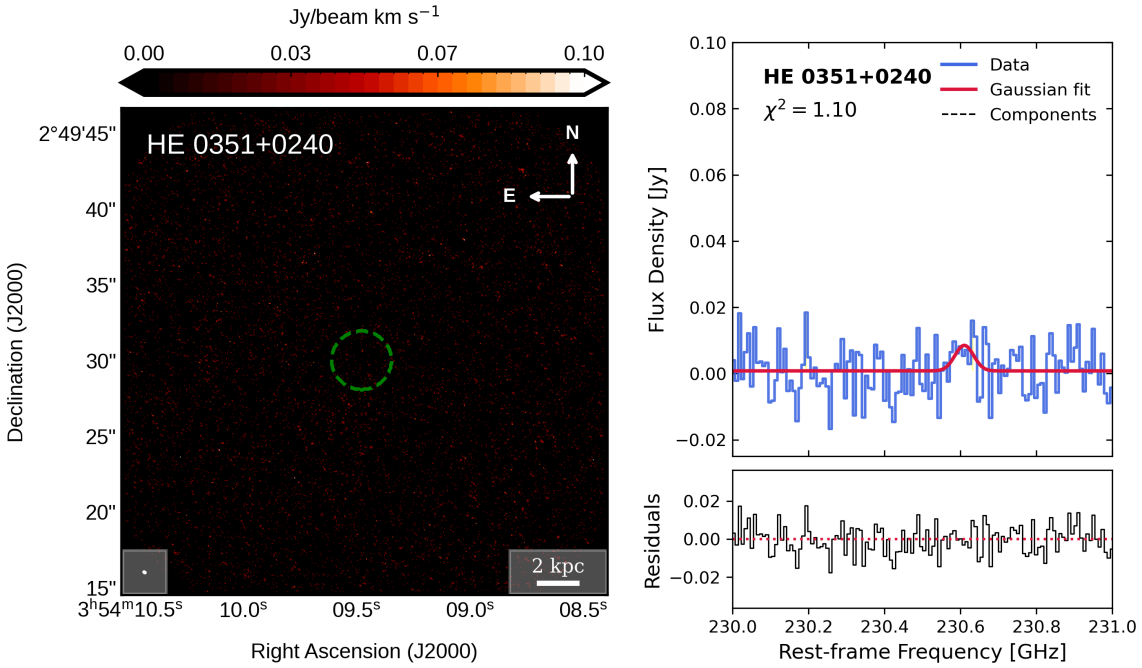


Figure 7.6: Same as 7.1 but for HE 0351+0240.

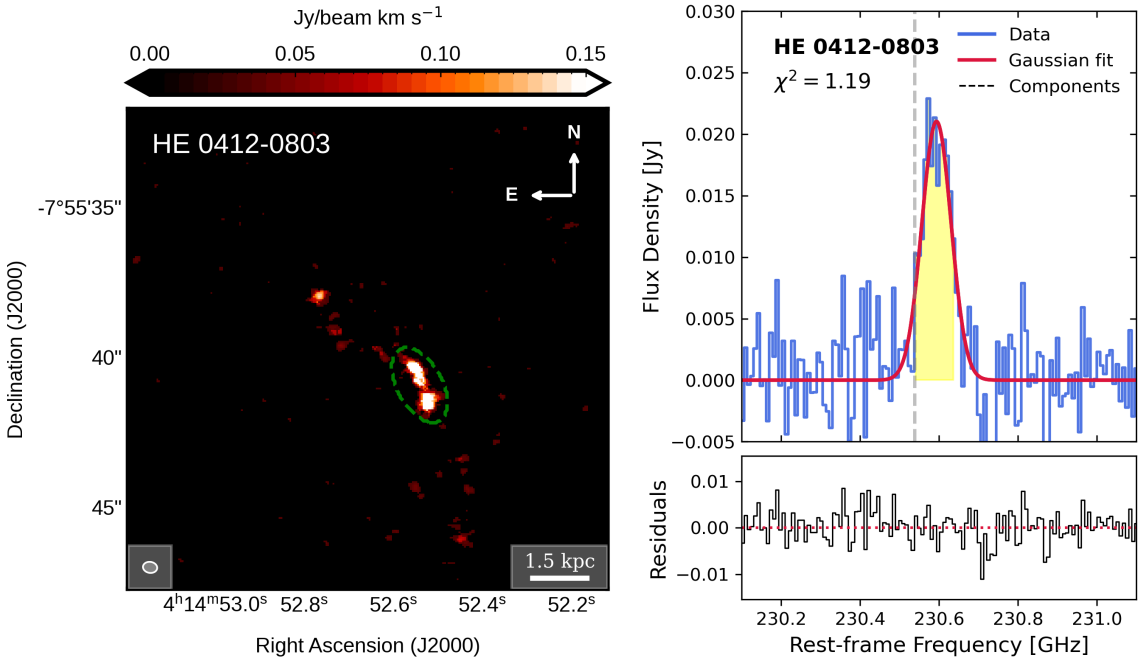


Figure 7.7: Same as 7.1 but for HE 0412-0803.

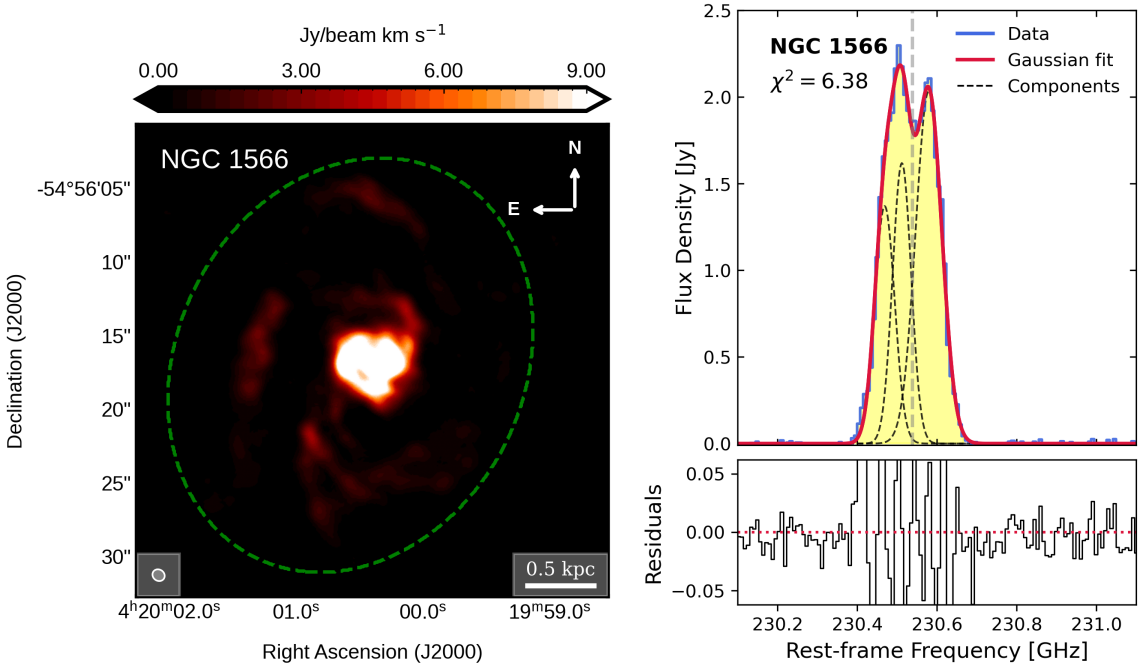


Figure 7.8: Same as 7.1 but for NGC 1566.

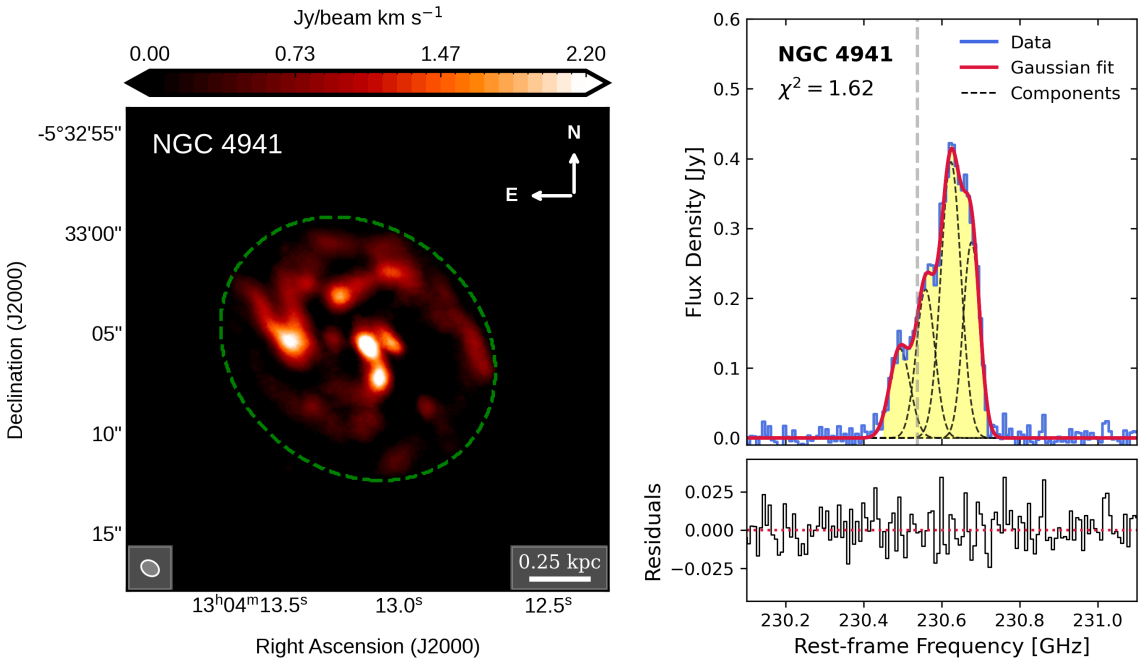


Figure 7.9: Same as 7.1 but for NGC 4941.

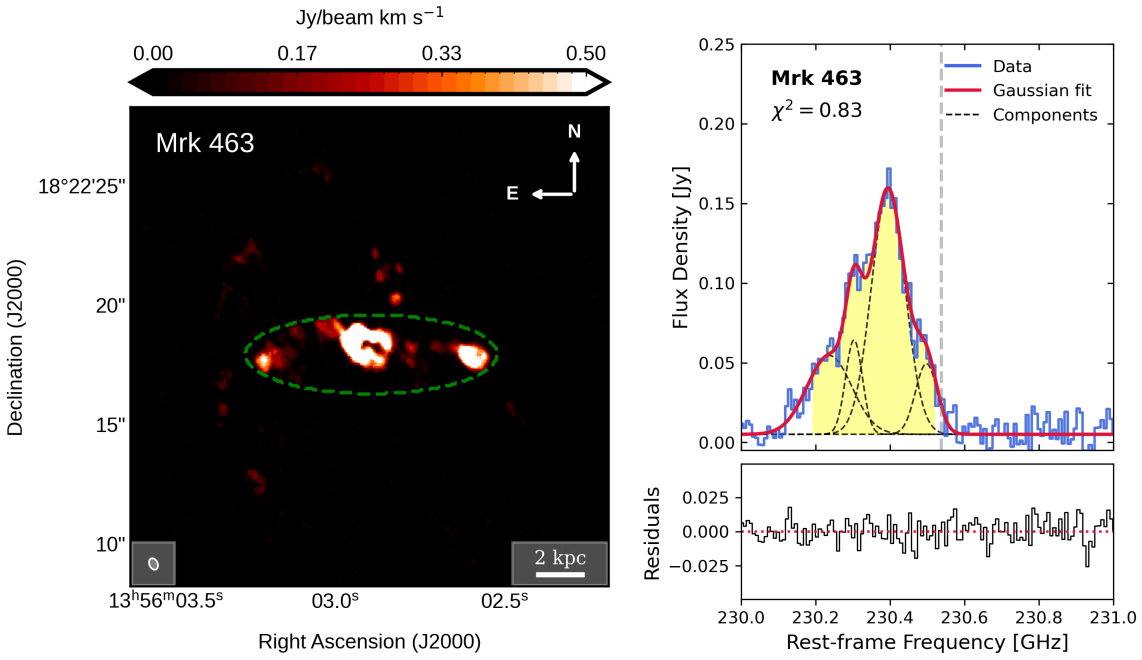


Figure 7.10: Same as 7.1 but for Mrk 463.

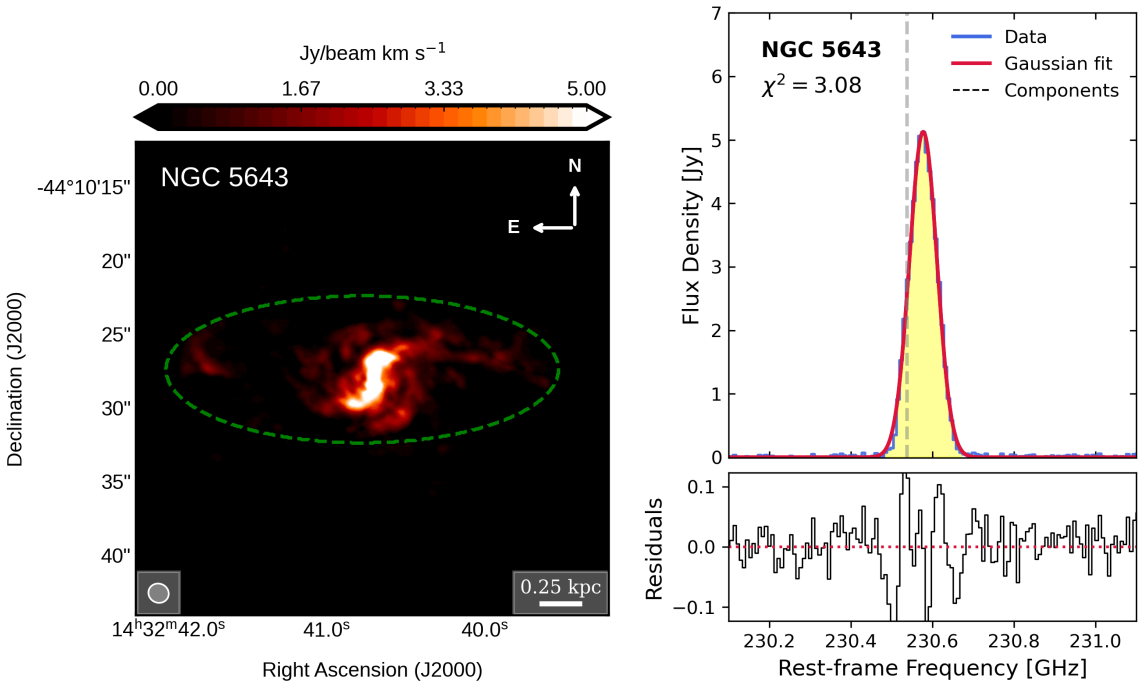


Figure 7.11: Same as 7.1 but for NGC 5643.

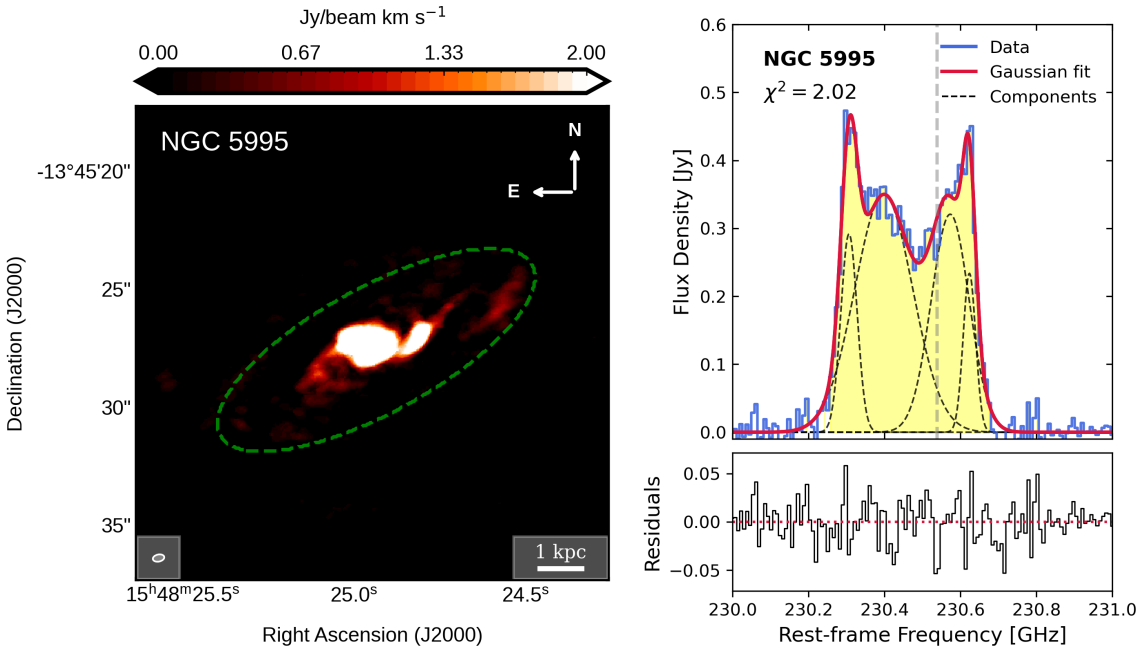


Figure 7.12: Same as 7.1 but for NGC 5995.

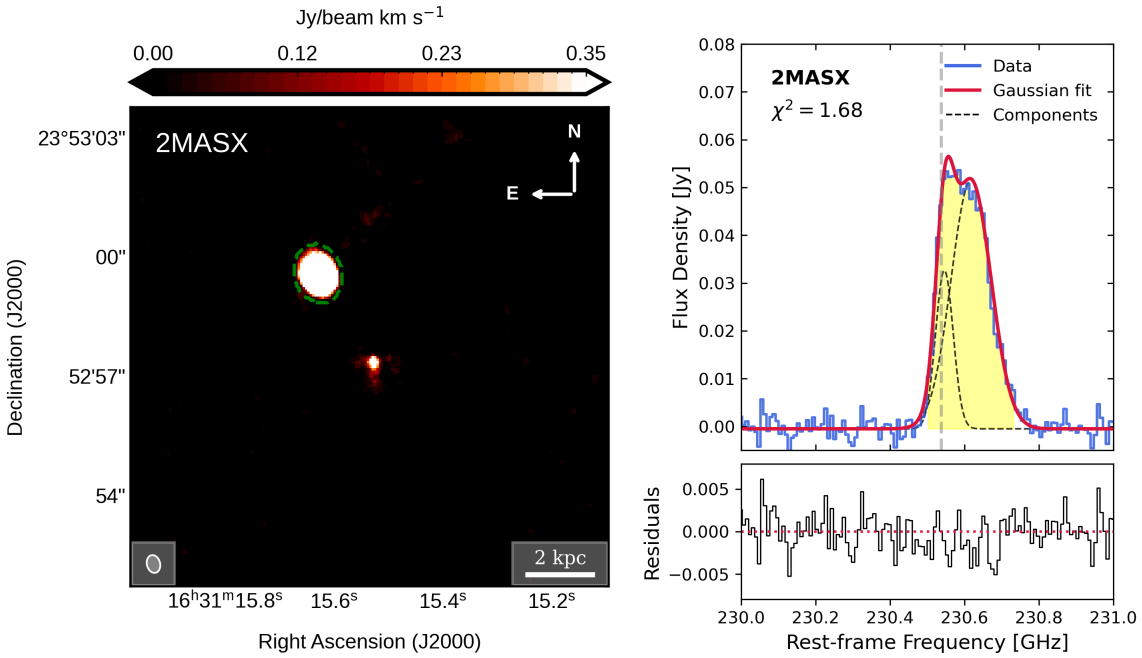


Figure 7.13: Same as 7.1 but for 2MASX 1631+2352.

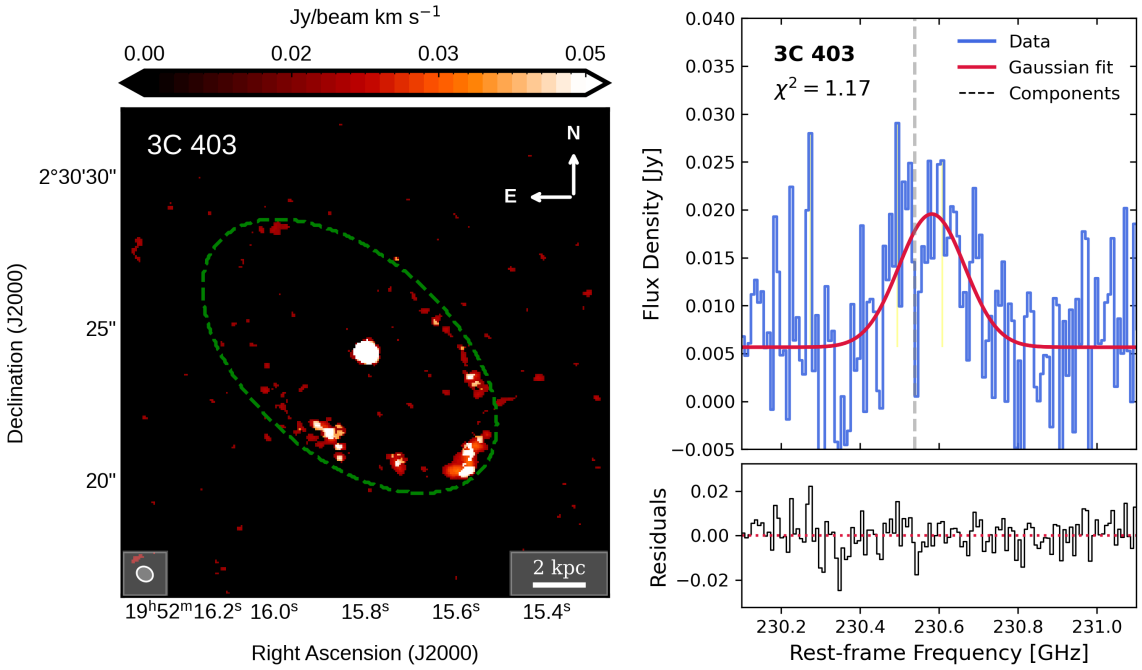


Figure 7.14: Same as 7.1 but for 3C 403.

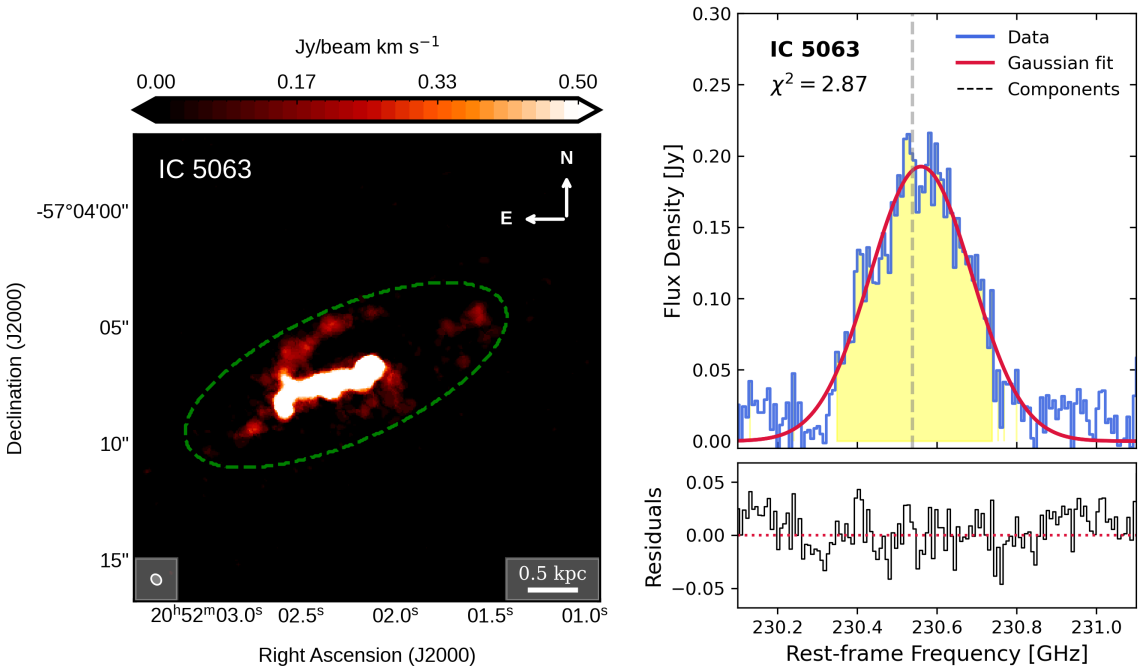


Figure 7.15: Same as 7.1 but for IC 5063.

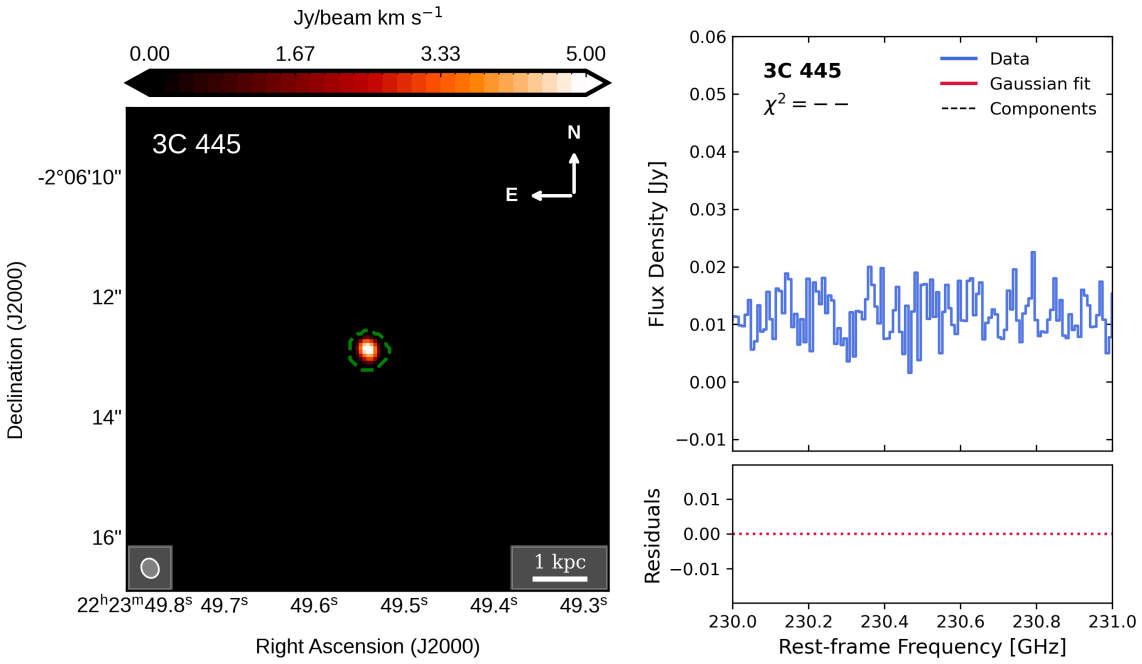


Figure 7.16: Same as 7.1 but for 3C 445.

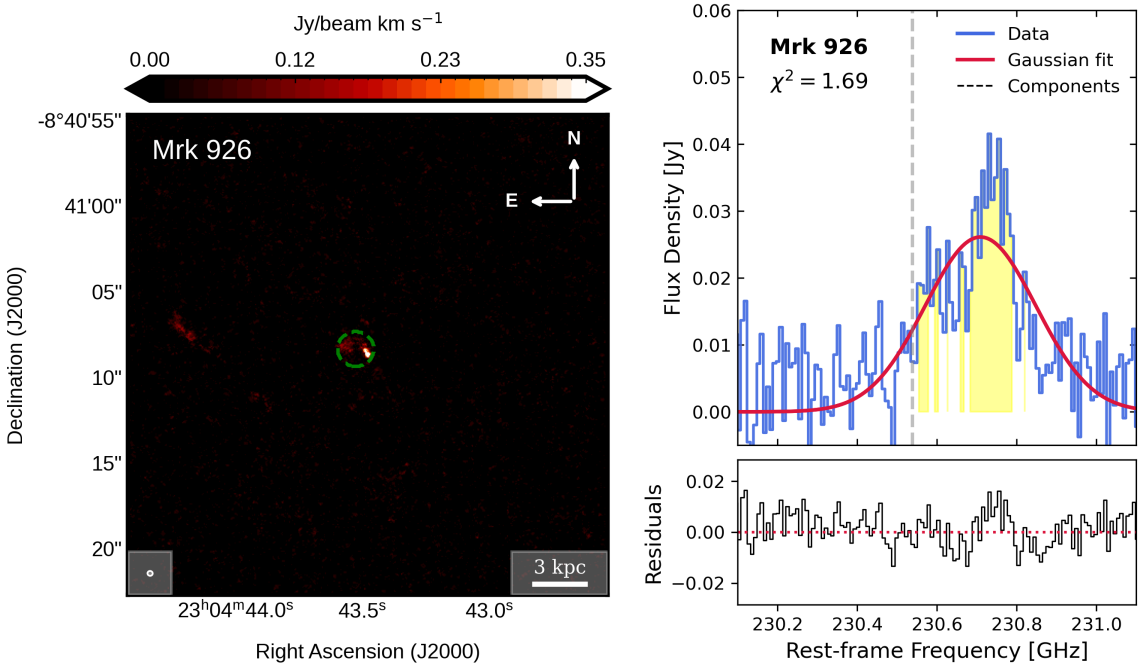


Figure 7.17: Same as 7.1 but for Mrk 926.

Chapter 8

Appendix B: Moment Maps

In this appendix, we present the full set of ALMA CO$(2-1)$ moment maps for the galaxy sample. Figure 8.1 through 8.7 display the integrated intensity (Moment 0), intensity-weighted mean velocity (Moment 1), and velocity dispersion (Moment 2) maps for each source, generated using the masking techniques outlined in Section 4.2.

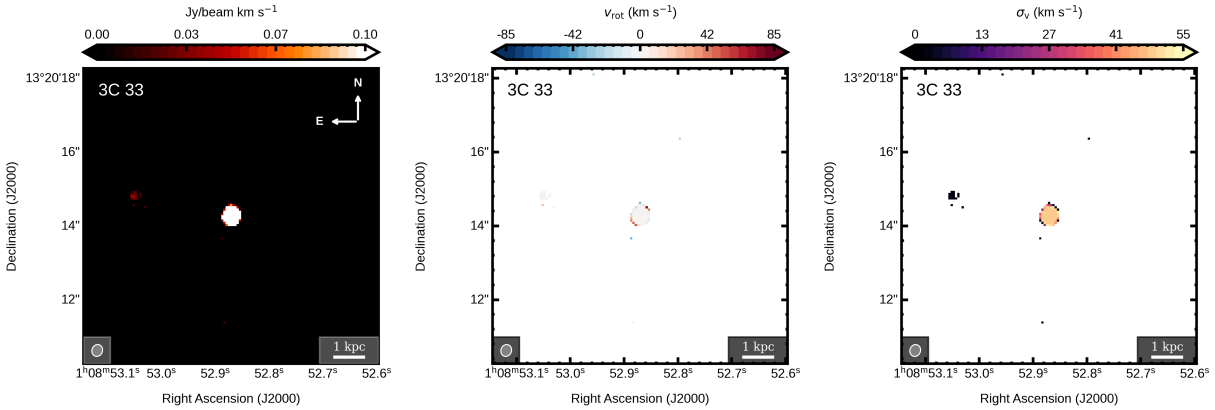


Figure 8.1: Moment maps for the ALMA CO$(2-1)$ galaxy sample. *Left panel*: Integrated intensity map (Moment 0). *Middle panel*: Intensity-weighted mean velocity field (Moment 1). *Right panel*: Velocity dispersion map (Moment 2). Synthesized beam is found in the bottom-left corner, the scale is located at the bottom-right corner and the arrows on the top-right corner indicate North and East.

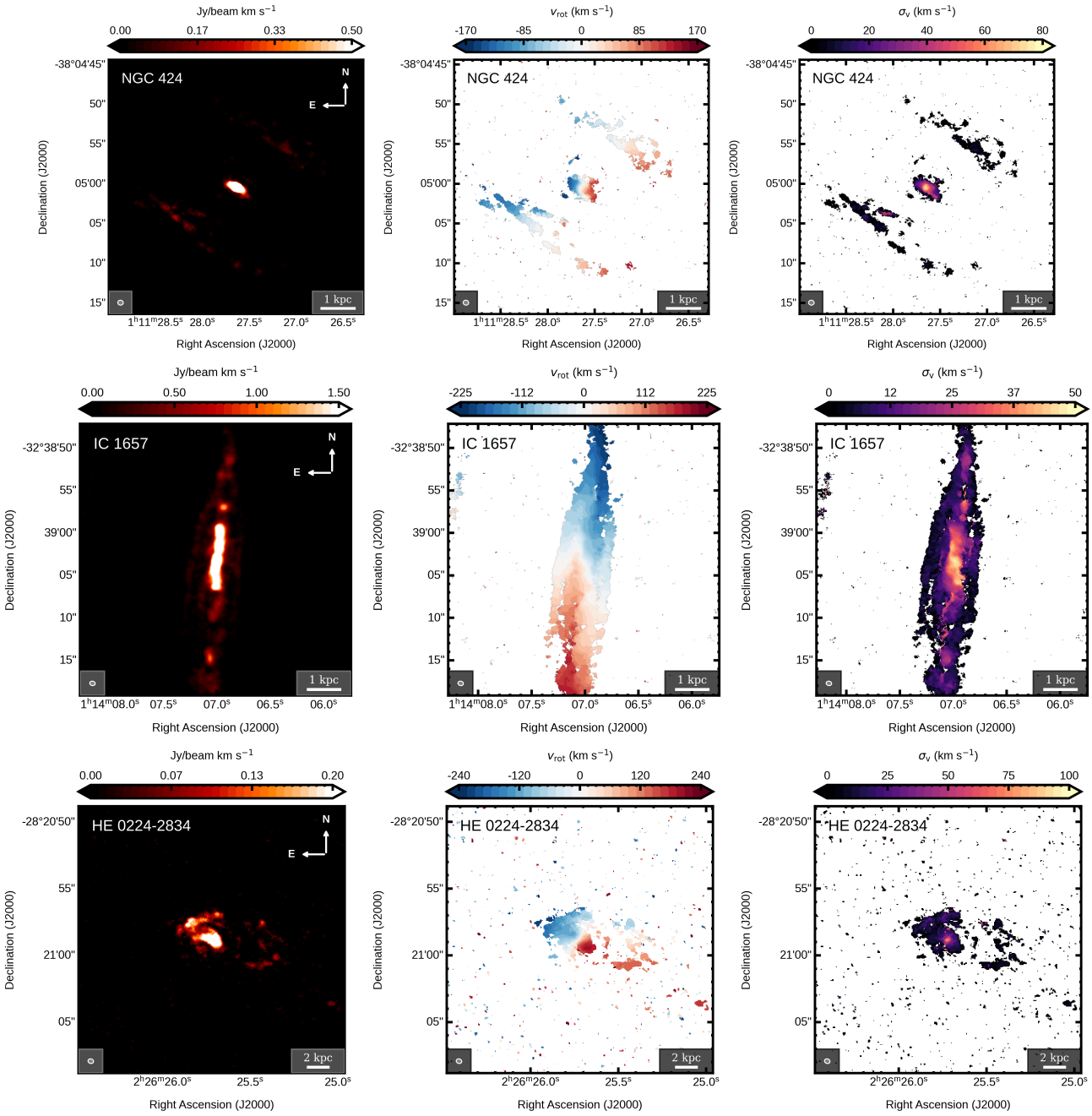


Figure 8.2: Continued.

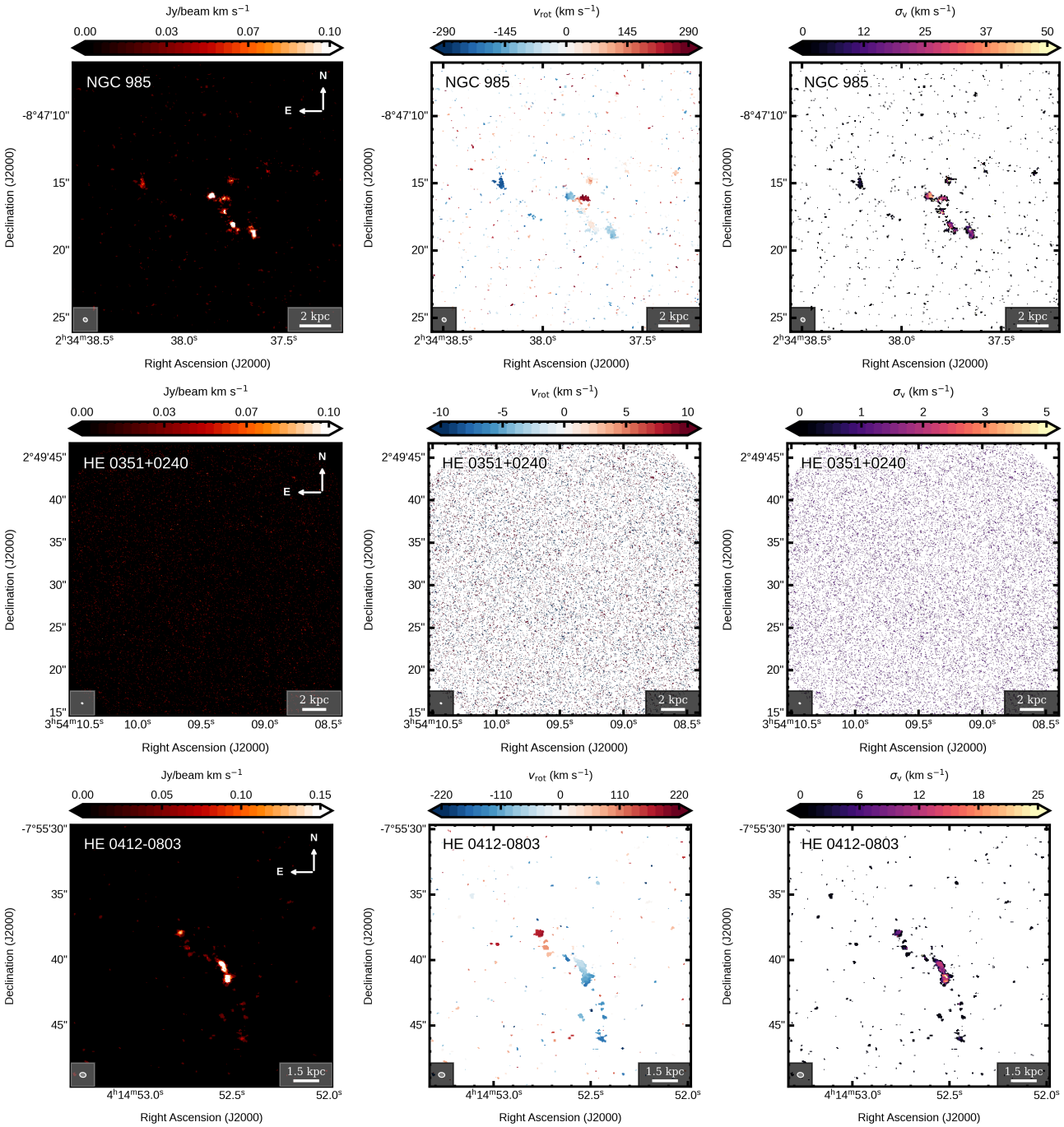


Figure 8.3: Continued.

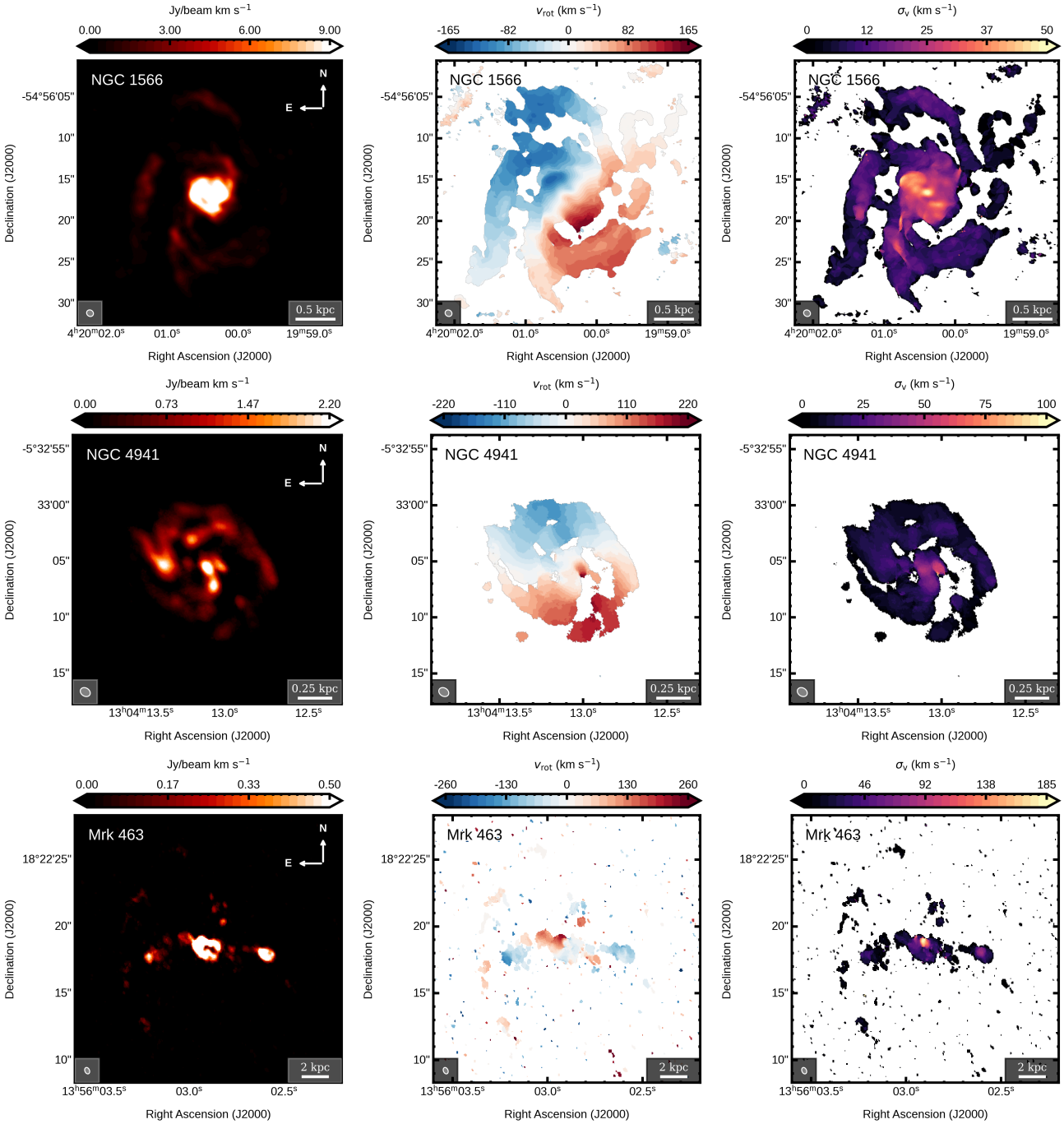


Figure 8.4: Continued.

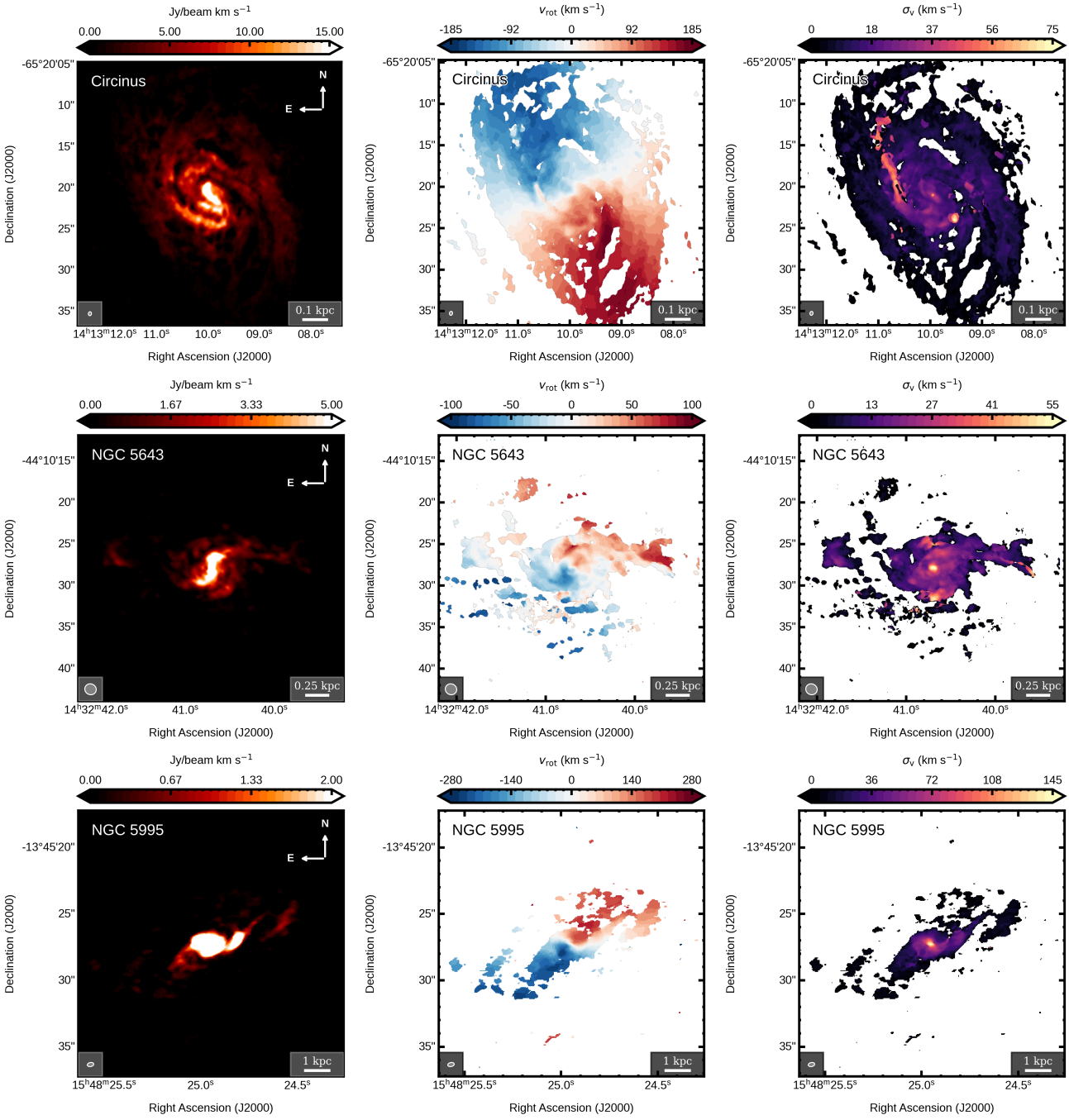


Figure 8.5: Continued.

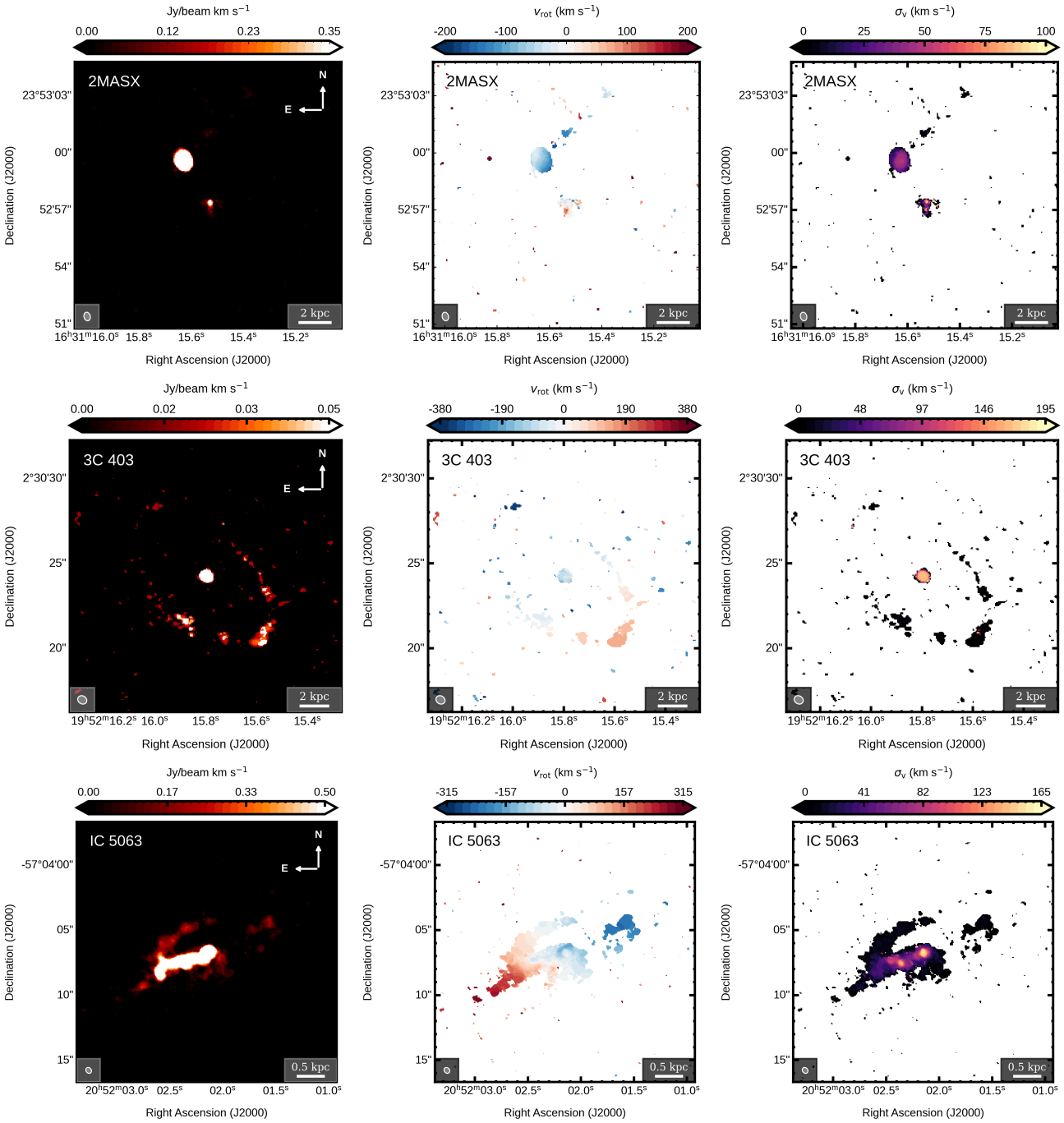


Figure 8.6: Continued.

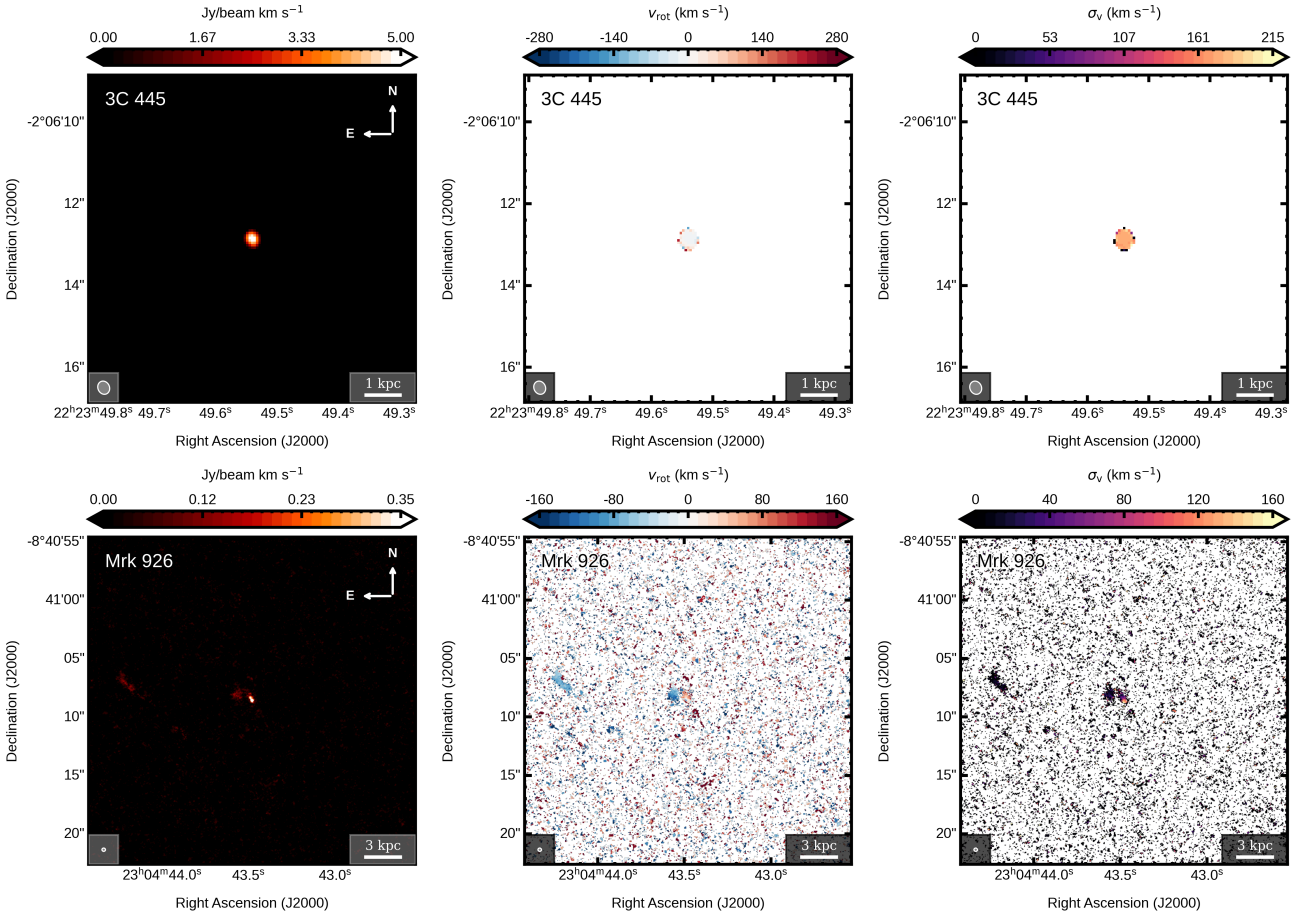


Figure 8.7: Continued.

Chapter 9

Appendix C: Radial Profiles

In this appendix, we present the radial profiles extracted from ALMA CO(2−1) moment 0 maps for the galaxies in our sample. Radial curves were extracted using concentric elliptical rings centered on the AGN, as explained in Section 3.1.3.

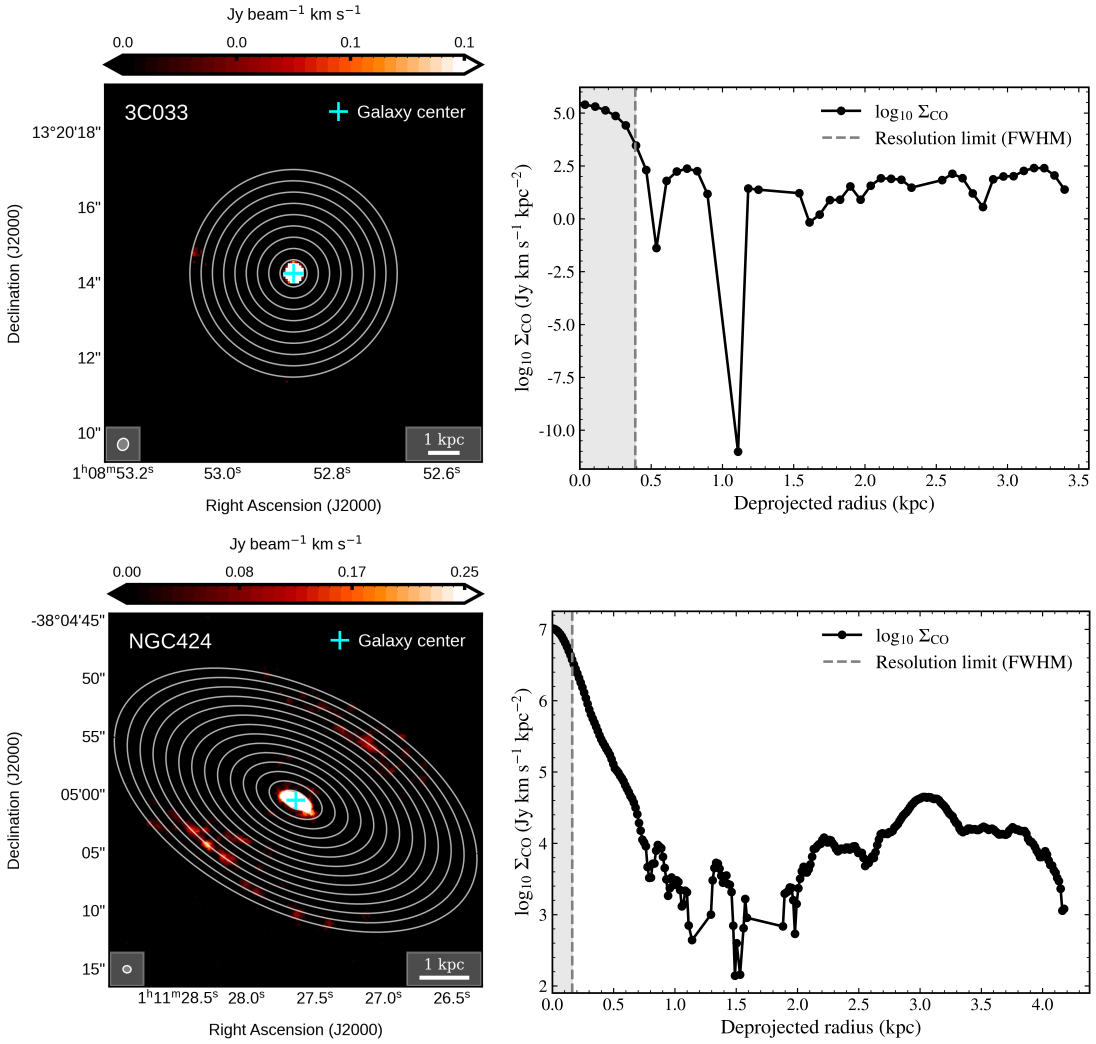


Figure 9.1: Radial profiles for the ALMA CO$(2-1)$ galaxy sample. *Left panel*: Annuli used for the radial profile in the zeroth moment, fixed at the center of the AGN. The cyan cross indicated the AGN position, while the white annuli represent the distribution and extent of the rings that measure $\Sigma_{\mathrm{CO(2\text{-}1)}}$. Synthesized beam is found in the bottom-left corner, the scale is located at the bottom-right corner. *Right panel*: Radial surface brightness distribution across the galaxy in logarithmic scale, where each black point dictates the surface brightness measure of one ring. The gray area beyond the dotted line represents the area that is unresolved, as the major axis of the beam is bigger than the annuli in this region.

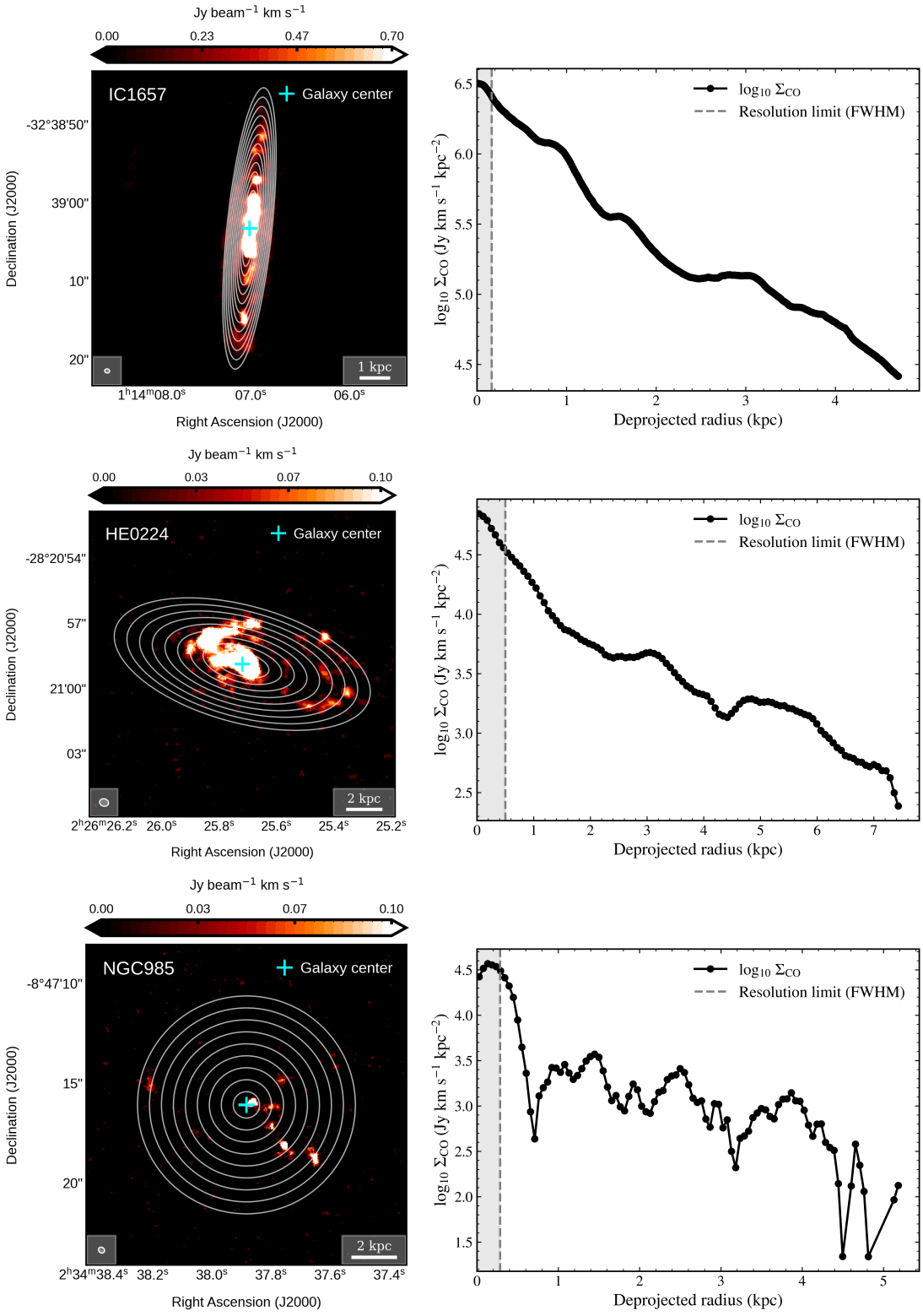


Figure 9.2: Continued.

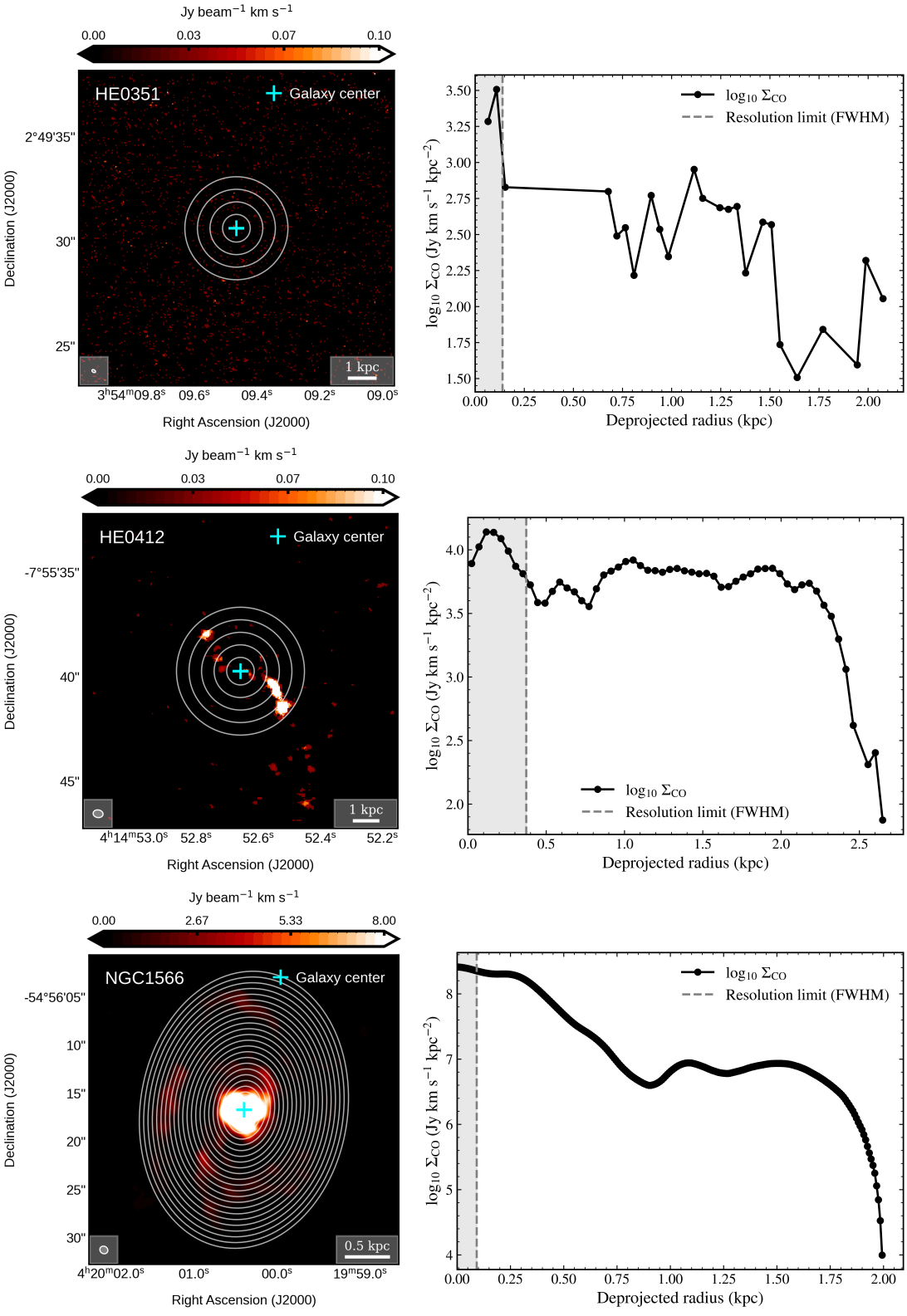


Figure 9.3: Continued.

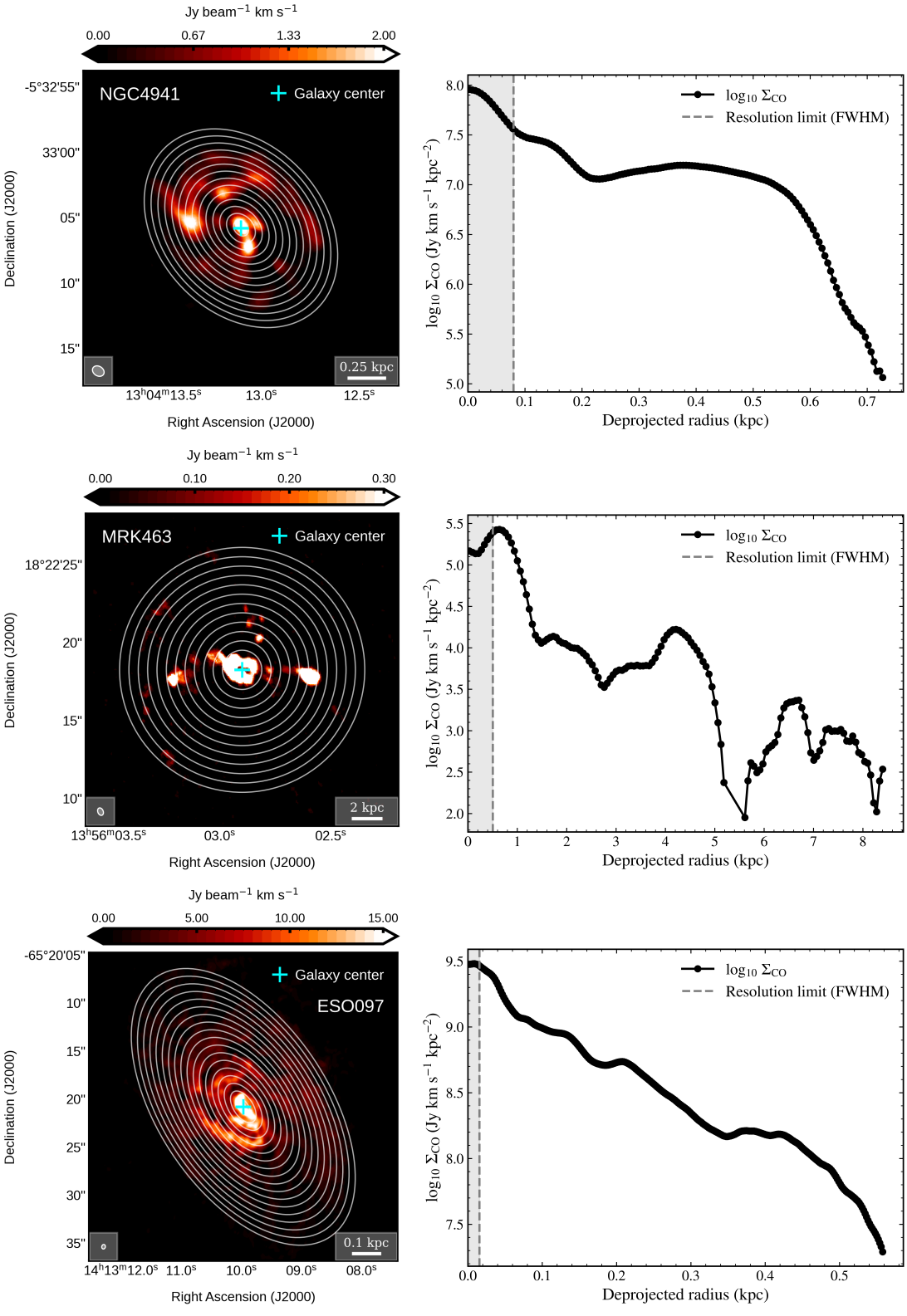


Figure 9.4: Continued.

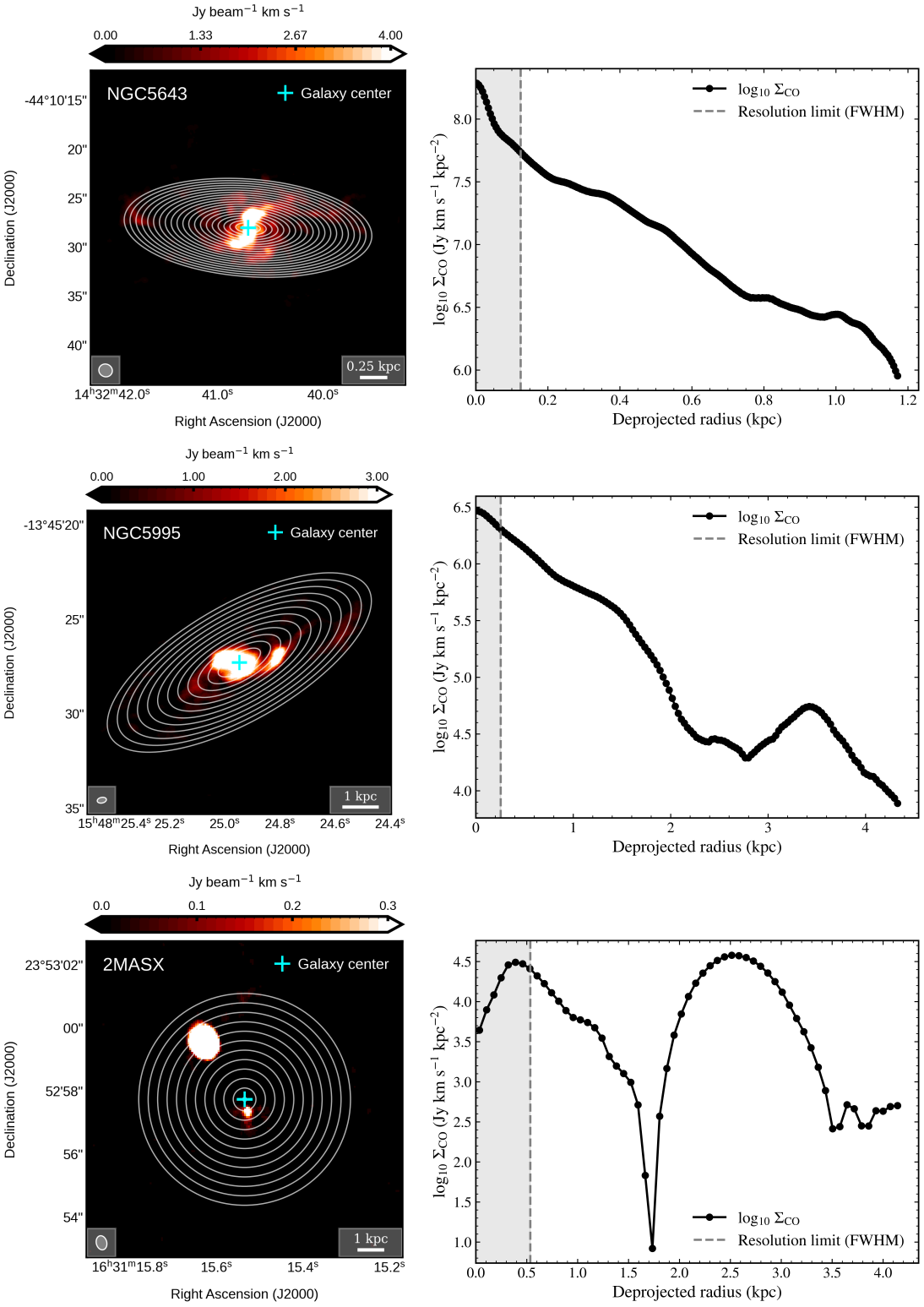


Figure 9.5: Continued.

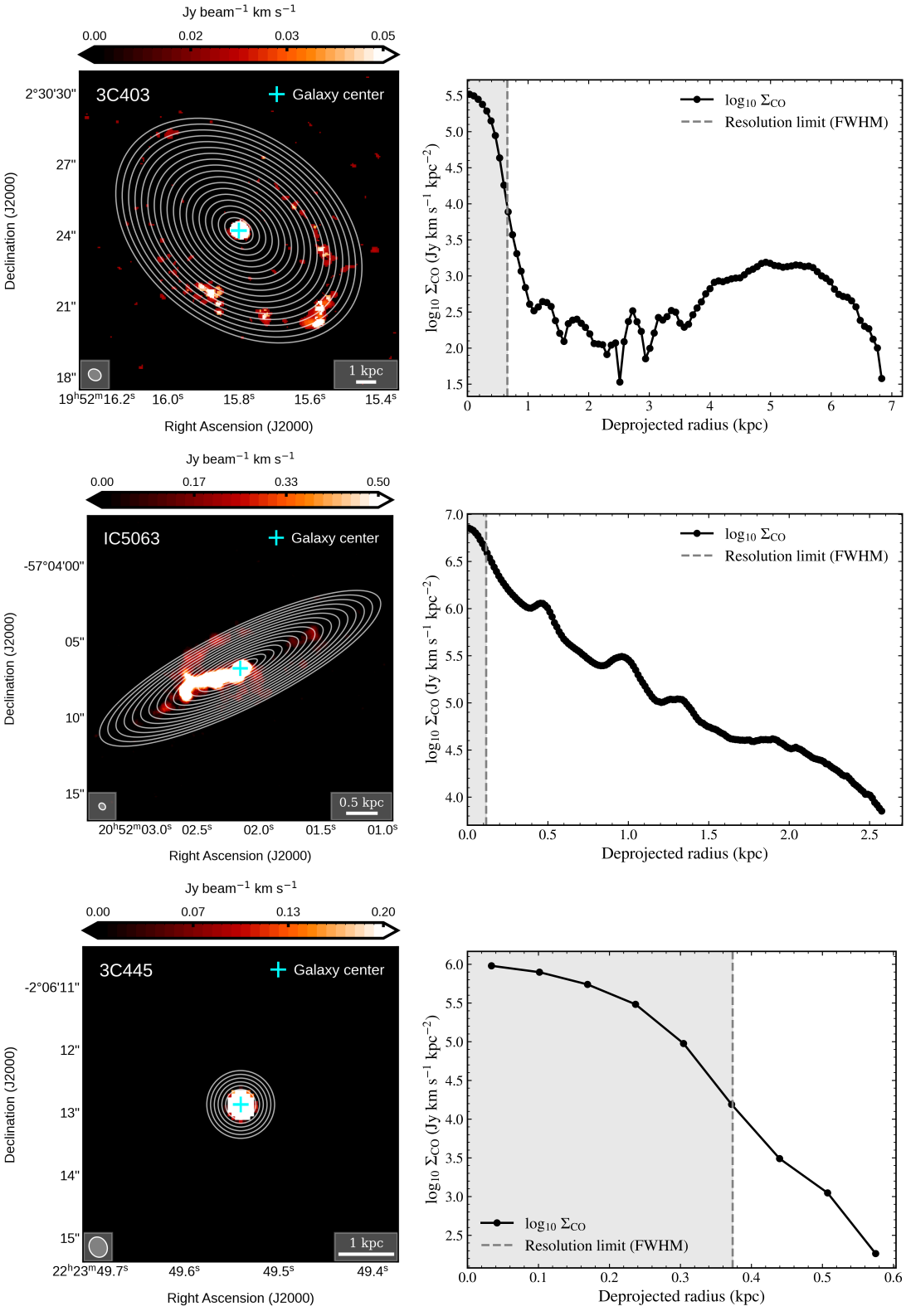


Figure 9.6: Continued.

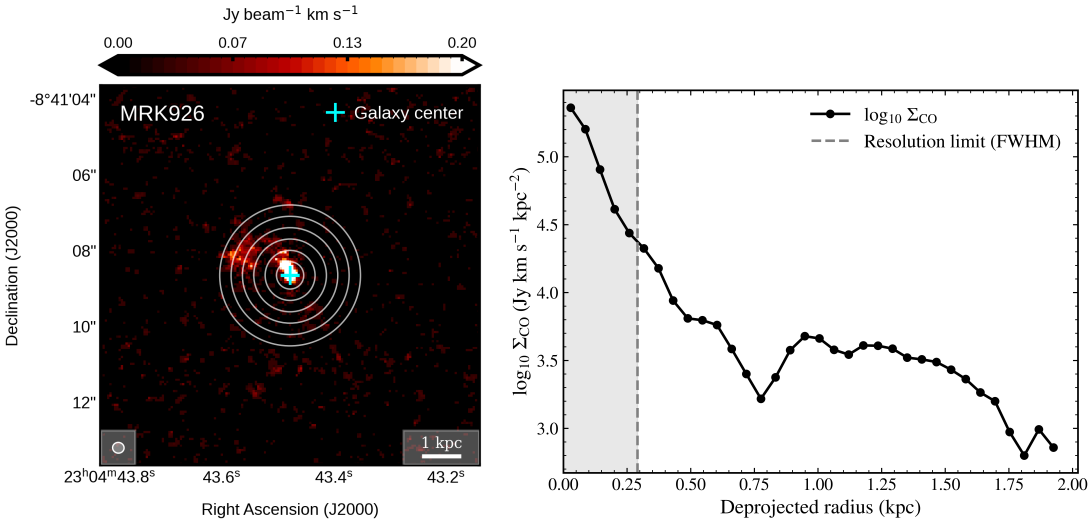


Figure 9.7: Continued.

Chapter 10

Appendix D: Radio continuum observations with VLA and correlation with CO(2 – 1) ALMA observations

In this appendix, we present the moment 0 ALMA CO(2 – 1) maps overlaid with high-resolution VLA radio continuum emission. Contour levels start at 3σ, increasing to 4σ, 8σ, 16σ, 32σ, 64σ, 128σ and 256σ. Negative contours are dismissed.

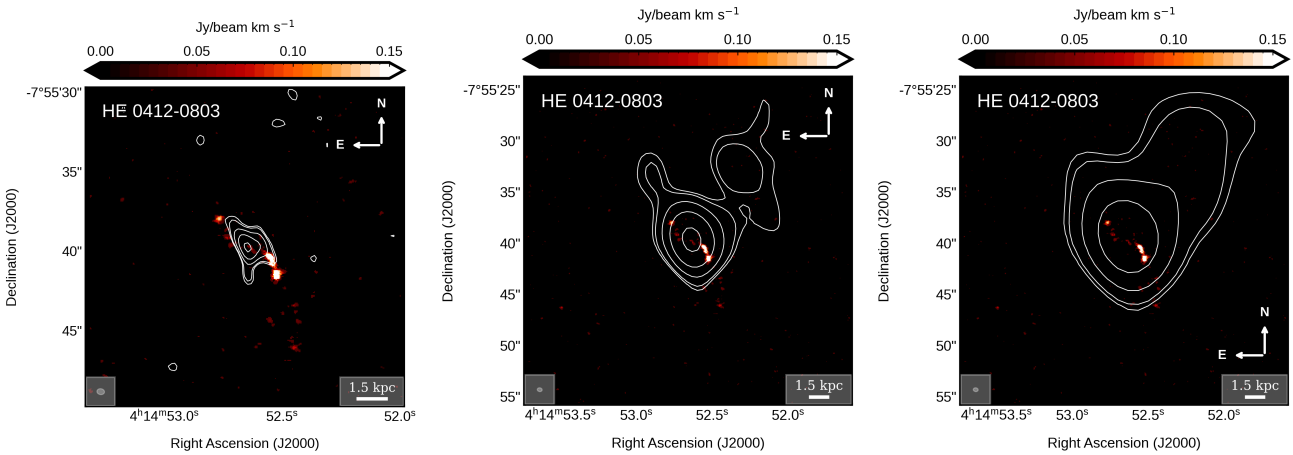


Figure 10.1: ALMA CO(2 – 1) integrated intensity map (color) with 22 GHz VLA C configuration radio continuum contours (white) of HE 0412-0803. Contours were drawn at 3σ, 4σ, 8σ, 16σ, 32σ, 64σ, 128σ and 256σ. *Left panel*: 1" aperture VLA observation. *Middle panel*: 3" aperture VLA observation. *Right panel*: 6" aperture VLA observation. Synthesized beam is found in the bottom-left corner, the scale is located at the bottom-right corner and the arrows on the top-right corner indicate North and East.

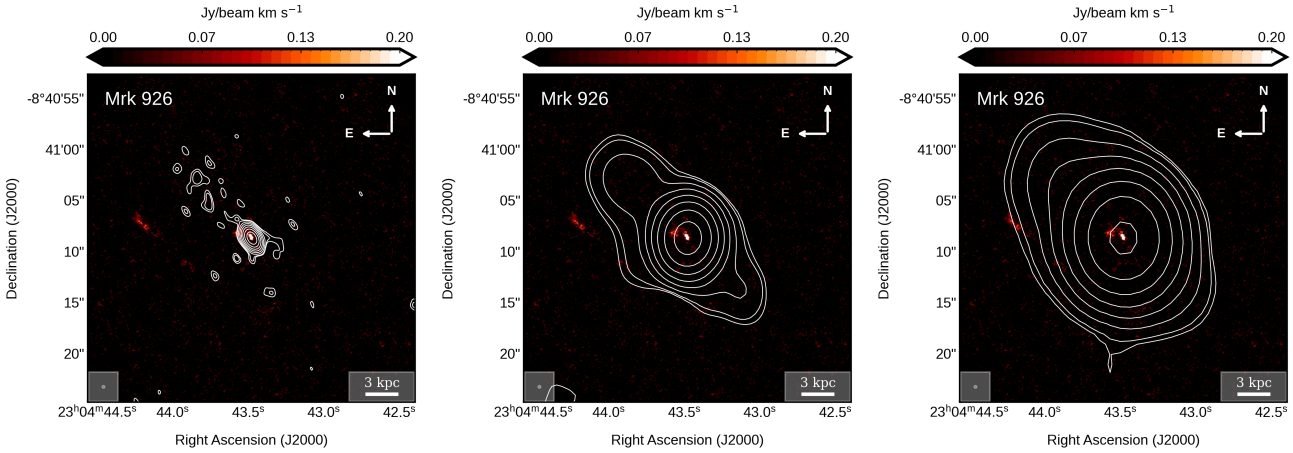


Figure 10.2: Same as Fig. 10.1 for Mrk 926.

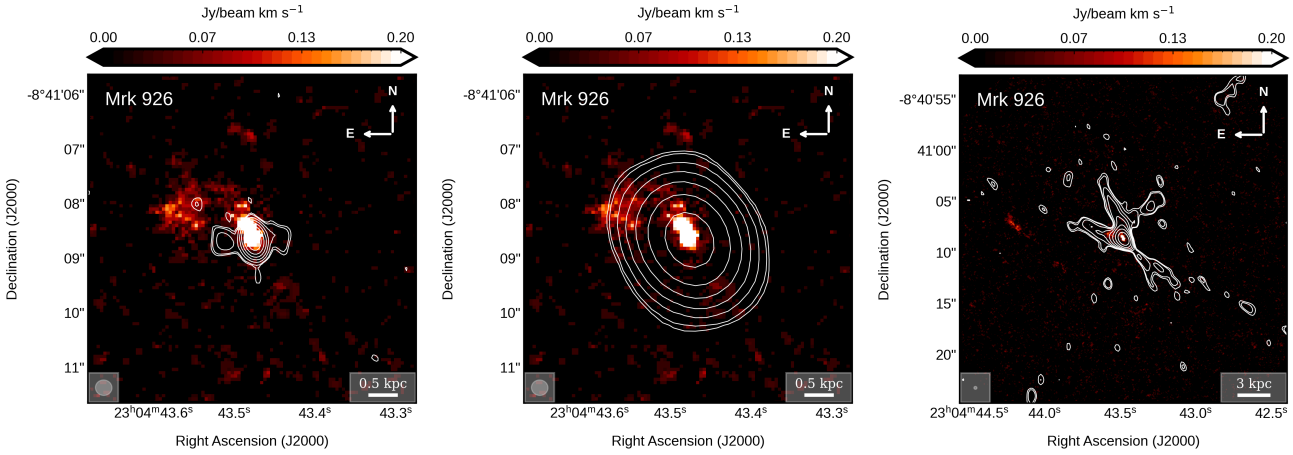


Figure 10.3: Same as Fig. 10.1 for Mrk 926 in the B Array of the VLA, starting at 0.3" aperture (Left panel), and an extended field of view observation (Right panel).

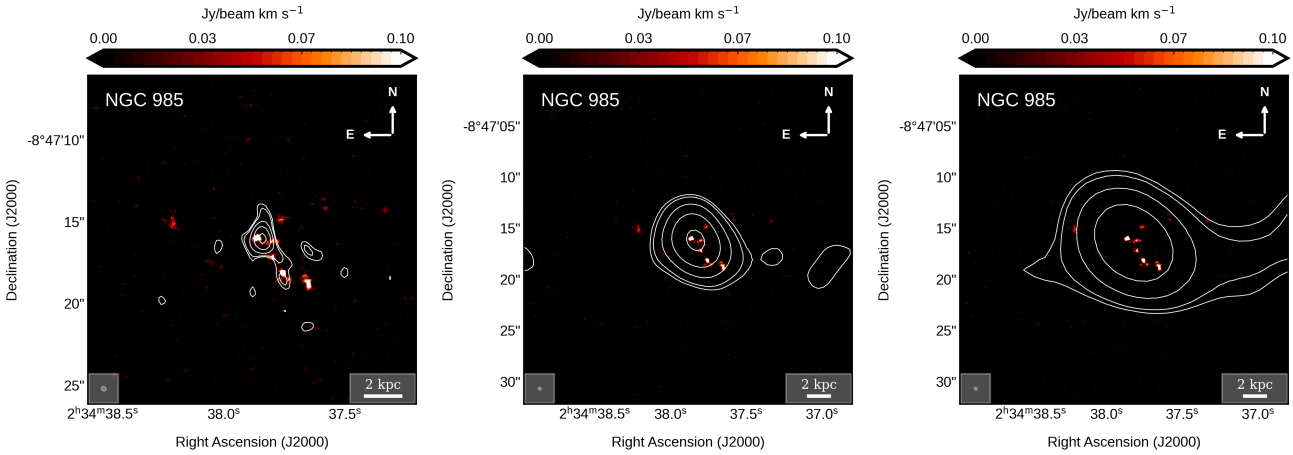


Figure 10.4: Same as Fig. 10.1 for NGC 424.

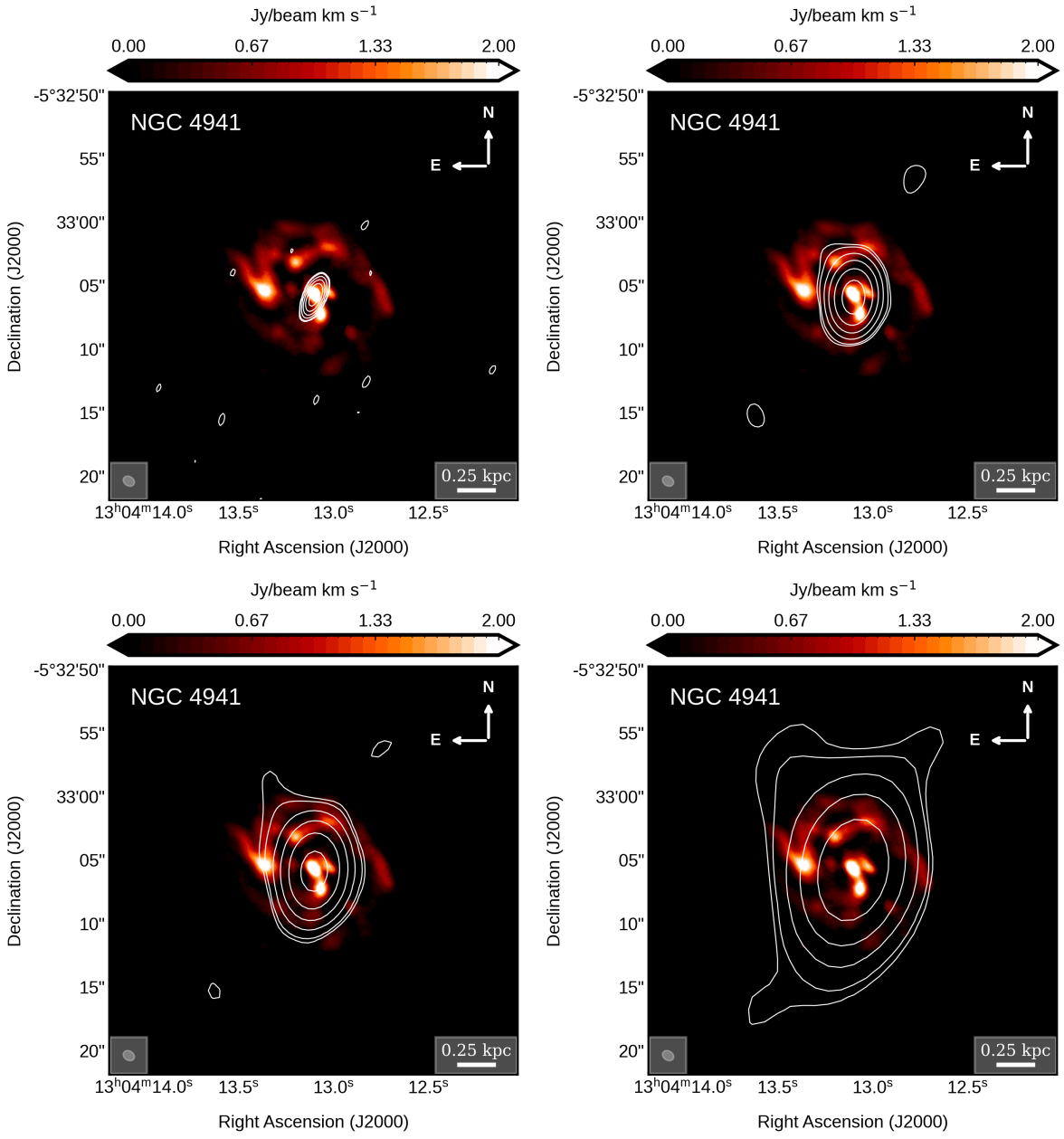


Figure 10.5: Same as Fig. 10.1 for NGC 4941, with the addition of the observation in the 2" aperture.

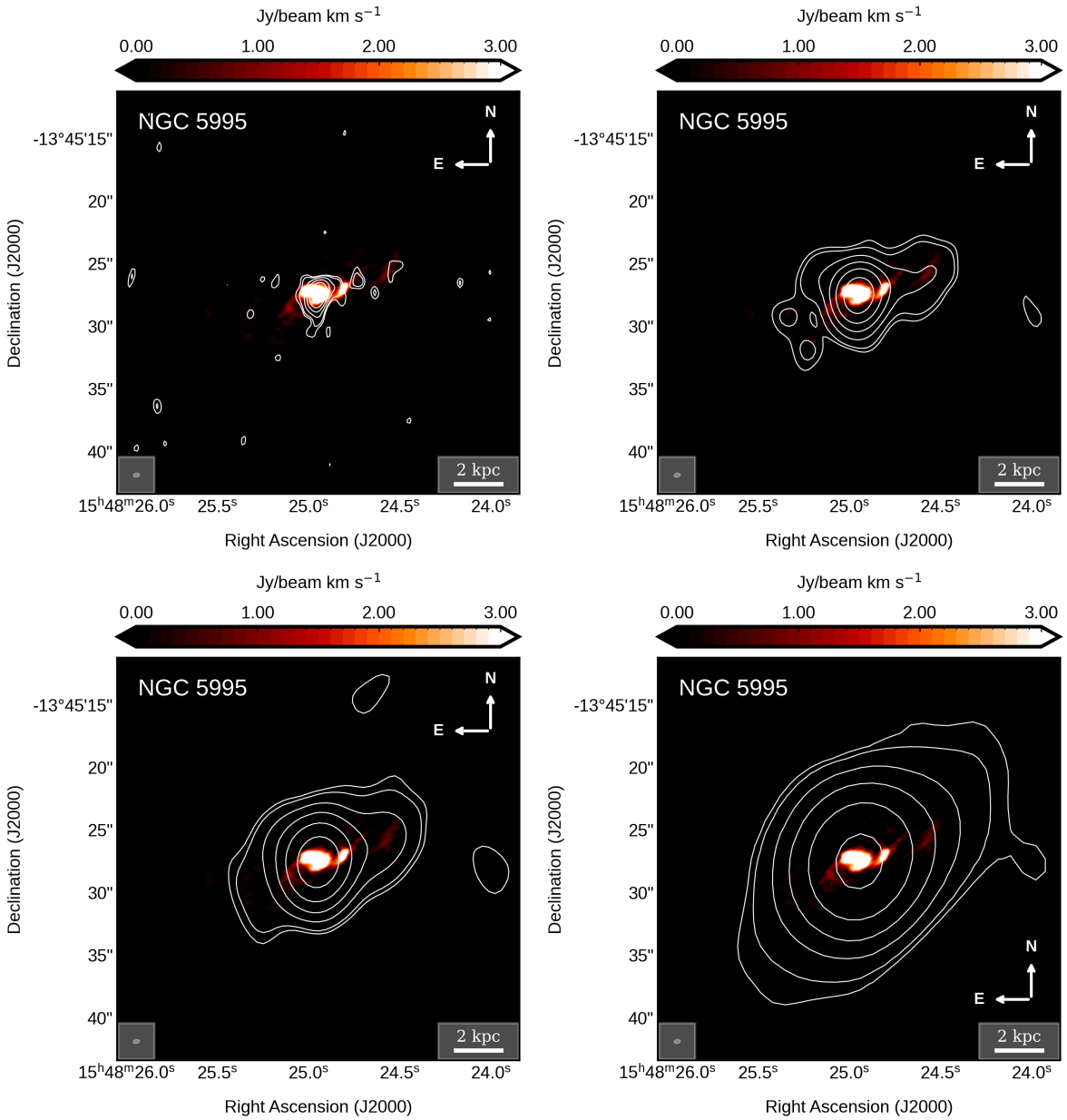


Figure 10.6: Same as Fig. 10.1 for NGC 5995, with the addition of the observation in the 2" aperture.

Chapter 11

Appendix E: ^{3D}BBarolo Modeling Results

In this appendix, we present the 3D tilted-ring kinematic modeling results derived using ^{3D}BBarolo (Di Teodoro & Fraternali, 2015) for the selected galaxy sample. The modeling used ALMA CO(2−1) data cubes as input.

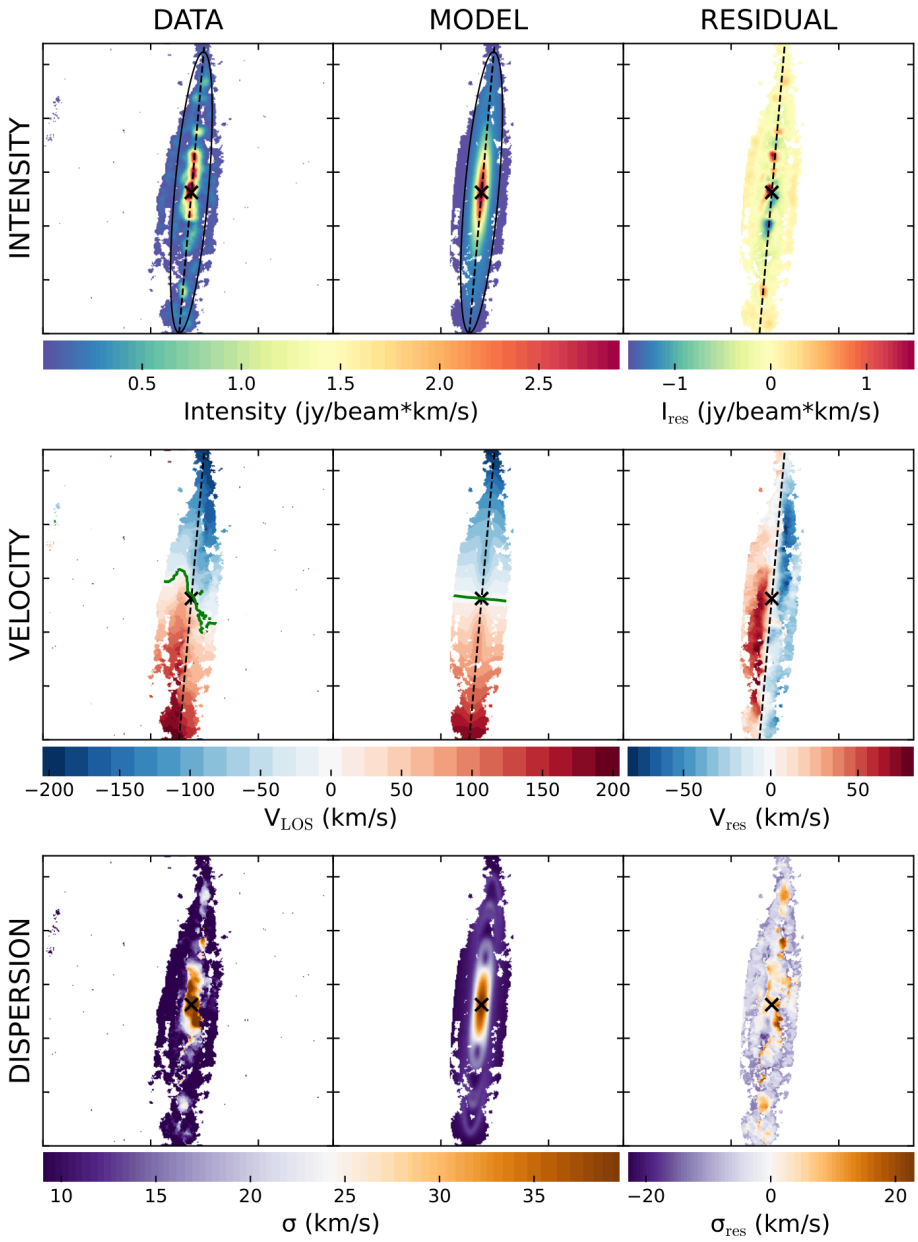


Figure 11.1: ALMA CO(2 − 1) kinematics model by ^{3D}BBarolo for IC 1657. *Left row (Data)*: Observed integrated intensity (Moment 0, top), intensity-weighted velocity field from the line of sight (Moment 1, middle) and velocity dispersion (Moment 2, bottom). *Middle Row (Model)*: Corresponding moment maps reconstructed from the best fitted tilted-ring model. *Right Row (Residuals)*: Residual maps showing the differences between the data and the model. The last ring modeled is shown as a solid black ring on moment 0 plots, with the dotted black line being the major axis of the outer ring.

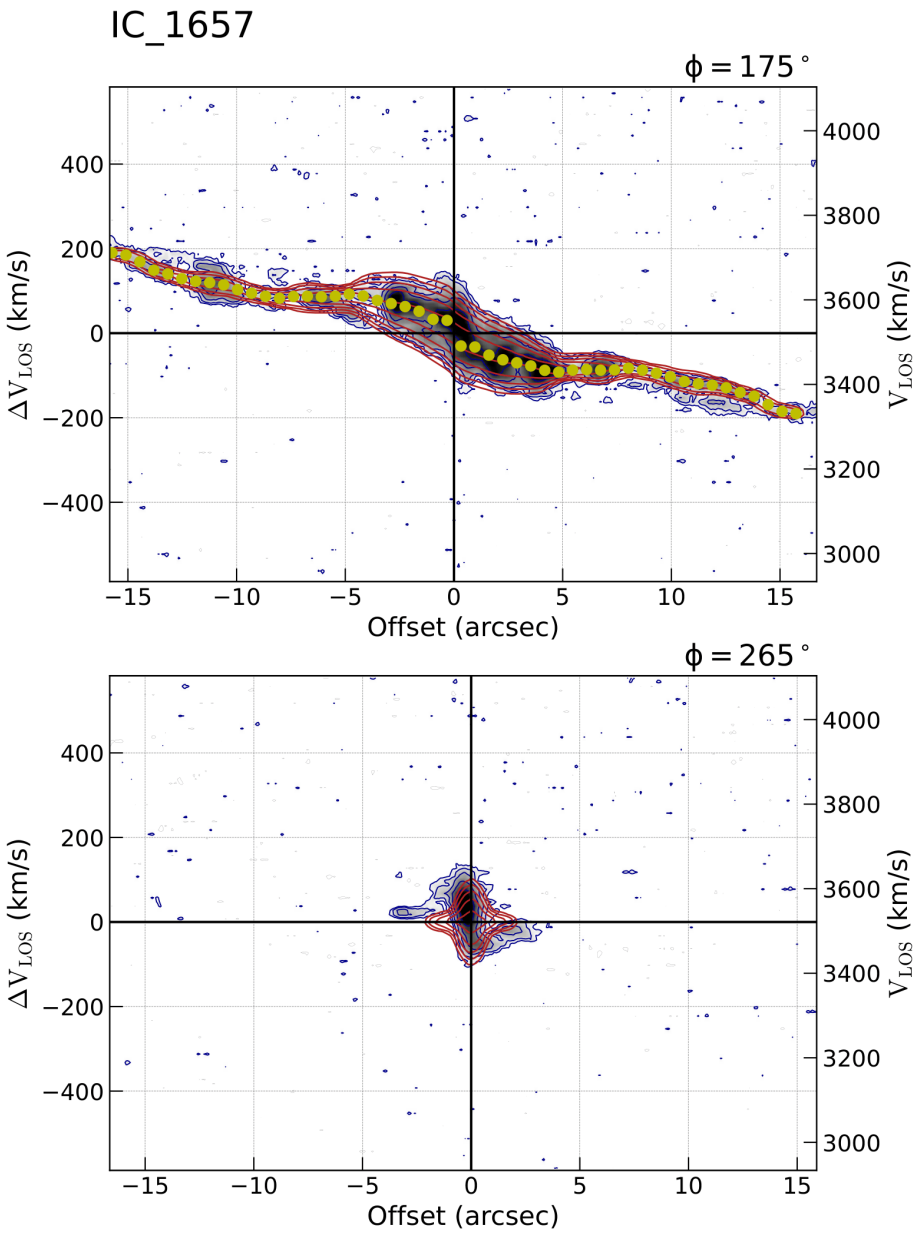


Figure 11.2: ALMA CO$(2-1)$ position-velocity (PV) diagram and PV model by ^{3D}BBarolo for IC 1657. The grayscale intensity background represents the observed data, where overlaid blue contours indicate positive line emission, whereas gray contours indicate negative noise levels. The ^{3D}BBarolo model is overlaid as red contours ($1\sigma, 2\sigma, 4\sigma, 8\sigma, 16\sigma, 32\sigma$ and 64σ) evaluated at the same flux levels as the data. The solid black line marks the spatial center and systemic velocity $V_{\rm sys}$ (corresponding to $\Delta V_{\rm LOS} = 0$ km s^{-1}). ϕ indicates the best-fit for the position angle (PA) of the kinematic axis in degrees. *Top panel*: Major axis PV diagram. Yellow dots indicate the ^{3D}BBarolo best-fit rotational velocity points projected at each ring. *Bottom panel*: Minor axis PV diagram.

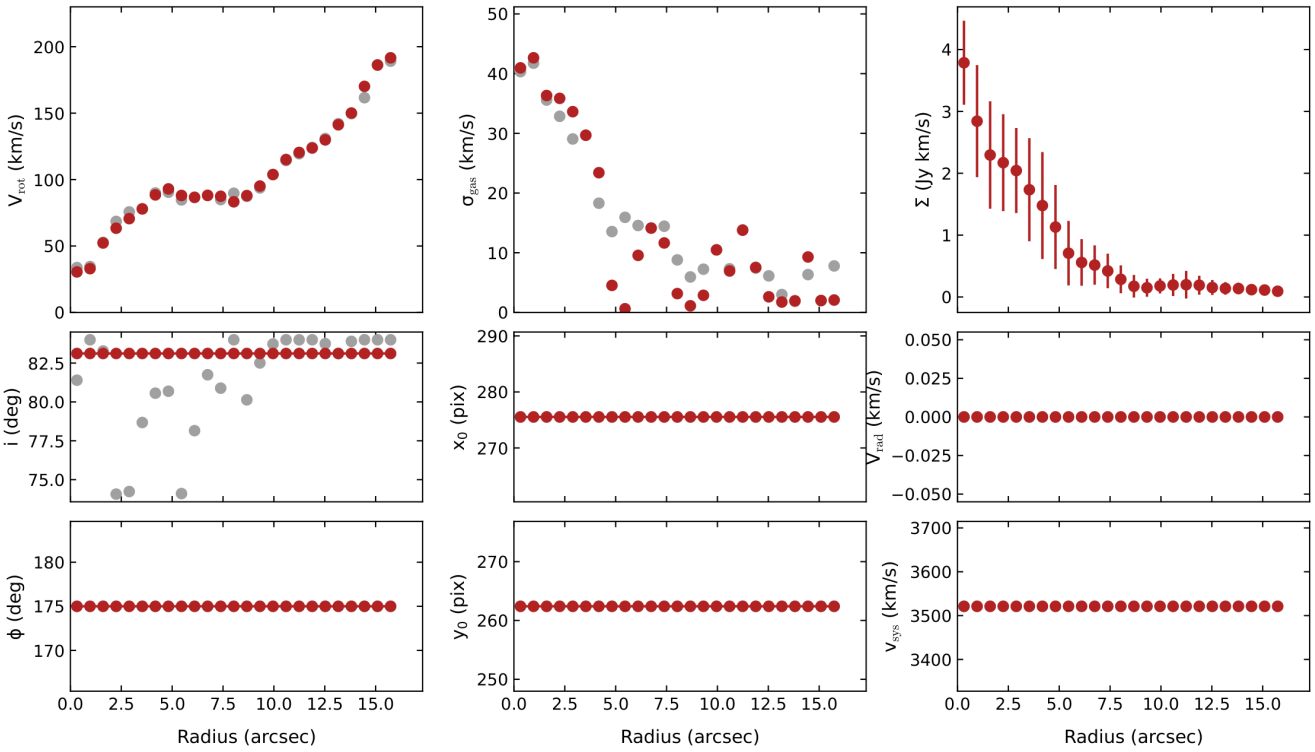


Figure 11.3: Best fitted parameters by ^{3D}BBarolo for IC 1657. Gray points represent the observed data, whereas red points represent the ^{3D}BBarolo fit. Each point corresponds to a ring in the fit. *Top-left panel*: Rotational velocity in km s^{-1}. *Top-middle panel*: Velocity dispersion in km s^{-1}. *Top-right panel*: Modeled CO$(2-1)$ brightness in Jy km s^{-1}. *Middle-left panel*: Inclination of each fitted ring in degrees. *Middle panel*: Central position of the AGN in the x axis in pixels. *Middle-right panel*: Radial velocity in km s^{-1}. This value is always fixed at zero. *Bottom-left panel*: Position Angle inclination (PA) in degrees. *Bottom-middle panel*: Central position of the AGN in the y axis in pixels. *Bottom-right panel*: Systemic velocity, automatically estimated by ^{3D}BBarolo.

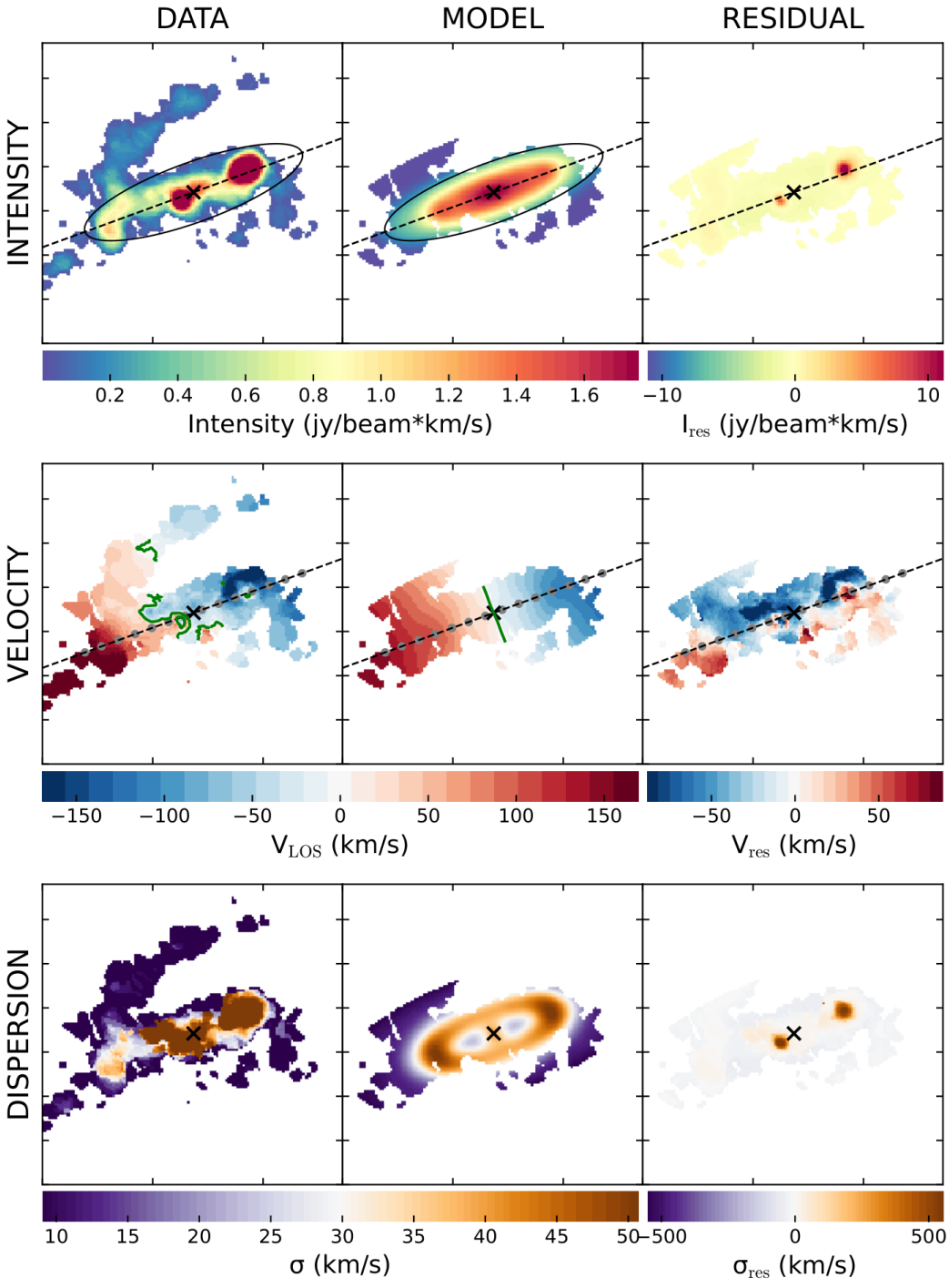


Figure 11.4: Same as 11.1 for IC 5063.

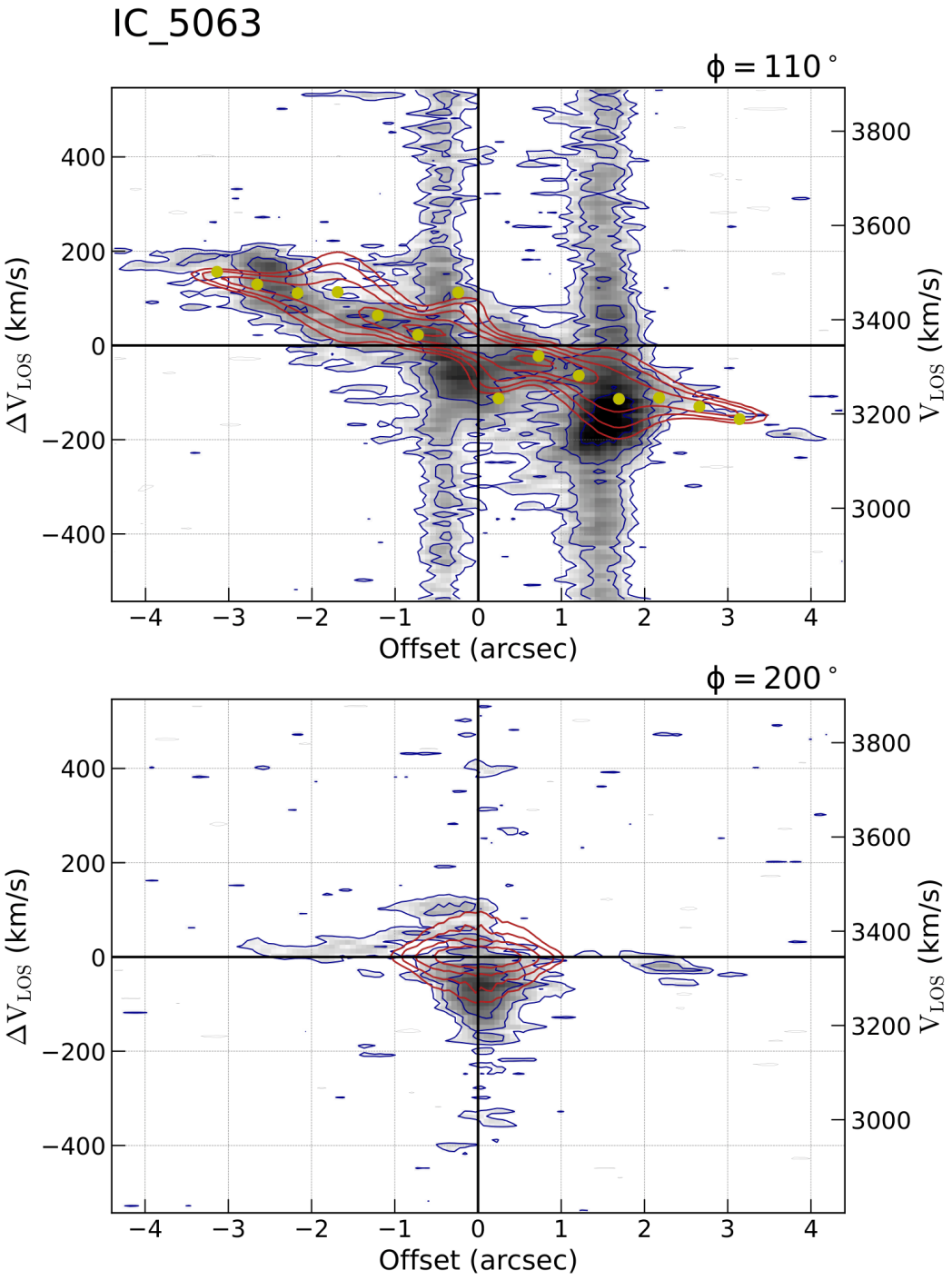


Figure 11.5: Same as 11.2 for IC 5063.

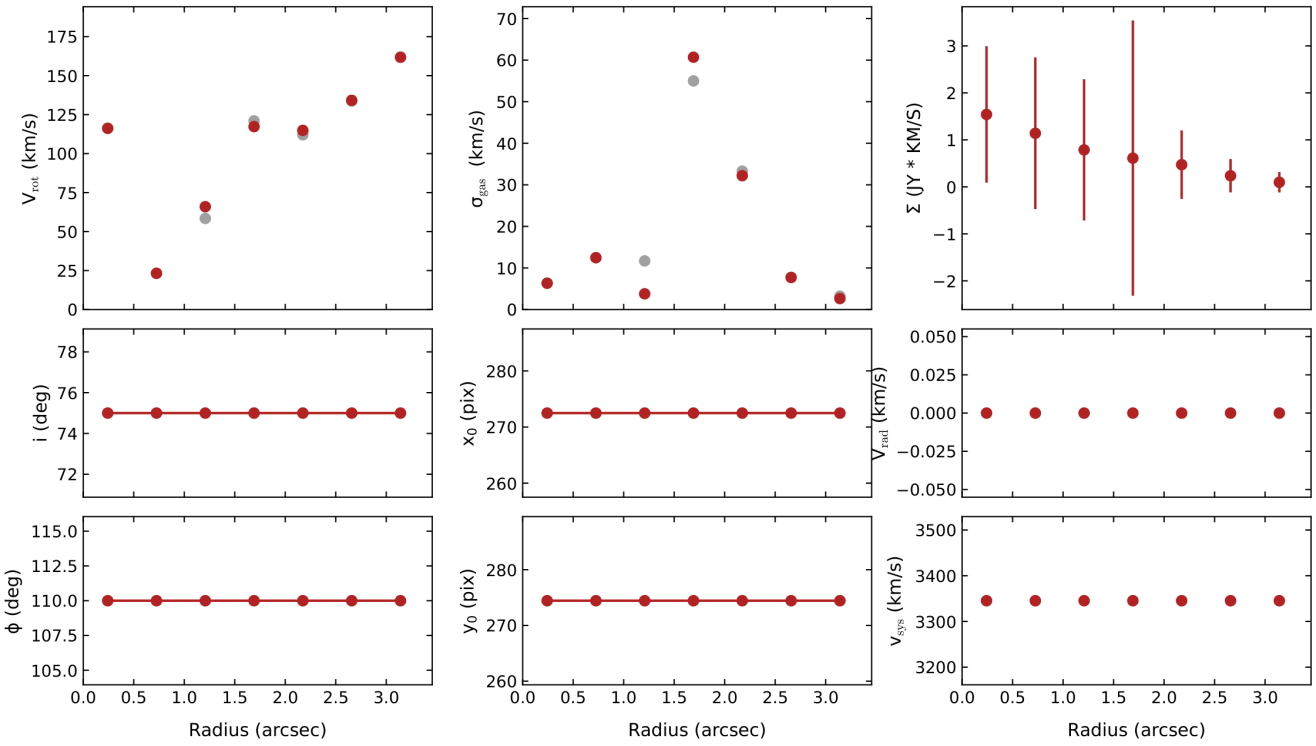


Figure 11.6: Same as 11.3 for IC 5063.

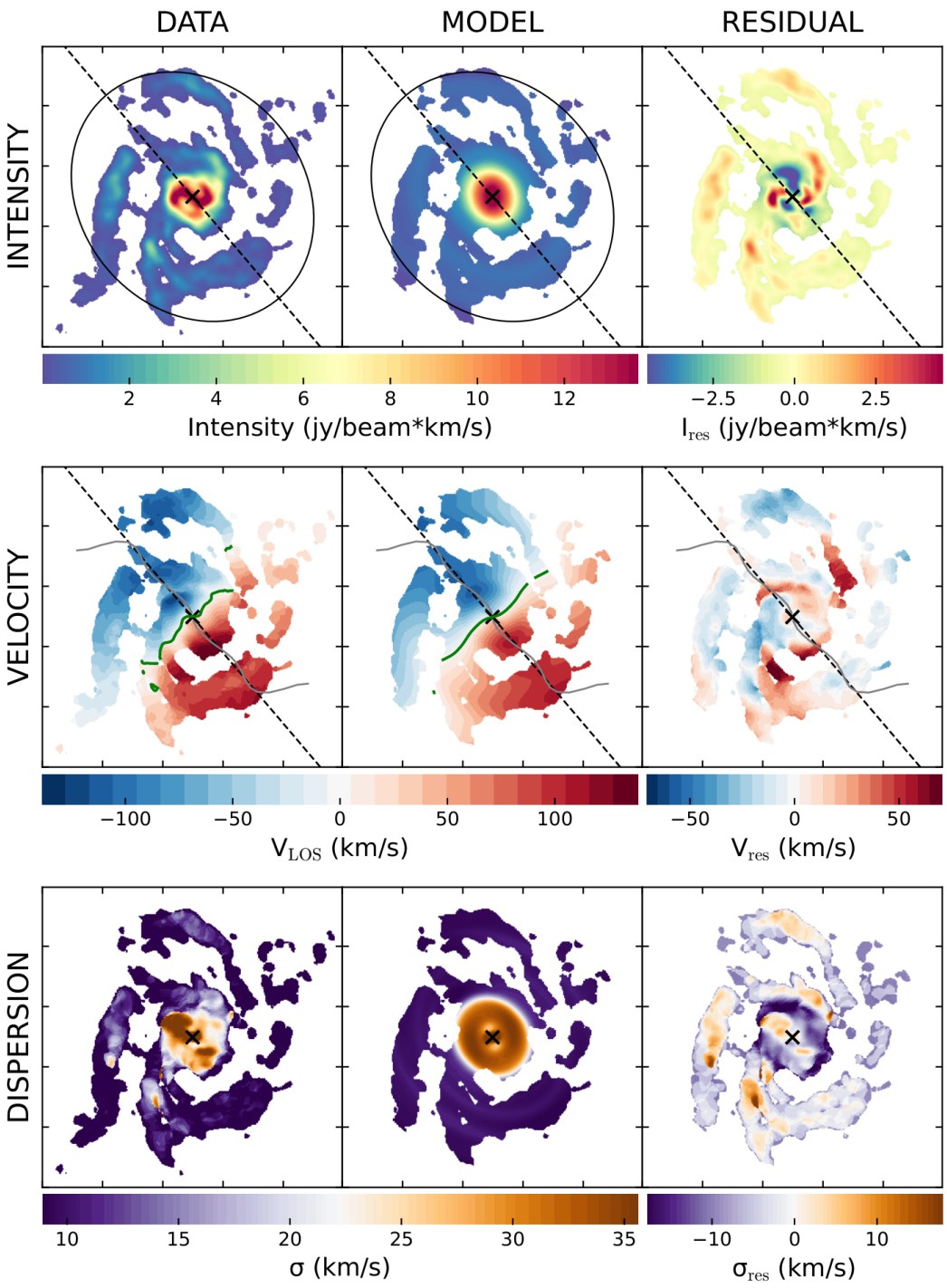


Figure 11.7: Same as 11.1 for NGC 1566.

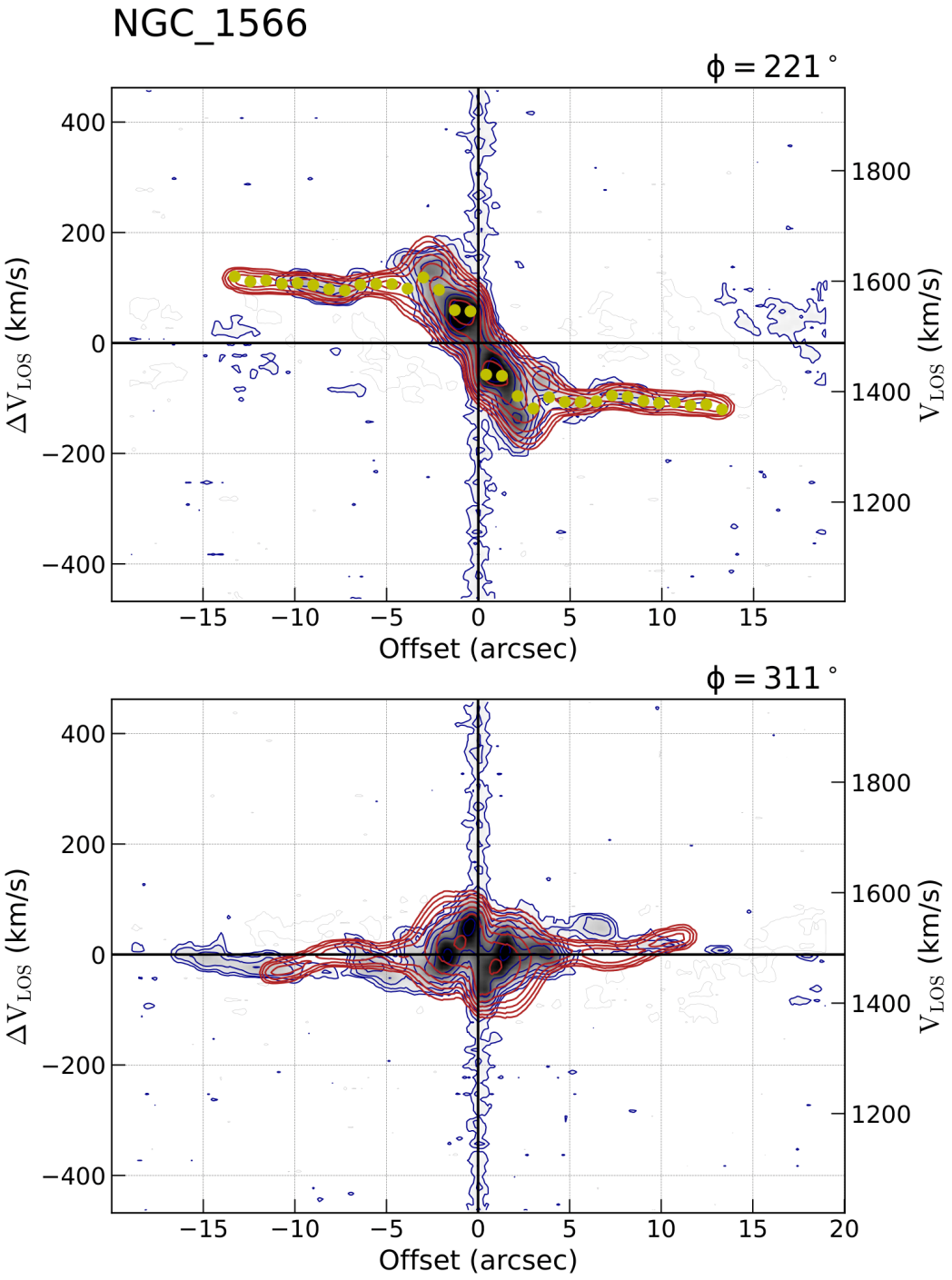


Figure 11.8: Same as 11.2 for NGC 1566.

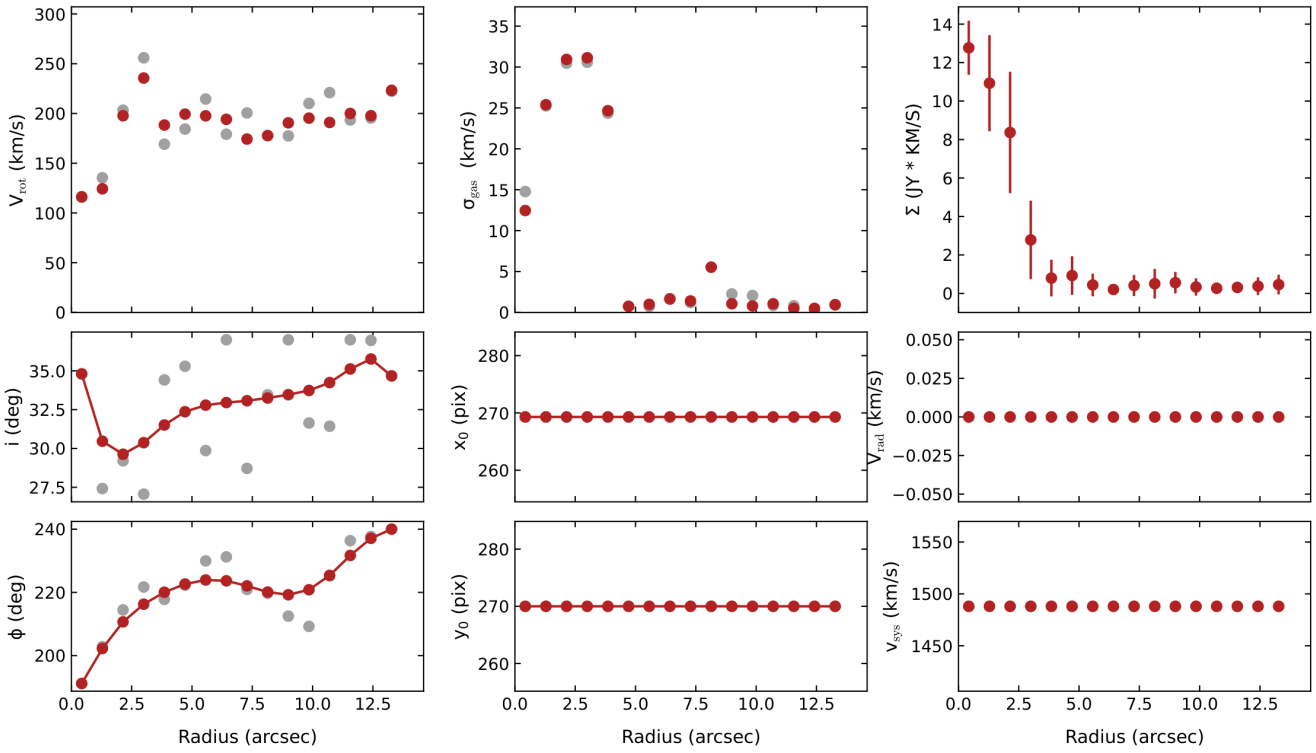


Figure 11.9: Same as 11.3 for NGC 1566.

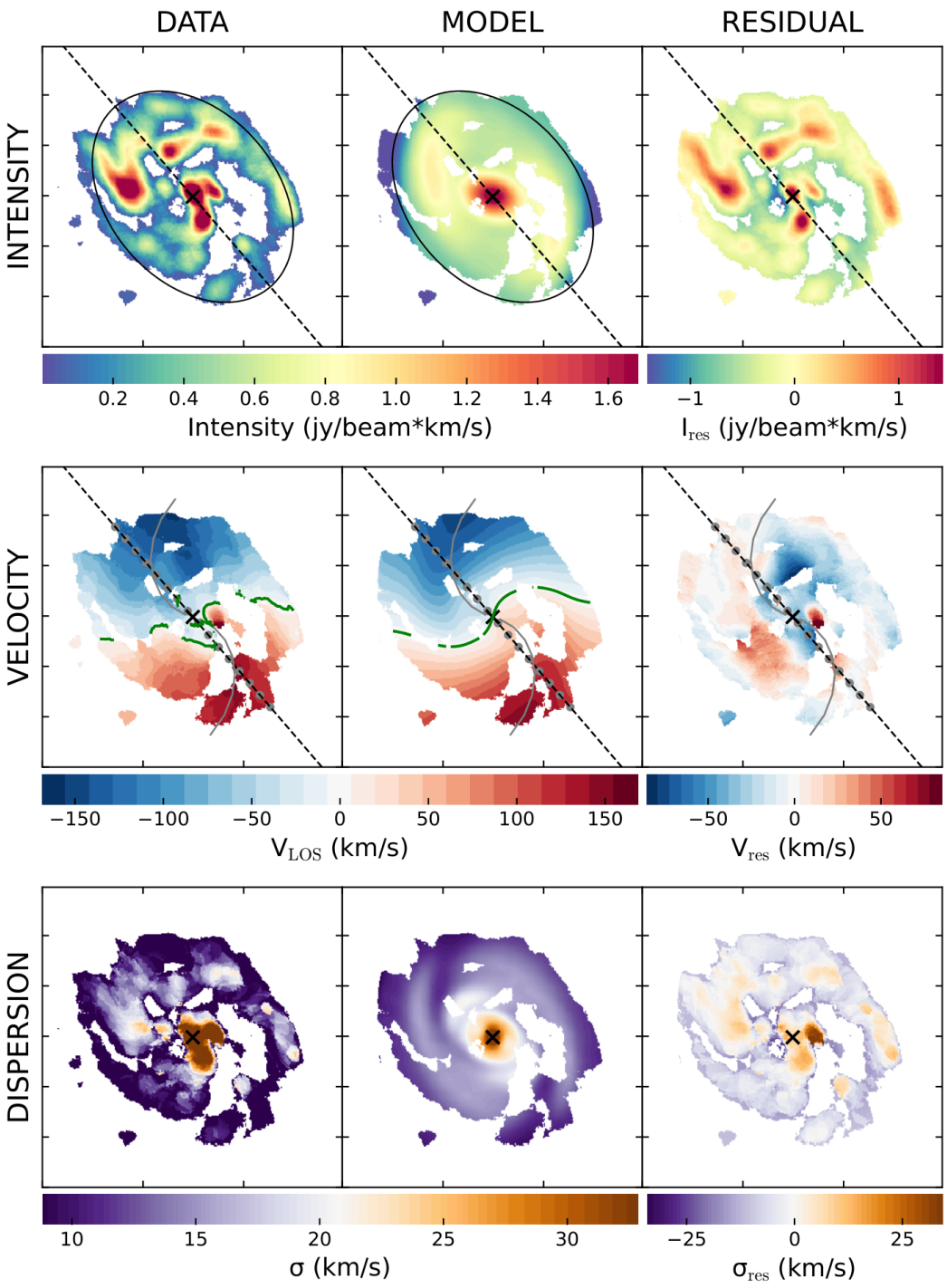


Figure 11.10: Same as 11.1 for NGC 4941.

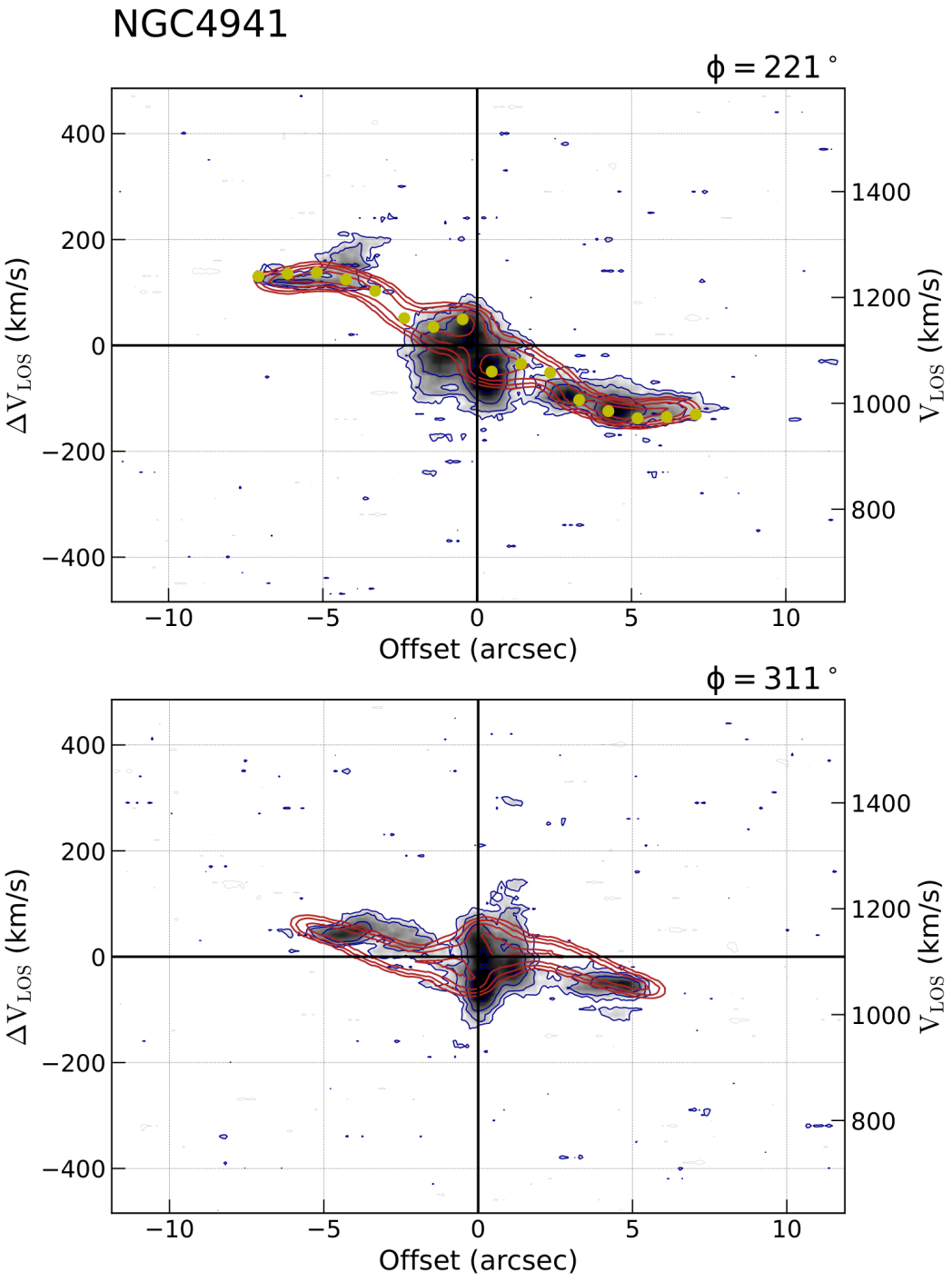


Figure 11.11: Same as 11.2 for NGC 4941.

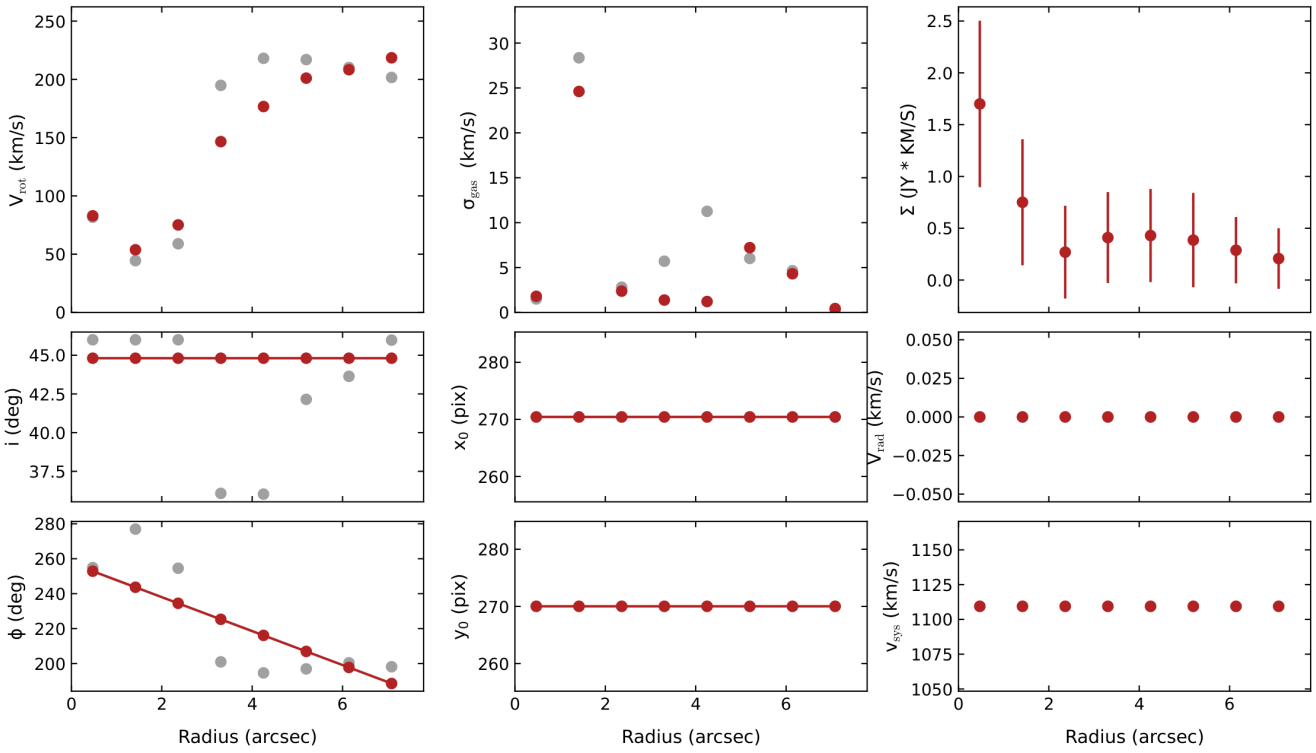


Figure 11.12: Same as 11.3 for NGC 4941.

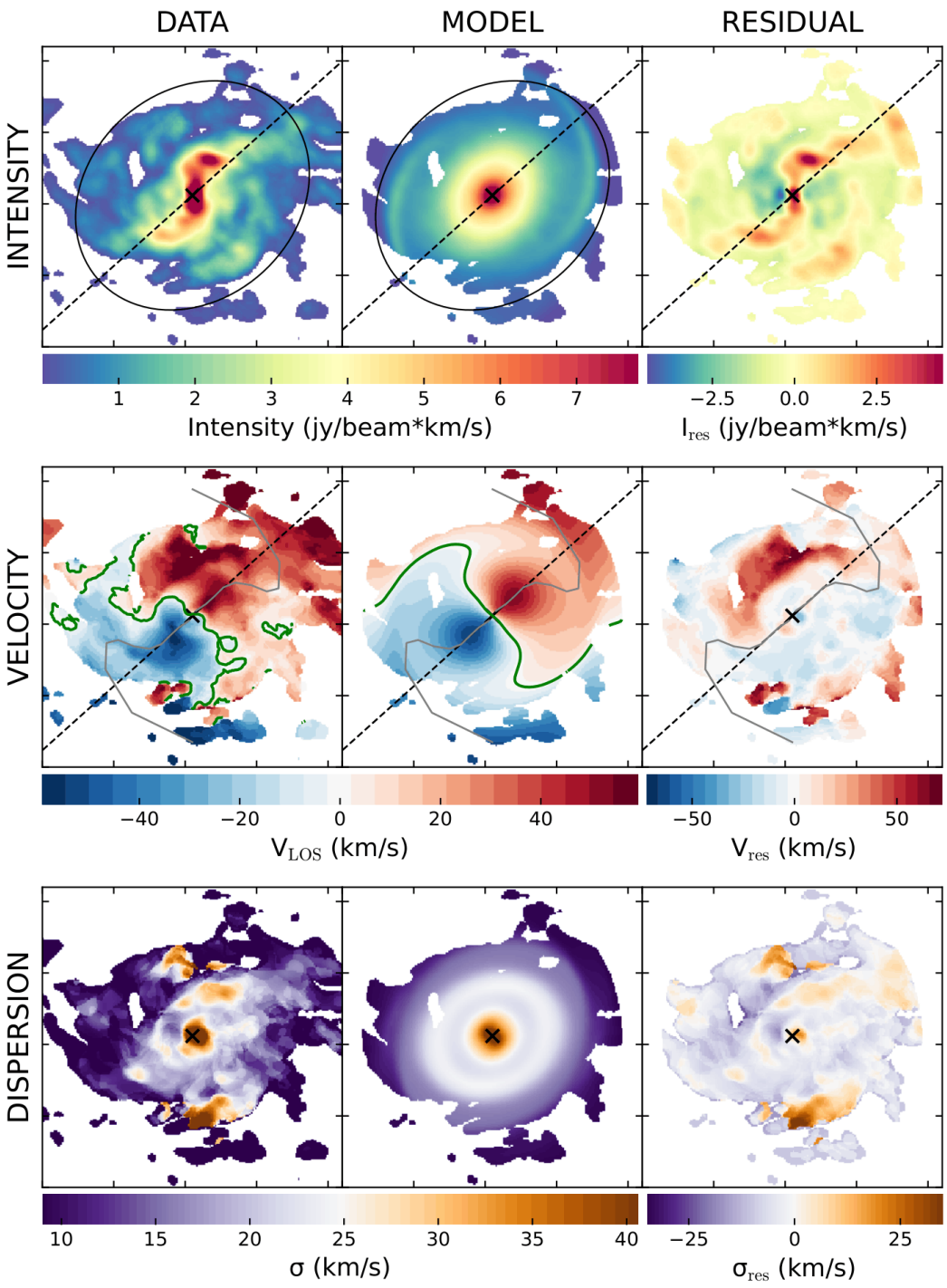


Figure 11.13: Same as 11.1 for NGC 5643.

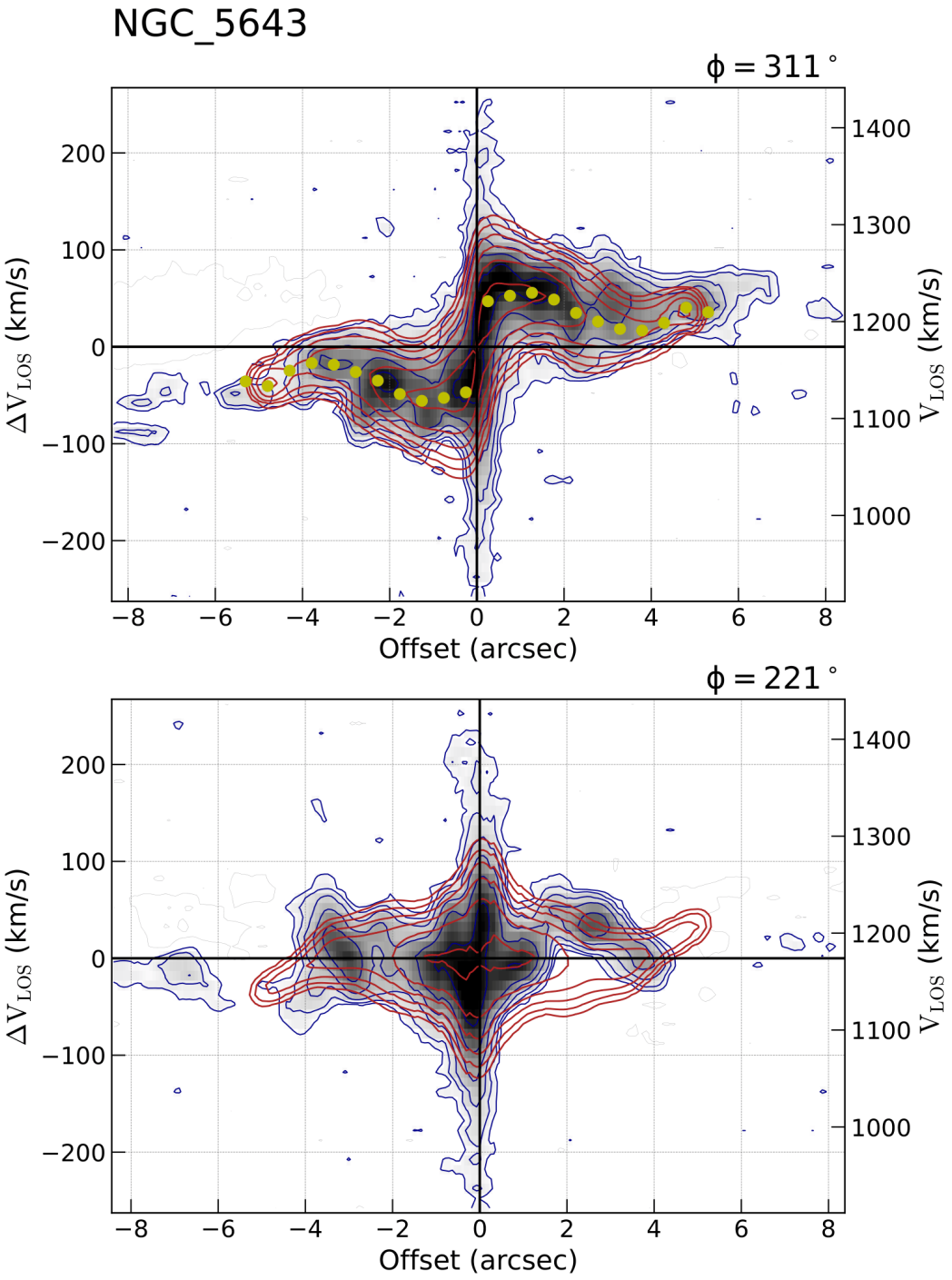


Figure 11.14: Same as 11.2 for NGC 5643.

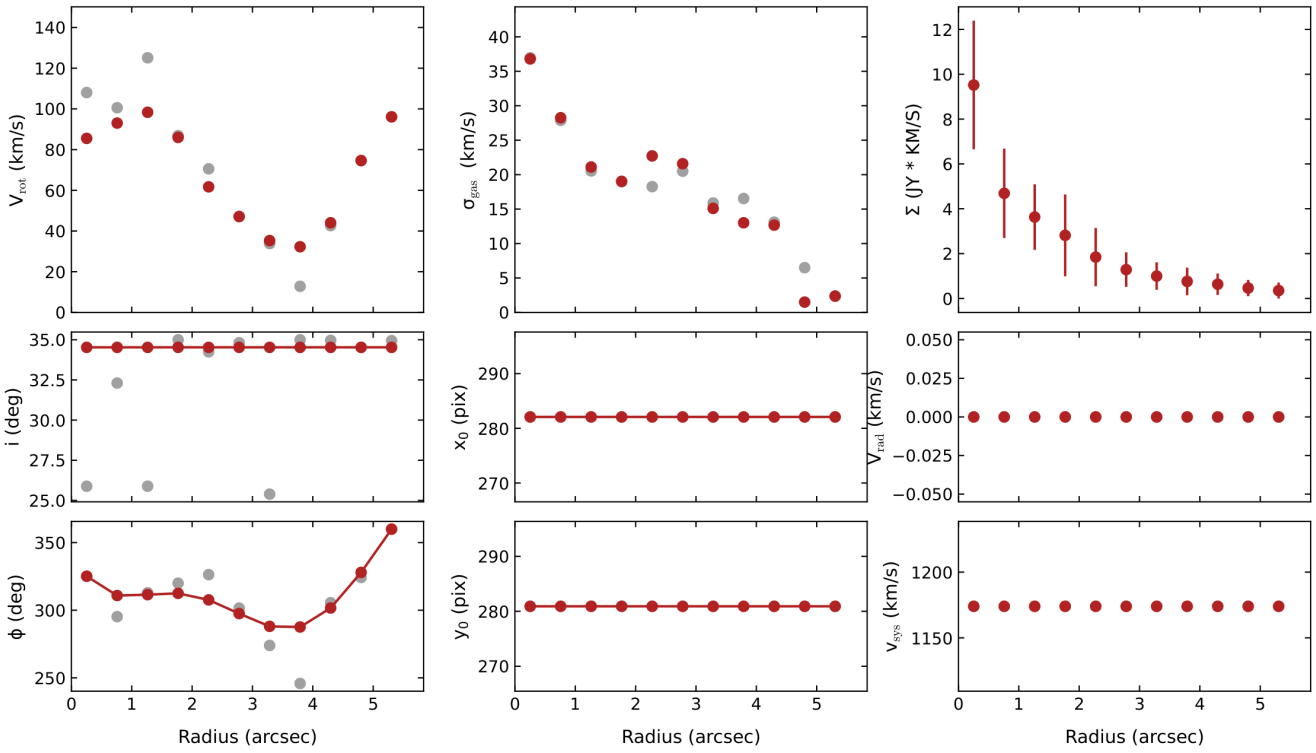


Figure 11.15: Same as 11.3 for NGC 5643.

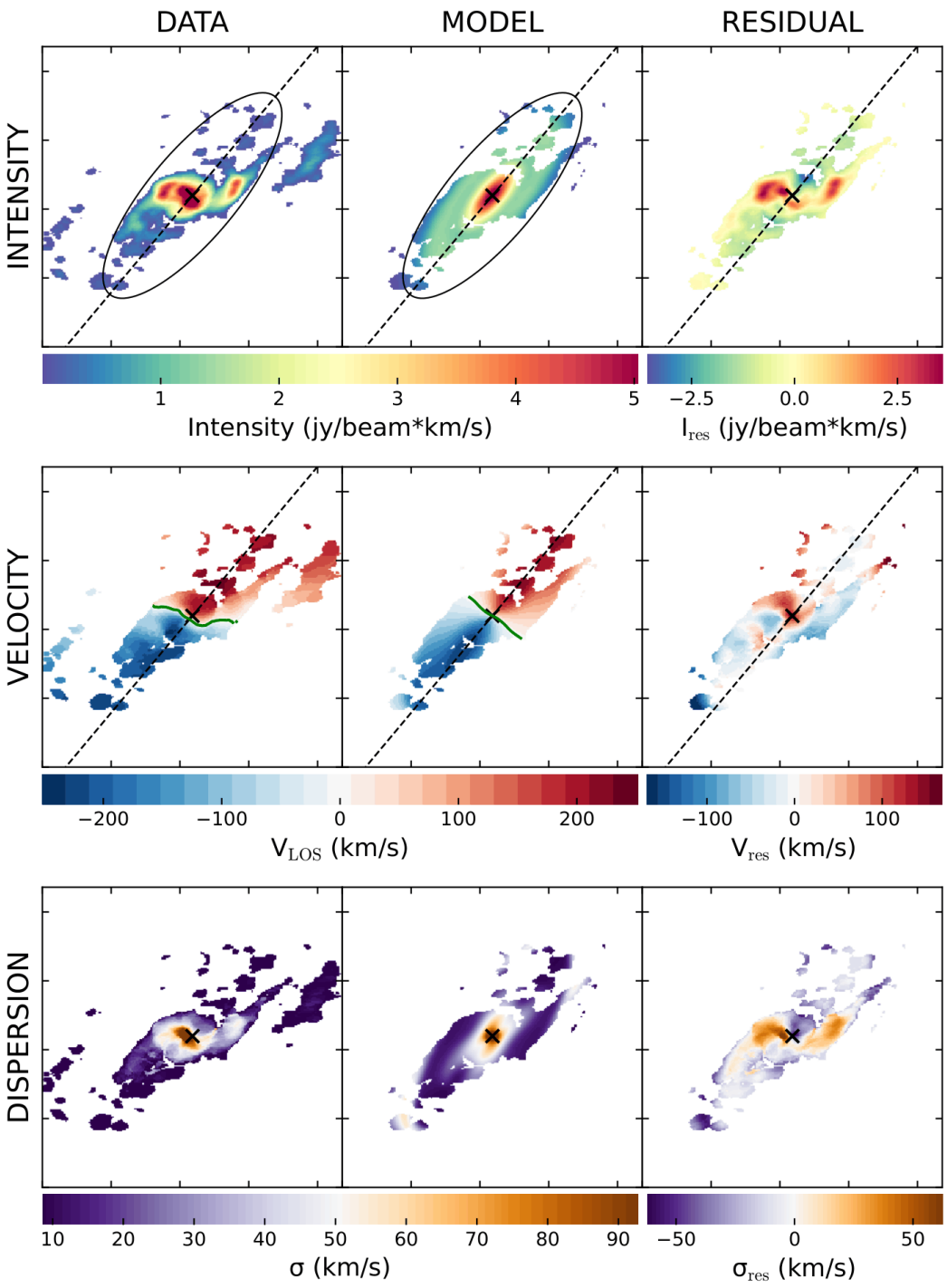


Figure 11.16: Same as 11.1 for NGC 5995.

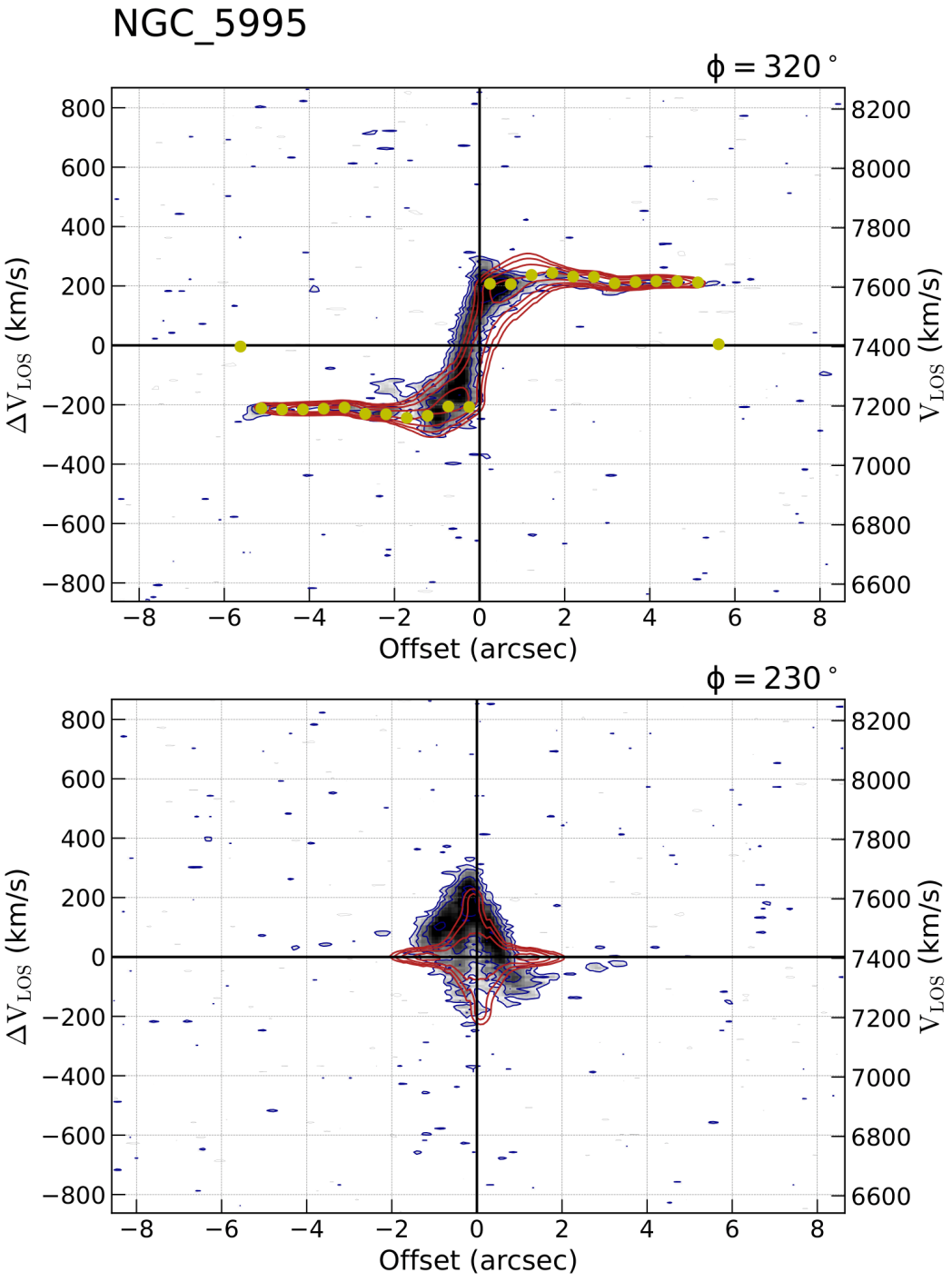


Figure 11.17: Same as 11.2 for NGC 5995.

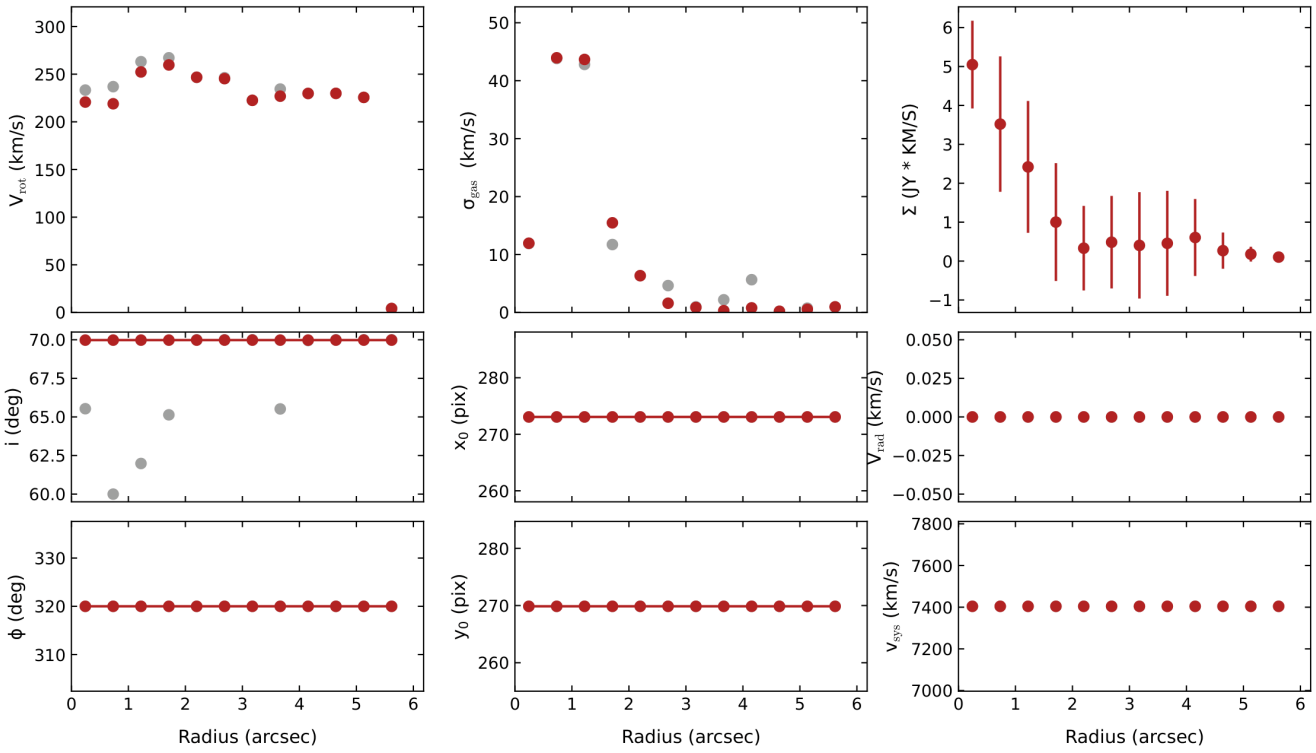


Figure 11.18: Same as 11.3 for NGC 5995.